Design, fabrication and characterization of electromagnetic resonators for medical and environmental applications

Politecnico di Bari

Department of Electrical and Information Engineering
ELECTRICAL AND INFORMATION ENGINEERING
Ph.D. Program
SSD: ING-INF/02–ELECTROMAGNETIC FIELDS

Final Dissertation

Design, Fabrication, and Characterization of Electromagnetic Resonators for Medical and Environmental Applications

---

by

Vincenza Portosi

Supervisor:

Prof. Francesco PRUDENZANO

Coordinator of Ph.D. Program:

Prof. Mario Carpentieri

Course n°35, 01/11/2019-31/10/2022

Department of Electrical and Information Engineering
ELECTRICAL AND INFORMATION ENGINEERING
Ph.D. Program
SSD: ING-INF/02–ELECTROMAGNETIC FIELDS

Final Dissertation

Design, Fabrication, and Characterization of Electromagnetic Resonators for Medical and Environmental Applications

---

by

Vincenza Portosi

Referees:

Prof. Gino SORBELLO

Prof. Luigi BOCCIA

Supervisor:

Prof. Francesco PRUDENZANO

Coordinator of Ph.D. Program:

Prof. Mario Carpentieri

Course n°35, 01/11/2019-31/10/2022

Alla mia famiglia

Tutti possono migliorare e raggiungere il successo a dispetto delle circostanze se si dedicano con passione a ciò che fanno.

Everyone can rise above their circumstances and achieve success if they are dedicated to and passionate about what they do.

Nelson Mandela

Abstract

In this Ph.D. thesis, the feasibility investigation, design, and characterization of different resonant structures optimized to improve the performance of microwave devices for environmental monitoring and medical applications, such as cancer therapy, have been illustrated. In particular:

- A metamaterial lens based on a split ring resonator (SRR) has been designed to improve the focusing of an external applicator for superficial hyperthermia tumour therapy. A prototype has been fabricated by using the standard printed board circuits (PCB) technology and then characterized. The experimental results suggest that a metamaterial based on SRR is a potentially effective option for external microwave applicators in the field of dermatology [1].
- An interstitial microwave applicator has been investigated for deep-seated tumours, a coaxial antenna working in the Industrial, Scientific, and Medical (ISM) frequency band at $f = 2.45\ GHz$. Several simulations have been performed to explore various configurations, impedance matching techniques, and radiating sections. The insertion of a metamaterial lens based on Closed Loop Resonator (CLR) around the radiating section of the applicator has been numerically investigated for a further improvement of the performance. Two prototypes of mini-invasive needle applicators have been constructed and characterized [2-5].
- Metamaterial lenses have been designed to improve the radiation performance of an antipodal Vivaldi antenna for wideband applications. Prototypes have been fabricated and characterized. The experimental results are in good agreement with simulations. The metalens allows the increase of the maximum gain, preserving the antenna bandwidth, and a more symmetrical radiation pattern [6-9].
- A microwave sensor based on a substrate integrated waveguide (SIW) technology has been designed and characterized for the detection of water contamination in the fuel. A suitable radiating slot placed on the top of the SIW

applicator allows the interaction between the microwave electromagnetic field and the fuel contaminated. The sensor is low-cost, low profile and ensures a good sensitivity for constant and real-time monitoring [10].

In addition, during the Ph.D. course, I have contributed to the following side research activities concerning optical electromagnetic field applications:

- The design, fabrication, and characterization of a 2×2 optical fiber coupler based on indium fluoride optical fibers [11]. In particular, I have contributed to the fabrication by means the glass processing system, Vytran® GPX-2400, supplied by the "Electromagnetic Fields" laboratory led by Prof. Francesco Prudenzano, by developing preliminary silica glass samples and by searching the fabrication parameters used for obtaining fluoride glass combiners.
- The design of a gain-switched pulsed laser based on a commercial, heavily holmium-doped fluoroindate glass fiber, emitting in the middle-infrared range, at the wavelength $\lambda = 3.92$ μm [12]. In particular, I have contributed to run several cases and discuss the obtained results.

Acknowledgments

I would like to thank Professor Francesco Prudenzano, my Ph.D. supervisor. Throughout my academic path, Professor Prudenzano has consistently afforded me valuable scientific knowledge, substantial support, and constructive feedback. I am truly grateful for the guidance and encouragement he has given me, as they have played a significant role to my academic growth.

During my research activities, I had the privilege of being a member of an exceptional research group known as the MOE group. I am grateful for the assistance and amicable companionship provided by my colleagues Christian, Antonella, Andrea, Francesco, and Vito. I am especially thankful to Giuseppe and Dario for their consistent aid, and most importantly, for their genuine friendship.

Lastly, I would like to express my heartfelt gratitude to my family. I thank my parents, Pompea e Francesco, for their valuable support. I wish to thank my sister Lucy, who always makes me feel her sweet presence, despite the distance. I would like to express my sincere gratitude to my loved ones Carlo and Paola, who have always encouraged and supported me in challenging times, and rejoiced with me in my small successes, but above all I want to thank them for their trust and love.

I wish to dedicate this thesis to all of them.

Bari, *November* 2023 Vincenza Portosi

Ph.D. Publications

International Journals

[j1] V. Portosi, A.M. Loconsole, F. Prudenzano, "A Split Ring Resonator-Based Metamaterial for Microwave Impedance Matching with Biological Tissue," *Applied Sciences* 2020, vol. 10, n. 19: 6740. doi: 10.3390/app10196740.

[j2] V. Portosi, A.M. Loconsole, M. Valori, V. Marrocco, I. Fassi, F. Bonelli, G. Pascazio, V. Lampignano, A. Fasano, F. Prudenzano, "Low-Cost Mini-Invasive Microwave Needle Applicator for Cancer Thermal Ablation: Feasibility Investigation," *IEEE Sensors Journal* 2021, vol. 21, n. 13, pp. 14027-14034. doi: 10.1109/JSEN.2021.3060499.

[j3] A.M. Loconsole, M.C. Falconi, V. Portosi, F. Prudenzano, "Numerical Design of a Gain-Switched Pulsed Laser at 3.92 μm Wavelength Based on a Ho^{3+}-Doped Fluoroindate Fiber," *IEEE - Optica Journal of Lightwave Technology* 2021, vol. 39, n. 10, pp. 3276-3283. doi: 10.1109/JLT.2021.3064764.

[j4] A.M. Loconsole, V.V. Francione, V. Portosi, O. Losito, M. Catalano, A. Di Nisio, F. Attivissimo, F. Prudenzano, "Substrate-Integrated Waveguide Microwave Sensor for Water-in-Diesel Fuel Applications," *Applied Sciences* 2021, vol. 11, n. 21:10454. doi: 10.3390/app112110454.

[j5] M. Valori, L. Rebaioli, V. Marrocco, F. Modica, F. Bonelli, G. Pascazio, V. Portosi, F. Prudenzano, A. Fasano, V. Lampignano, I. Fassi, "Manufacturing challenges and technological solutions for microwave ablation (MWA) probe prototyping," *Proceedings of the Institution of Mechanical Engineers, Part B: Journal of Engineering Manufacture*. May 2022. doi:10.1177/09544054221101769.

[j6] V. Portosi, A.M. Loconsole, A. Campana, F. Anelli, F. Prudenzano, "A Novel L-Shaped Metalens for Ultra-Wide Band (UWB) Antenna Gain

Improvement," *Applied Sciences* 2023, vol. 13, no. 8. doi: 10.3390/app13084802.

[j7] A.M. Loconsole, V. Portosi, V.V. Francione, F. Anelli, A. Annunziato, M.C. Falconi, F. Prudenzano, "Optimization of a wideband antipodal Vivaldi antenna with metalenses," *International Journal of Microwave and Wireless Technologies* 2023, 1-8. doi:10.1017/S1759078723001022

[j8] F. Anelli, A. Annunziato, A. Maria Loconsole, V. Portosi, S. Cozic, P. L. P. du Teilleul, S. Venck, S. Poulain, F. Prudenzano, "Low-Loss Fluoride Optical Fiber Coupler for Mid-Infrared Applications" submitted to *IEEE - Optica Journal of Lightwave Technology*, August 2023 (Under Review).

Proceedings of International Conferences:

[c1] V. Portosi, A.M. Loconsole, M. Valori, V. Marrocco, F. Bonelli, G. Pascazio, V. Lampignano, A. Fasano, R. Lorusso, F. Prudenzano, "Optimization of low-cost needle microwave applicators for cancer therapy," *IEEE Proceedings XXXIV General Assembly and Scientific Symposium (GASS) of the International Union of Radio Science (URSI)*, Rome, Italy, 28 August – 4 September 2021.

[c2] A.M. Loconsole, G. Roberto, M.C. Falconi, D. Laneve, V. Portosi, A. Massaro, N. Savino, F. Prudenzano, "Compact Vivaldi antipodal SIW antenna for GPR applications," *IEEE Proceedings XXXIV General Assembly and Scientific Symposium (GASS) of the International Union of Radio Science (URSI),* Rome, Italy, 28 August – 4 September 2021.

[c3] A. M. Loconsole, M. C. Falconi, V. Portosi, A. Annunziato, S. Taccheo and F. Prudenzano, "Incoherent Multi-Wavelength Emission in the Wavelength Range 1500-2100 nm," *IEEE Proceedings of AEIT International Annual Conference 2021*, Milan, 04-08 October 2021, pp. 1-6, doi: 10.23919/AEIT53387.2021.9627051.

[c4] V. Portosi, A.M. Loconsole, M. Valori, V. Marrocco, F. Bonelli, G. Pascazio, V. Lampignano, A. Fasano, F. Prudenzano, "Refinement of a Microwave Needle Applicator for Cancer Therapy via Metamaterials," *IEEE Proceedings of 21st Mediterranean Microwave Symposium (MMS*

2022), Italy, Pizzo (VV), 2022. doi: 10.1109/MMS55062.2022.9825526.

[c5] F. Anelli, V. Portosi, A.M. Loconsole, A. Lacatena, A. Quatela, D. Laneve, A. Diaferia, F. Prudenzano, "Design of Electromagnetic Shielding for Food Pasteurization via Corrugated Waveguide and Graphite Rings," *IEEE Proceedings of 21st Mediterranean Microwave Symposium (MMS 2022)*, Italy, Pizzo (VV), 2022. doi: 10.1109/MMS55062.2022.9825598.

[c6] A.M. Loconsole, V. Portosi, V.V. Francione, G. Roberto, F. Anelli and F. Prudenzano, "Wideband antipodal Vivaldi antenna with metalenses for GPR applications," *IEEE Proceedings of 21st Mediterranean Microwave Symposium (MMS 2022)*, Italy, Pizzo (VV), 2022. doi: 10.1109/MMS55062.2022.9825608.

[c7] F. Anelli, A. Annunziato, V. Portosi, S. Cozic, S. Poulain, P. Le Pays Du Teilleul, F. Prudenzano, "Multimode Fluoroindate Optical Fiber Coupler," *Conference on Lasers and Electro-Optics, CLEO Europe 2023*, Munich, 26-30 June 2023.

[c8] A. Annunziato, F. Anelli, A. M. Loconsole, M. C. Falconi, V. Portosi, V. V. Francione, F. Prudenzano, "Optical Combining in Medium Infrared Wavelength Range and its Applications," *IEEE Proceedings of 23rd International Conference on Transparent Optical Networks (ICTON 2023),* Bucarest, 2-6 July 2023.

[c9] F. Anelli, A. Annunziato, A. M. Loconsole, V. Portosi, V. V. Francione, M. C. Falconi, P. Le Pays Du Teilleul, S. Cozic, S. Poulain, Francesco Prudenzano, "Fabrication of Tapered Devices with Fluoride and Chalcogenide Optical Fibers for Mid-IR Applications," *IEEE Proceedings of 23rd International Conference on Transparent Optical Networks (ICTON 2023)*, Bucarest, 2-6 July 2023.

[c10] A. M. Loconsole, A. Annunziato, F. Anelli, V. V. Francione, V. Portosi, M. C. Falconi, F. Prudenzano, "Design of a Pr3+:InF3 fiber laser pumped in near-IR and emitting at 4 micron wavelength," *IEEE Proceedings of 23rd International Conference on Transparent Optical Networks (ICTON 2023)*, Bucarest, 2-6 July 2023.

International Conferences:

[i1] A. Annunziato, F. Anelli, V. V. Francione, V. Portosi, A. M. Loconsole, C. Holmes, M. Godfrey, J. Dulieu-Barton, F. Prudenzano, "Flexible Photonic Sensor for Bending Monitoring," in D-Photon 2023, 3rd International Conference on Dielectric Photonic Devices and System Beyond Visible, Bari, 11-13 July 2023.

[i2] F. Anelli, A. Annunziato, V. Portosi, P. Le Pays Du Teilleul, S. Cozic, S. Poulain, F. Prudenzano, "Indium Fluoride Optical Fiber Coupler for Mid-Infrared Applications," in D-Photon 2023, 3rd International Conference on Dielectric Photonic Devices and System Beyond Visible, Bari, 11-13 July 2023.

[i3] A. M. Loconsole, A. Annunziato, M. C. Falconi, F. Anelli, V. V. Francione, V. Portosi, F. Prudenzano, "Investigation on A Mid-Ir Laser Based on A Praseodymium-Doped Fluoroindate Fiber," in D-Photon 2023, 3rd International Conference on Dielectric Photonic Devices and System Beyond Visible, Bari, 11-13 July 2023.

[i4] F. Anelli, V. Portosi, A. M. Loconsole, V. V. Francione, A. Annunziato, F. Prudenzano, "A Wideband Inkjet-Printed Antenna on Flexible Pet Substrate," in D-Photon 2023, 3rd International Conference on Dielectric Photonic Devices and System Beyond Visible, Bari, 11-13 July 2023.

[i5] A. Annunziato, F. Anelli, V. V. Francione, A. M. Loconsole, V. Portosi, F. Prudenzano, "Mid-IR Optical Combiners for All-In-Fiber Laser," in D-Photon 2023, 3rd International Conference on Dielectric Photonic Devices and System Beyond Visible, Bari, 11-13 July 2023.

[i6] F. P. Pallotta, V. Portosi, A. M. Loconsole, V.V. Francione, F. Anelli, A. Annunziato, A. Crudele, F. Prudenzano, "A Metalens for Non-Invasive Microwave Hyperthermia in Cancer Treatment," in D-Photon 2023, 3rd International Conference on Dielectric Photonic Devices and System Beyond Visible, Bari, 11-13 July 2023.

[i7] A. Annunziato, F. Anelli, V. Portosi, V. V. Francione, A. M. Loconsole, M. C. Falconi and F. Prudenzano, "Optical Fiber Couplers Based on Indium Fluoride Optical Fibers," *Conference on Photonics for Advanced Spectroscopy and Sensing (C-PASS 2023)*, Castellaneta Marina, 3-8 September 2023.

[i8] F. Anelli, A. Annunziato, A. M. Loconsole, M. C. Falconi, V. Portosi, V. V. Francione and F. Prudenzano, “"Fabrication of Mid-IR Tapered Devices Using Fluoride and Chalcogenide Optical Fibers,” *Conference on Photonics for Advanced Spectroscopy and Sensing (C-PASS 2023)*, Castellaneta Marina, 3-8 September 2023.

[i9] A. M. Loconsole, M. C. Falconi, A. Annunziato, F. Anelli, V. Portosi, V. V. Francione and F. Prudenzano, “Investigation on a 4-μm emitting laser based on a fluoroindate fiber doped with praseodymium,” *Conference on Photonics for Advanced Spectroscopy and Sensing (C-PASS 2023)*, Castellaneta Marina, 3-8 September 2023.

Proceedings of National Conferences:

[p1] A.M. Loconsole, M.C. Falconi, D. Laneve, V. Portosi, S. Taccheo, F. Prudenzano, “Wideband optical amplifier based on Tm:Er:Yb:Ho co-doped germanate glass,” *IEEE Proceedings of 2020 Italian Conference on Optics and Photonics (ICOP),* Parma, Italy, 9-11 September 2020. doi: 10.1109/ICOP49690.2020.9300334

[p2] A.M. Loconsole, M.C. Falconi, D. Laneve, V. Portosi, S. Taccheo, F. Prudenzano, “Tm:Er:Yb:Ho amplified spontaneous emission source operating from 1480 nm to 2100 nm,” *IEEE Proceedings of 2020 Italian Conference on Optics and Photonics (ICOP)*, Parma, Italy, 9-11 September 2020. doi: 10.1109/ICOP49690.2020.9300317

[p3] A. M. Loconsole, M. C. Falconi, A. Annunziato, V. Portosi and F. Prudenzano, “Design of a Ho:Nd-codoped fluoroindate fiber for Mid-IR laser emission” *IEEE Proceedings of 2022 Italian Conference on Optics and Photonics (ICOP)*, Trento, June 15-17, 2022.

National Conferences:

[n1] V. Portosi, A. M. Loconsole, F. Prudenzano, “A low-cost microwave needle applicators for cancer ablation,” *Riunione Nazionale di Elettromagnetismo (RiNEm) 2020*, 26-27 September 2020, Rome, Italy

[n2] V. Portosi, A. M. Loconsole, M. Valori, V. Marrocco, I. Fassi, F. Bonelli, G. Pascazio, V. Lampignano, A. Fasano, F. Prudenzano, “Design

of Metamaterials for the Refinement of Mini-invasive Microwave Needle Applicator," *VI Convegno Nazionale "Interazione tra Campi Elettromagnetici e Biosistemi" (ICEmB 2022)*, 8-10 June 2022, Cagliari, Italy

[n3] A. M. Loconsole, V. Portosi, F. Anelli, A. Annunziato, V. V. Francione, M. C. Falconi and F. Prudenzano: "Low-Profile Antipodal Vivaldi Antenna (Ava) for Ground Penentrating Radar Applications," *Riunione Nazionale di Elettromagnetismo (RiNEm) 2022*, 18-21 September 2022, Catania, Italy.

Contents

Introduction

The use of microwave resonator devices in biomedicine and environmental engineering is greatly increased in recent years, creating new opportunities, and opening the way for novel interesting applications. Resonant electromagnetic fields, from microwave to optical frequencies, can be used taking advantage of their immense potential and flexibility. For example, several applications, such as microwave-assisted extraction, in the environmental and chemical field [13,14], microwave-assisted synthesis, in the biotechnology and chemical-pharmaceutics industry [15,16], drying, sterilization and disinfestation, in the agri-food sector [17,18], can benefit greatly from the exploitation of microwave resonators.

Electromagnetic fields resonating at microwave frequencies can be employed in medicine, to realize advanced mini-invasive systems for more efficient hyperthermal cancer treatment and thermo-ablation therapy [19-39]. Hyperthermia therapy for tumours treatment is based on the temperature increasement of the biological tissue regions under treatment, to necrotize the tumor without damages or minimizing the effects for the surrounding healthy tissue. This kind of therapy is strongly emerging as an efficient cancer treatment, in combination with the radio- and chemo- therapy as a feasible alternative to surgical resection [19]. The desired heating can be reached by using radiofrequency waves, microwaves; laser beams or ultrasounds sources [20-22]. The high scattering of the laser in the tissue produces a localized thermal ablation close to the applicator more rapidly than ultrasound or microwaves, but less extended due to the higher attenuation. Ablation by microwaves has been broadly investigated in literature [23-26]. It has attracted great interest because it can produce a rapid and localized temperature increment that causes immediate necrosis of the tumoral cells, and it is able to promote heating through different types of biological tissues. As local treatment, it allows a mini-invasive therapy, improving the patient wellness during and after the ablation session. During the last years, devices for hyperthermia therapy of mammary, hepatic, renal, and pancreatic carcinomas have been studied and developed [27-30].

Microwave applicators basically consist of a microwave generator and an antenna and can be divided into external and internal applicators depending on their peculiar use. They can be designed employing different kinds of radiating sections. For example, monopole, dipole, slot, and helical antennas, that irradiate directly into the target tissues via intracavitary, percutaneous, or laparoscopic paths, have been designed for internal applicators [30-39]. Among the various types of antennas studied for the external applicators there are waveguide and horn antennas [40], phased array antennas [41] and patch antennas [42-44]. Different shapes, rectangular, circular, horseshoe, have been considered for the radiating slot of microstrip antennas for microwave hyperthermia treatment of cancer [45]. The design of the patch antenna and the choice of the operating frequency must take into account the size and depth of the tumoral mass. At low frequencies large penetration depth of the electromagnetic field can be obtained, but also the radiating system employed in order to produce an adequate localized heating become larger. Microstrip applicators at 915 MHz, 433 MHz, and 190 MHz, have been designed with low loss, high dielectric constant, substrate to treat tumours at 2 cm, 3 cm, and 4 cm depth [23].

Among the principal drawbacks of patch antennas there are the narrow bandwidth and low penetration depth capability. A water bolus is usually placed between the external applicator and the body in order to improve the matching of the antenna and at same time maintain the temperature of the skin at normal human body level. Microwave resonators have been investigated in literature to improve external applicators for superficial cancer treatment, in particular metamaterial lens can improve the antenna directivity and reduce the beam width and side lobe ratio [46-49]. Left-handed metamaterial lenses have been numerically investigated in order to improve the focusing in superficial tumour [50,51]. Metamaterial zeroth-order mode applicators have been proposed in order to produce a more homogeneous specific absorption ratio (SAR) distribution, similar to that of an ideal plane wave, and larger penetration capability [52,53].

Microwave resonators can also be exploited in order to improve Ultra-Wide Band antennas radiation performance [54-65]. These antennas find application in different fields, such as ground-penetrating radar (GPR) [66], fifth generation (5G) and communication systems [67-73], microwave imaging [74,75], and medical applications [75]. Lenses based on metamaterial technology are designed, optimized, and fabricated for the enhancement of Antipodal antennas. Non-resonant metamaterials, based on conventional parallel-line unit cells, are used to enhance the gain [57-59] and to stabilize the radiation pattern [59]. In [60], a zero-index metamaterial (ZIM) by using meander line cells is proposed

for obtaining a gain increase of about 4 dB of an antipodal Vivaldi antenna (AVA). A modified H shape cell is used for a ZIM lens to obtain a gain enhancement of up to 2.6 dB of an AVA slot antenna in frequency bands close to 60 GHz [61]. Epsilon-near-zero (ENZ) metamaterials can be exploited to increase the gain of conventional [62] and double-slot AVAs [63]. Gradient refractive index (GRI) metasurface lenses, based on non-resonant unit cells, allow the improvement in the radiation properties if placed in front of the antenna at an optimized distance [64,65].

Microwave planar sensors for real-time and non-invasive sensing systems are another example of intriguing use of microwave resonant devices. A number of industrial, environmental, and medical applications have seen a renewed interest due to recent developments in the field of microwave planar sensors. For example, monitoring of hydrocarbon quality is an important goal, not only for modern automotive, industrial, and aerospace applications, but also in view of the next uses of biodiesel fuel generation [76,77]. There are many different contaminants that can compromise hydrocarbon quality, such as alcohol, water, ethanol, and oils [78-80]. Monitoring should be fast, accurate and real time, because these contaminants could alter the lubrification properties of fuel and reduce motor performance. In particular, they could alter the viscosity, density, and boiling point of the hydrocarbons [81]. In general, traditional laboratory techniques, such as an evaporation test, distillation, gas chromatography, etc., useful to identify the quality of petroleum liquid and its derivative products, are more expensive and introduce a delay time for analysis. Microwave sensor techniques provide an interesting alternative approach [80-86]. Water contamination can be detected by using different electromagnetic technologies, including optical fiber gratings and microwave reflection techniques [87-93]. Microwave sensors can be very efficient devices for real-time water detection, since the dielectric constant of water, $\varepsilon_{r,H_2O} = 70$, is about 40 times the dielectric constant of diesel fuel, $\varepsilon_{r,fuel} = 1.75$, at the frequency $f = 10\ GHz$. Many different kinds of devices have been proposed, including coaxial antennas and microstrip sensors, stacked multi ring resonators (SMRR) or vertically stacked ring resonators (VSRR), and microwave resonant cavities [80-88,93-97]. Microstrip technology, in addition to having a number of practical advantages, allows to design compact and integrated devices, but it does not guarantee a complete confinement of the electromagnetic field and suffers radiating losses. On the other hand, Substrate-Integrated Waveguide (SIW) technology allows to obtain compact and low-cost solutions, good performances, integration of active and passive devices

on a single substrate, good electromagnetic field guidance, a reduction in insertion and radiation losses, and the use of higher power [98-111].

This thesis has been focused on the theoretical study, design, and optimization of novel devices and systems that can be used in biomedical and environmental applications. In particular:

THE FIRST CHAPTER recalls the theory for the design of metamaterials and Substrate-Integrated Waveguide devices.

THE SECOND CHAPTER illustrates the design of a metamaterial lens based on the split ring resonator (SRR) to improve the impedance matching of a SIW cavity backed patch antenna loaded with biological material, thus obtaining an applicator for skin cancer therapy.

THE THIRD CHAPTER reports the design of a needle microwave applicator for hyperthermia liver cancer treatment. Impedance matching techniques, cooling system effects, innovative 3D additive printing techniques, and the insertion of a metamaterial lens based on Closed Loop Resonator (CLR) are investigated to improve the applicator performances.

THE FOURTH CHAPTER describes the design, fabrication, and characterization of a novel metamaterial lens for the gain improvement of an Ultra-Wide Band antenna, that can be employed for environmental applications.

THE FIFTH CHAPTER illustrates the design, fabrication, and characterization of a microwave SIW sensor for detection of water in diesel.

2 Theory

In this chapter, a recall of theory useful for the design of the devices, proposed in this thesis, is briefly reported.

2.1 Metamaterials

Metamaterials (MTMs) are artificial materials designed with the aim of obtaining special electromagnetic (EM) properties that would not normally be available in nature. They are typically constituted by periodic repetitions of elementary units with sizes significantly less than the wavelength of the propagating EM field. Therefore, the MTMs are inhomogeneous structures that can be globally considered as a homogeneous medium. Their EM properties can be described by the effective parameters ε_{eff} and μ_{eff}, that could be calculate considering the average of the local charge, current, and field distribution. Due to the possibility of manipulating EM characteristics, the metamaterials are considered particularly interesting and very promising for applications in several fields, from microwaves to optical frequencies [112].

Many types of MTMs have been designed, and now, different criterions are necessary for a comprehensive classification. A standard way to categorize them is based on the sign of effective permittivity ε_{eff} and effective permeability μ_{eff}.

Figure 2.1 illustrates the diagram of MTMs classification as function of effective permittivity ε_{eff}, effective permeability μ_{eff} and effective refractive index n_{eff}. Metamaterials based on Split Ring Resonator (SRR) have been considered for the design of microwave resonators in this thesis.

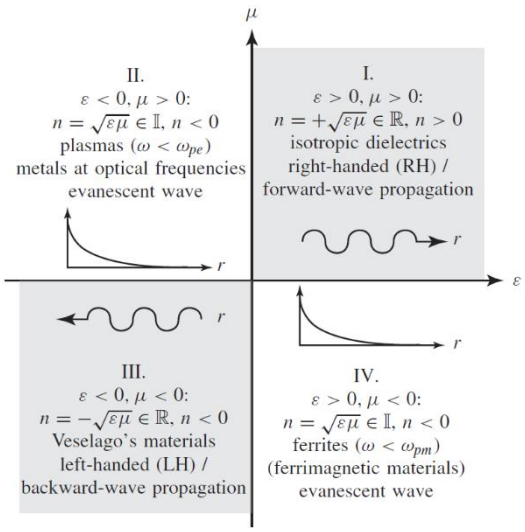

Figure 2.1 Diagram of MTMs classification as function of effective permittivity ε_{eff}, effective permeability μ_{eff} [112].

2.1.1 Theoretical model of the Split Ring Resonators

In [113], for the first time, SRR was proposed in order to realize Mu-negative (MNG) materials (fourth quadrant in Figure 2.1). Figure 2.2 shows the double rings structure proposed in [113].

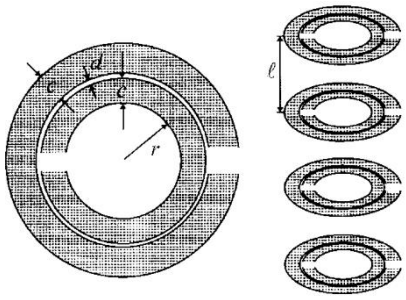

Figure 2.2 Scheme of the double ring configuration of the SRR proposed in [113].

When an electromagnetic wave propagates orthogonally to the SRR plane, the SRR behaviour can be approximatively described by an equivalent LC circuit, where the inductance and the capacitance are related to the currents induced in the metal rings and to the capacitive phenomena between the split terminations (capacitive gap), respectively [112]. If the dimension of unit cell is very small with respect to wavelength λ, the metamaterial layer exhibits an effective capacitance and an effective inductance at macroscopic/average level, according to the effective medium theory, which lead to the calculation of an effective

permeability [113]. Figure 2.3 illustrates the equivalent circuit model of (a) double SRR and (b) single SRR configuration.

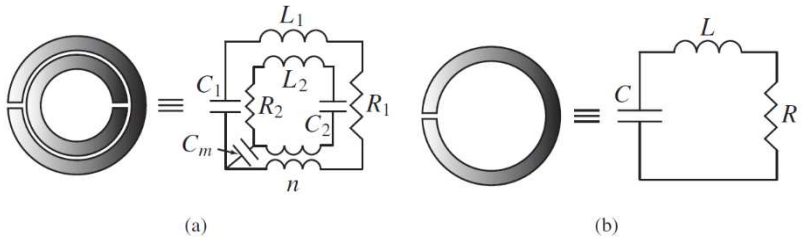

Figure 2.3 Equivalent circuit model of (a) double SRR and (b) single SRR configuration [112].

The analytical model and physics of the split ring resonators is recalled since it has been employed in order to roughly obtain preliminary geometric parameters of the microwave resonators designed in this thesis.

The metamaterial based on SRR exhibits an effective magnetic permeability described by the Lorentz model approximation [112,113]:

$$\mu_{r_{eff}}(\omega) = 1 - \frac{F\omega^2}{\omega^2 - {\omega_{0m}}^2 + j\gamma\omega} \tag{2.1}$$

where ω_{pm} and ω_{0m} are the plasma magnetic and resonant frequency, respectively, F is the fractional of the unit cell occupied by interior ring, and γ is the damping factor due to metal losses. Starting from (2.1) a frequency range in which $Re\left(\mu_{r_{eff}}\right)$ is negative can be identified:

$$\omega_{0m} < \omega < \frac{\omega_{0m}}{\sqrt{1-F}} = \omega_{pm} \tag{2.2}$$

where the plasma magnetic frequency ω_{pm} and the resonant frequency ω_{0m} are finely tunable by optimizing the geometry of the unit cell, see Figure 2.4.

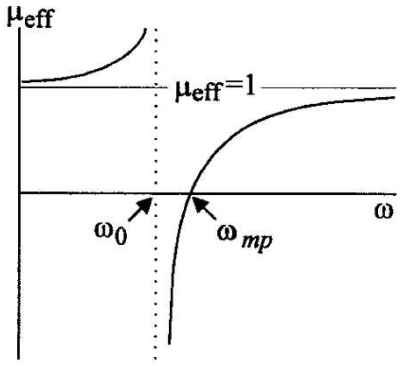

Figure 2.4 Generic curve of the effective permeability $\mu_{r_{eff}}$ of the SRR [113].

Considering an array of single broadside coupled SRRs, with rings in the xy-plane, the effective magnetic permeability is described by (2.3) [46]:

$$\mu_{r_{eff}} = 1 - \frac{j\,\omega\,L_{eff}\,S}{\Delta_x \Delta_y (R_{eff} - \frac{j}{\omega\,C_{eff}} + j\,\omega\,L_{eff})} \tag{2.3}$$

$$S = l_x l_y \tag{2.4}$$

where Δ_x and Δ_y are the dimensions of the SRR unit cell in xy-plane, l_x and l_y are the lengths of the metallic ring in the x- and y-directions, respectively, and R_{eff}, C_{eff} and L_{eff} are the effective resistance, effective capacitance and effective inductance of the metamaterial, respectively. The effective capacitance is approximatively obtained from the formula for the capacitance per unit length of a strip line [114].

$$C_{eff} = \frac{\varepsilon_r\,\varepsilon_0\,l}{4}\,\frac{K(k)}{K'(k)} \tag{2.5}$$

$$k = tanh\frac{\pi\,w}{2\,t} \tag{2.6}$$

$$l\ =\ 2(l_x + l_y - s) \tag{2.7}$$

where $K(k)$ and $K'(k)$ are elliptic integrals [115], w, s are the width and the split gap of the SRR, t is the distance between the two SRR in the z-direction. The effective inductance is [114]:

$$L_{eff} = \frac{\mu_0\,S}{t} \tag{2.8}$$

The effective resistance R_{eff} includes the radiation resistance and the loss resistance [114].

In other words, the control of the effective magnetic permeability, by varying both the inductive and capacitive properties of metamaterial, via a proper SRR optimization, is the basis physics principle of the electromagnetic field focusing.

a) Metalens for improving antenna gain

A planar metamaterial lens based on SRR, formed by an array of the unit cell in the rings plane, exhibits an anisotropic negative permeability; if the wave propagates in the z-direction, the permeability tensor is [46]:

$$\mu = \mu_0 \begin{pmatrix} 1 & 0 & 0 \\ 0 & 1 & 0 \\ 0 & 0 & \mu_{r_{eff}} \end{pmatrix} \tag{2.9}$$

When the antenna radiation frequency is within the range for which the permeability element $\mu_{r_{eff}}(\omega) < 0$ the x-axis wave vector component is imaginary $k_x = \omega\sqrt{(\varepsilon_y \mu_z)}$, therefore the component of the electromagnetic field parallel to SRRs plane is evanescent and the sideward radiation forbidden, see Figure 2.5. Consequently, the main lobe of antenna radiation pattern will be improved while the side lobe attenuated and there is an overall improvement in terms of directivity and gain [47].

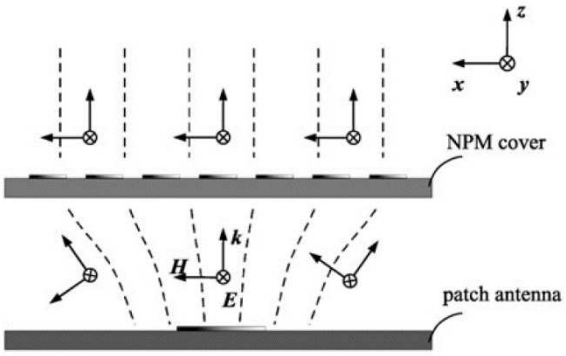

Figure 2.5 Radiation scheme of a patch antenna with a MTM superstrate based on SRR [47].

a) Metalens as impedance matching layer for medical applications

The metamaterial lens placed on the antenna, in addition to the electromagnetic field focusing properties, allowing the gain increasement, can be used as impedance matching layer. When the radiated electromagnetic waves propagate through media with different permittivity and permeability values an impedance mismatch occurs. The scheme of the normal wave propagation through the two layers sandwiched between two semi-infinite media is illustrated in Figure 2.6, where the SRR metamaterial layer is placed at distance t_2 from the biological layer to be matched.

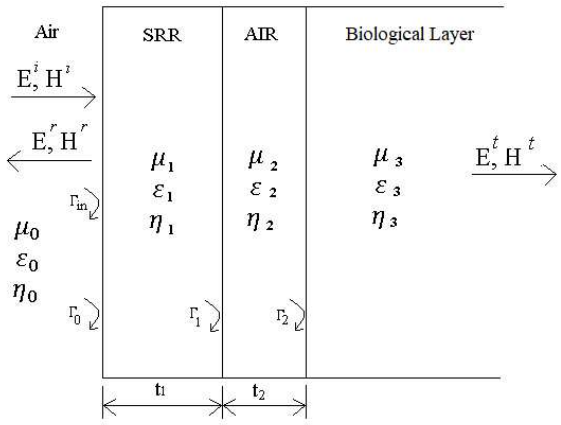

Figure 2.6 Scheme of the normal wave propagation through the two layers sandwiched between two semi-infinite media. The SRR metamaterial layer is placed to distance t_2 from the medium to be matched [1].

The metamaterial lens, if properly designed, can minimize the mismatch, and maximize the energy transmission. With reference to the Figure 2.6 the general form of wave matrices is given by (2.10).

$$\begin{bmatrix} E^i \\ E^r \end{bmatrix} = \prod_{n=1}^{3} \frac{1}{T_n} \begin{pmatrix} e^{i\gamma_n t_n} & \Gamma_{n-1} e^{-i\gamma_n t_n} \\ \Gamma_{n-1} e^{i\gamma_n t_n} & e^{-i\gamma_n t_n} \end{pmatrix} \begin{bmatrix} E^t \\ 0 \end{bmatrix} = \begin{pmatrix} a_{11} & a_{12} \\ a_{21} & a_{22} \end{pmatrix} \begin{bmatrix} E^t \\ 0 \end{bmatrix} \tag{2.10}$$

$$\Gamma_{in} = \frac{E^r}{E^i} = \frac{a_{21}}{a_{11}} \tag{2.11}$$

where T_n, γ_n and t_n are the transmission coefficient, propagation constant and thickness of the layer n, and Γ_{n-1} is the reflection coefficient at the $(n-1)$-n layers interface. The total reflection coefficient of the multiple layers Γ_{in}, given by (2.11), is zero for a 'perfect' impedance matching. By considering (2.11), the total reflection coefficient is a function of frequency and can be minimized by appropriately planning the effective magnetic permeability of the metamaterial and by adjusting the distance from the medium to be matched.

Moreover, the impedance of the metamaterials is given by [112]

$$Z(\omega) = \sqrt{\frac{\mu_{eff}(\omega)}{\varepsilon_{eff}(\omega)}} \tag{2.12}$$

where ω is the angular frequency of the propagating EM wave, $\varepsilon_{eff}(\omega)$ is the effective electrical permittivity, and $\mu_{eff}(\omega)$ is the effective magnetic permeability, whose real and imaginary parts are handled by varying: i) the geometry and dimensions of the unit cells pattern, and ii) the thickness and permittivity of

the dielectric substrate. The resonant frequency of the metamaterials is given by [112]

$$f = \frac{1}{2\pi\sqrt{L_{eff} \times C_{eff}}} \tag{2.13}$$

where the effective inductance L_{eff} and the effective capacitance C_{eff} are related to the conductive elements and to the spacing between them. The length and the width of the metal strips define the effective inductance value. The gap between two adjacent loops, the loop length and the dielectric permittivity of the substrate define the effective capacitance value. Considering (2.12) and (2.13), the impedance matching of the needle applicator with the biological medium is possible by using a suitably designed metamaterial lens. In this thesis, modelling, operating frequency tuning in the operating frequency band, and impedance matching optimization of the MTM lens have been performed by numerical simulations with the commercial EM software CST Microwave Studio®.

2.1.2 Effective Parameters Extraction

Considering the state of the art, there are several approaches for modelling metamaterials [116-118]. A way for metasurfaces modelling, by considering their effective electrical and magnetic surface susceptibilities, is reported in [116]. Anyway, the most largely employed is based on the evaluation of the volumetric effective electric permittivity and volumetric magnetic permeability [54-67,69,75]. This method, based on the assumption of homogenization, exploit the S-Parameter Retrieval (SPR) method, based on the Kramers-Kronig relationship, and requires the definition of an effective thickness d_{eff} related to volumetric effective parameters of the effective homogeneous layer modelling the metamaterial. The effective electric permittivity ε_{eff} and the effective magnetic permeability μ_{eff} are calculated from the complex wave impedance Z_{eff} and complex refractive index N_{eff}, obtained from the S-parameters [116-118].

The effective volumetric material properties can still be used for metasurfaces modelling if the effective thickness d_{eff} along propagation direction is held constant. The effective material properties retrieved with a set thickness can be used without any loss of generality [116]. On the other hand, if one changes the thickness, but keeps the effective properties the same, then the results would be meaningless [116].

It should also be noted that, using the SPR method, the imaginary part of the retrieved effective parameters could be negative in narrow frequency bands.

Anyway, the magnetic and electric dipoles induced in metamaterials are not independent of each other, and the passivity condition can be fulfilled even when $Imm(\varepsilon_{eff}) < 0$ or $Imm(\mu_{eff}) < 0$ [117,119].

In this thesis, the SPR method is exploited for the preliminary design of the metalens, whereas the optimization of the actual microwave devices has been performed with full-wave numerical simulations.

2.2 Substrate-Integrated Waveguide

The Substrate Integrated Waveguide (SIW) is a planar waveguide-like structure, that can be realize by inserting of two parallel rows of metal posts (vias) into a dielectric substrate. The posts are electrically connected with two parallel metal plates, see Figure 2.7. The EM propagation in this structure is similar to that in the standard rectangular waveguide. The SIW has the same advantages as standard rectangular waveguide, such as high quality-factor and high power-handling capability, and in addition the same advantages as planar technology, such as low cost and easy fabrication and high integration with planar circuits [101].

In this thesis, the SIW technology has been considered for the design of a planar microwave sensor for environmental applications.

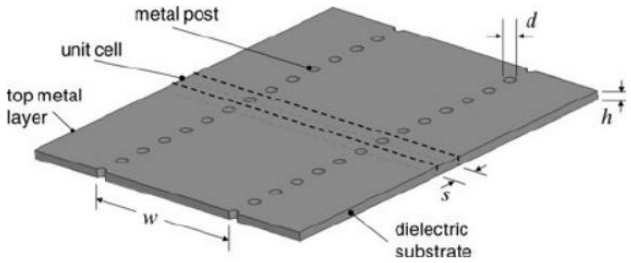

Figure 2.7 Scheme of a generic SIW [101]

2.2.1 SIW design basics

For the design of the SIW, the three fundamental geometrical parameters are the width of the SIW w, i.e. the distance between the two parallel rows of vias, the vias diameter d and the distance between the centres of adjacent vias in the same row s, see Figure 2.7. Different empiric methods have been proposed in literature, that allow to calculate these parameters, starting from the operating frequency and the effective width w_{eff} of the standard rectangular waveguide with the same propagation characteristics [98-99,120].

In this thesis, the empirical equation (2.14) has been used for the preliminary design.

$$w_{eff} = w - \frac{d^2}{0.95\ s} \tag{2.14}$$

The precision of (2.14) is within $er = \pm 5\%$, and the approximation is valid if the following conditions are respected [98]:

$$s < \frac{\lambda_0 \sqrt{\varepsilon_r}}{2} \tag{2.15}$$

$$s < 4\ d \tag{2.16}$$

where λ_0 is the wavelength in air and ε_r is the dielectric constant of the substrate.

The optimization of the SIW structures has been performed by using full-wave simulations.

2 Design of a microwave resonator applicator for superficial hyperthermia cancer treatment

2.1 Introduction

The high absorption of microwave energy by tumour tissues, due to the intrinsic biological characteristics, makes microwave hyperthermia an efficient cancer therapy technique. Hyperthermia applicators can be classified into non-invasive external, and invasive or mini-invasive internal applicators, depending on the location of the tumour to be treated. Non-invasive microwave antenna configurations are commonly utilized as applicators for superficial hyperthermia cancer treatment. Patch antennas are considered very interesting radiating elements for treatment of skin cancers because of their intrinsic advantages as small size, low profile, light weight, high integration, and low-cost fabrication. However, the main disadvantage of patch antennas is the narrow bandwidth and low penetration depth capability. The patch antenna bandwidth can be increased by using a metallic cavity, that reduces the losses due to surface waves reduction and improves the radiation performance [122]. Substrate integrated waveguide (SIW) technology is an excellent choice for the realization of the metallic cavity, as it allows to obtain an efficient and low-cost three-dimensional bounding of electromagnetic power via the planar printed board circuits (PCB) technology [100,104,106,109-111,121]. In addition, several studies have shown that metamaterials can be used for the improvement of non-invasive microwave applicators [46-53].

In this chapter, the design and optimization of a split ring resonator (SRR) based metamaterial for microwave therapy of cancer at the frequency $f = 10.7\ GHz$ are reported. This frequency allows a strong microwave absorption of the biological tissue. Generally, the SRR metamaterials are optimized for sensing/imaging applications at different operating frequencies.

The design is focused:

i) to improve the impedance matching of the antenna loaded with human tissue, thus avoiding the impedance mismatch and the formation of stationary waves which are deleterious for an efficient operation of the microwave applicator,

ii) to obtain a better focusing of the electromagnetic power into human tissue.

This feasibility investigation constitutes a preliminary prove of concept for the development of a compact and low-cost microwave applicator for dermatology.

The matching properties of metamaterial are experimentally demonstrated by employing a pre-prototype applicator which consists of a suitable SIW cavity-backed patch antenna with the optimized metamaterial lens based on SRR array. The antenna cavity has been designed by considering SIW technology. Higher gain, efficiency and directivity have been obtained by putting a SRR metamaterial over a patch antenna applicator. The impact of this research lies in the novelty of the proposed device and in its practical potential due to the possibility to refine a set of different SRR geometries. These can be optimized by considering the kind of organ, age, and gender of the patients, for the same source and applicator. The obtained results pave the way towards the construction of an external microwave applicator for skin cancer thermal treatment.

2.2 Design overview

The considered microwave applicator, depicted in Figure 2.1, is a SIW Cavity-Backed Patch antenna, designed and optimized for Ku-Band applications ($10.7 \div 12.7\ GHz$). It consists of a stack structure, a microstrip patch antenna coupled with a circular resonant cavity based on SIW technology. The substrate Rogers Duroid 5880 with low dielectric constant $\varepsilon_r = 2.2$ and low losses $tan\delta = 0.0009$ has been considered for both layers. This antenna combines the attractive features of both SIW cavity-backed and patch antennas with truncated corners. The design has been performed by varying the size of the cavity, the hole diameters, the hole pitch, the patch geometry. All the details pertaining the design of this kind of antenna are reported in [106]. The two cuts on the sides of the rectangular patch were designed to provide a wider frequency band and a frequency downshift. This allows a more compact size. The metallized cavity furtherly broadens the bandwidth and improves the gain of the antenna,

furthermore the SIW technology offers the typical advantages of the standard PCB processes, like easiness fabrication, low cost, compact size, and high integration with the planar circuits. Figure 2.2 shows the layout of SIW cavity-backed patch antenna, whose geometric parameters are listed in Table 2.I.

2.2.1 Metamaterial design

The metamaterial theory reported in Chapter 1 has been applied to roughly identify the geometric parameters of the metamaterial operating at Ku-Band applications. The analytical model for simple split ring resonators has been employed in order to obtain simple and preliminary line guides for the actual design, which is numerically performed via CST Microwave Studio®.

The geometry of the SRR unit cell has been suitably modified and scaled with respect to the literature [46] in order to operate at the resonance frequency of the SIW microwave applicator. Moreover, with respect to [46] the unit cell of the proposed SRR presents a further double ring with splits placed on the opposite side and operates at a different frequency. A complementary configuration, i.e., a couples of coplanar rings written symmetrically with respect to the common centre, has been considered to obtain a resonance frequency close to that of a single ring with the same dimensions, but with a larger magnetic moment due to higher current density. Since they are written on both sides of a dielectric substrate, they are broadside coupled. The analytical model of a single (not complementary) broadside coupled SRR satisfactorily approximates the complementary configuration when the couple of rings are very close each other.

The metamaterial lens consists of an array of complementary broadside coupled split square-rings. The lattice of this inhomogeneous structure is shorter than the guided wavelength of antenna radiation, so the composite behaves as an effective homogeneous medium. Figure 2.3 shows the 3D view (a) and plan front view (b) of the unit cell of the SRR, respectively. The metamaterial lens used as superstrate of the SIW Cavity-Backed Patch antenna is shown in Figure 2.4.

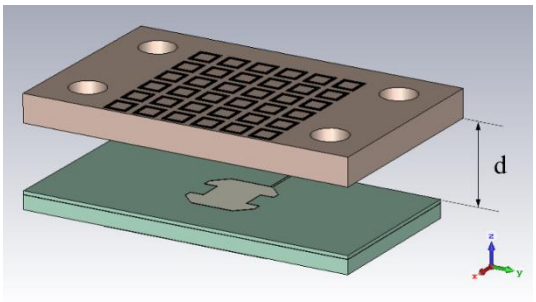

Figure 2.1 Layout 3D view of the microwave applicator with the split ring resonator-based metamaterial superstrate placed on the SIW cavity-backed patch antenna at a distance d [1].

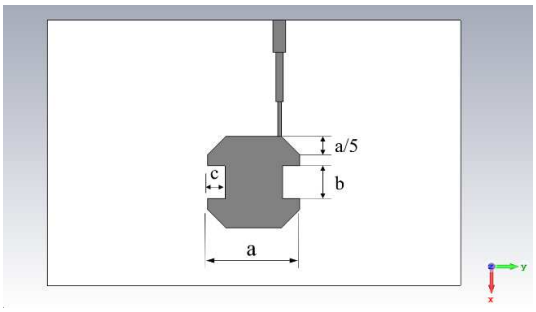

(a)

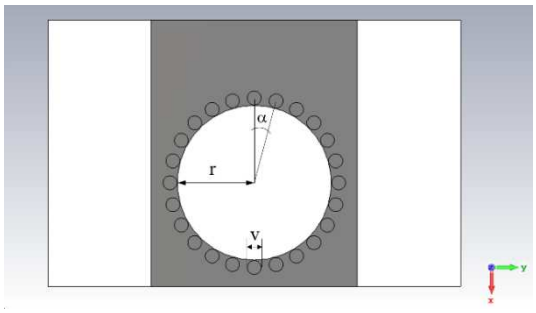

(b)

Figure 2.2 Layout of SIW cavity-backed patch antenna. (a) Top view of the patch antenna and (b) top view of the SIW circular resonant cavity [1].

TABLE 2.I
GEOMETRIC PARAMETERS OF THE SIW CAVITY-BACKED PATCH ANTENNA

Parameter	*Dimension*	*Description*
a	8.00 mm	Length of the patch
b	2.86 mm	Length of the lateral cuts
c	1.50 mm	Width of the lateral cuts
r	6.72 mm	Radius of the SIW cavity
v	0.62 mm	Diameter of the vias
α	15°	Angular distance between the consecutive vias

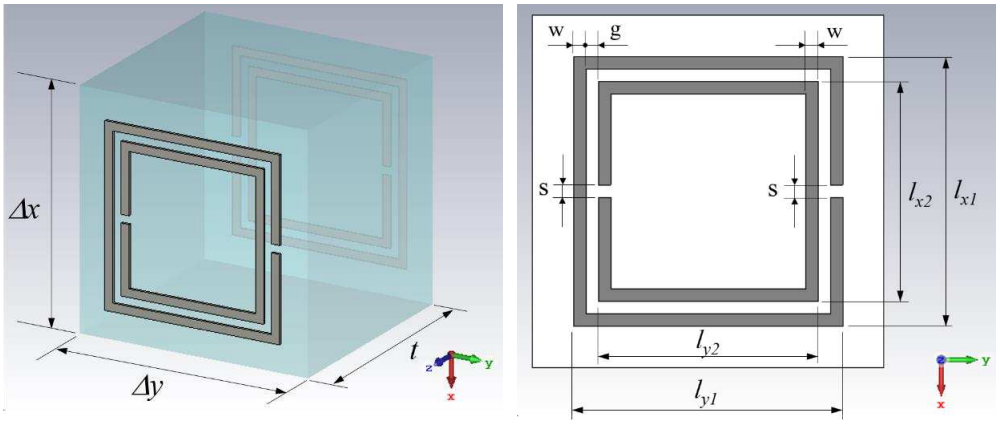

(a) (b)

Figure 2.3 3D model of complementary broadside coupled SRR unit cell designed in CST Microwave Studio®. (a) 3D view and (b) top view [1].

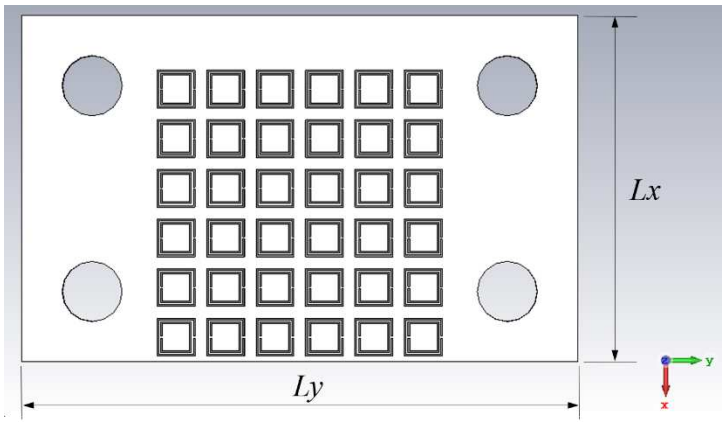

Figure 2.4 Layout of the SRR metamaterial placed as the patch antenna superstrate [1].

2.2.2 Design specifications

The design is numerically performed via CST Microwave Studio®. The dielectric substrate used for the metamaterial is Rogers RO4350B with dielectric constant $\varepsilon_r = 3.48$ and dissipation factor of $tan\delta = 0.004$.

The S_{11} parameter of the microwave applicator placed at distance D from a model of human tissue is simulated to evaluate the lens metamaterial behavior as impedance matching layer. Figure 2.5 shows the sideview of the layout of SIW Cavity-Backed patch antenna covered by the metamaterial lens and at distance D from the biological tissue. The biological tissue considered in the simulation is a slab of skin-fat-muscle, whose electromagnetic parameters at the $f = 11\ GHz$ frequency are listed in Table 2.II [123].

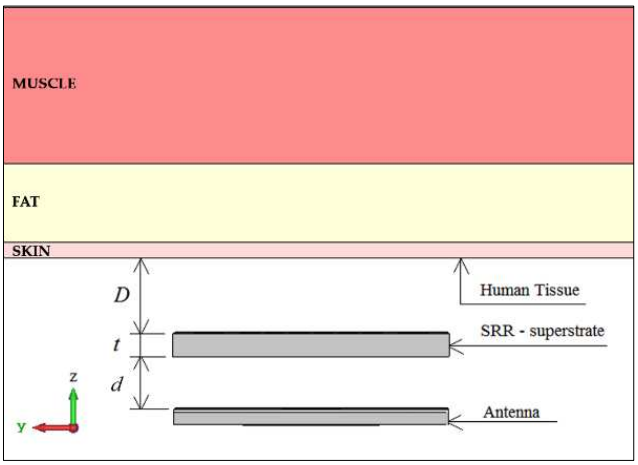

Figure 2.5 Sideview of SIW Cavity-Backed patch antenna with SRR superstrate placed at distance D from human tissue [1].

TABLE 2.II
ELECTROMAGNETIC PARAMETERS HUMAN TISSUE AT $f = 11\ GHz$

Biological Tissue	*El. Conductivity* (σ) $(S\ m^{-1})$	*Permittivity* (ε)
Skin	9.1658	30.313
Fat	0.6567	4.5278
Muscle	12.083	41.419

2.3 Simulation results

The design and optimization of the metamaterial lens has been numerically performed via CST Microwave Studio®. After several simulations, in which the SRR geometry and cell size have been parametrically changed, the optimized geometric parameters are listed in Table 2.III. The optimized SRR metamaterial exhibits resonant frequency range overlapping the operating frequency range of the SIW Cavity-Backed Patch antenna.

The scattering parameter modulus $|S_{11}|$ of the antenna SIW Cavity-Backed patch with SRR superstrate has been simulated for different distances from the biological tissue and the obtained results are compared in Figure 2.6a. It is apparent that the metamaterial placed at $D = 10\ mm$ allows the best impedance matching with the biological tissue.

TABLE 2.III
LIST OF THE GEOMETRIC PARAMETERS OF THE SRR UNIT CELL OF FIGURE 2.1, FIGURE 2.3 AND FIGURE 2.4

Parameter	*Dimension (mm)*	*Description*
Δx	3.20	Length of the unit cell in the x direction
Δy	3.20	Length of the unit cell in the y direction
l_{X1}	2.45	Length of the external SRR in the x direction
l_{y1}	2.45	Length of the external SRR in the y direction
l_{x2}	2.00	Length of the internal SRR in the x direction
l_{y2}	2.00	Length of the internal SRR in the y direction
s	0.11	Split gap of the SRR
w	0.11	Width of the SRR
g	0.11	Length between the complementary SRRs in the xy plane
t	3.04	Length between the broadside coupled SRRs in the z direction
d	6.90	Length between the SIW antenna and the metamaterial lens
L_x	22.40	Length of the metamaterial lens in the x direction
L_y	36.00	Length of the metamaterial lens in the y direction

Figure 2.6b illustrates the simulated scattering parameter modulus $|S_{11}|$ of the SIW Cavity-Backed patch antenna with SRR superstrate placed at distance $D = 10\ mm$ from the human tissue (solid curve) and of the SIW cavity-backed patch antenna with SRR superstrate without tissue (dashed curve). The reduction of the scattering parameter modulus $|S_{11}|$ can be observed over almost the entire frequency range, the metamaterial strongly improves the impedance matching.

Figure 2.7 illustrates the electric field distribution has been simulated in order to evaluate the ability of the proposed microwave applicator to focus the electromagnetic field into biological tissue. Simulated electric field 2D distribution in the yz plane at $f = 11\ GHz$. The metamaterial lens produces a focusing improvement of the electromagnetic field into the skin model in both cases. In the case of SRR superstrate placed at distance $D = 10\ mm$ from the human tissue, the electric field modulus better penetrates along $z-$direction, in both the skin and fat layers, with respect to the case without SRR superstrate. Moreover, the region where the electric field modulus is close to $|E| = 300\ Vm^{-1}$, is more homogeneous in presence of SRR superstrate (Figure 2.7a). It is worth noting the nodal surfaces due to a stationary electromagnetic wave in absence of SRR metamaterial (Figure 2.7b).

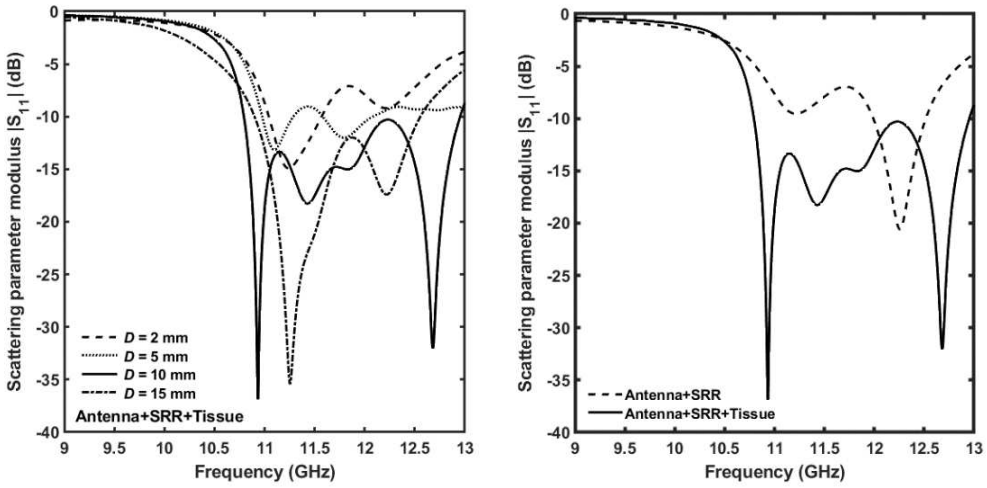

(a) (b)

Figure 2.6 Simulated scattering parameter modulus $|S_{11}|$ (a) of the SIW Cavity-Backed patch antenna with SRR superstrate placed at different distances from the biological tissue and (b) of the SIW Cavity-Backed patch antenna with SRR superstrate placed at distance $D = 10\ mm$ from the human tissue (solid curve) and of the SIW Cavity-Backed patch antenna with SRR superstrate without tissue (dashed curve) [1].

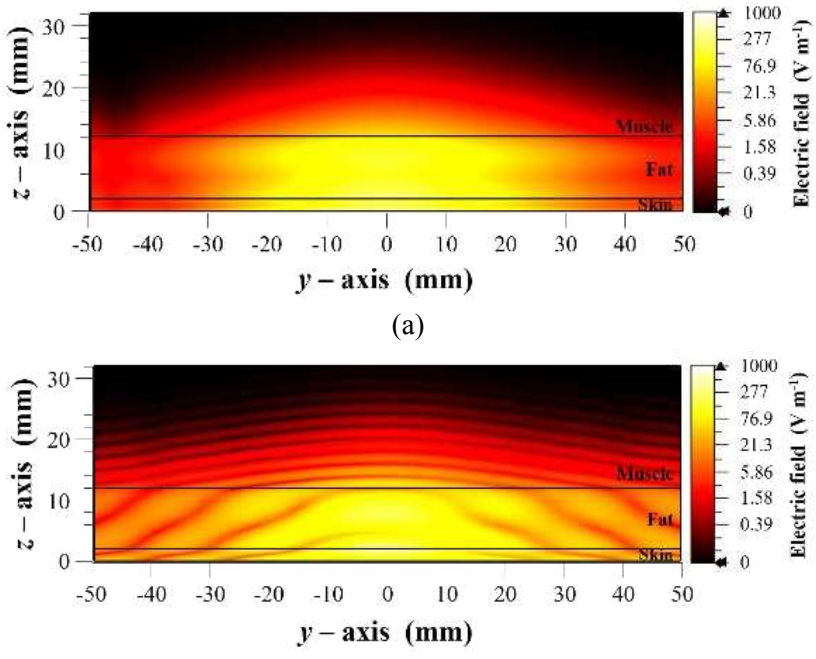

(a)

(b)

Figure 2.7 Simulated electric field 2D distribution in the yz plane at the frequency $f = 11\ GHz$; (a) SIW Cavity-Backed patch antenna with SRR superstrate placed at distance D=10 mm from the human tissue; (b) SIW Cavity-Backed patch antenna placed at distance $D = 10\ mm$ from the human tissue without SRR superstrate [1].

2.4 Measurements

The antenna and metamaterial prototypes have been fabricated by employing the dielectric substrates Rogers Duroid 5880 with $\varepsilon_r = 2.2$ and $tan\delta = 0.0009$ and Rogers RO4350B with $\varepsilon_r = 3.48$ and $tan\delta = 0.004$, respectively and by using a standard PCB process.

Top-view of the SIW cavity-backed antenna and the metamaterial lens are showed in Figure 2.8a, the four holes are fabricated to fixing with suitable screws the metamaterial lens to the SIW antenna and the nuts are screwed in order to the obtain the distance $d = 6.9\,mm$, as shown in Figure 2.8b. The designed thickness of the metamaterial lens, $t = 3.04\,mm$, is achieved by overlaying two layers of dielectric substrate each of thickness $1.52\,mm$.

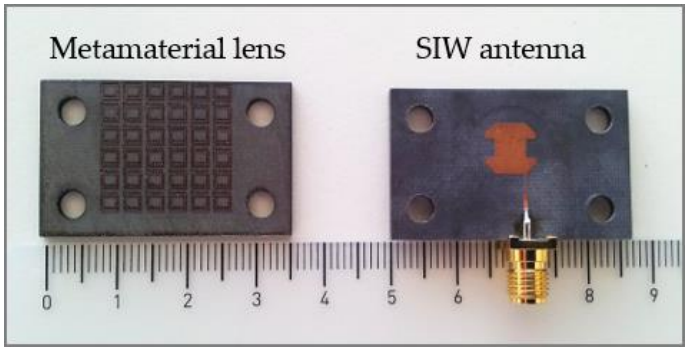

(a)

(b)

Figure 2.8 (a) The metamaterial lens (at left) and SIW Cavity-Backed Patch antenna (at right) prototypes. (b) SIW antenna and metamaterial superstrate assembled and connected at the PNA Network Analyzer [1].

The scattering parameter S_{11} of the device has been measured with the Agilent Technologies N5224A Network Analyzer.

In Figure 2.9 the scattering parameter modulus $|S_{11}|$ of the SIW antenna versus the frequency with metamaterial lens is illustrated, the measurement is performed with the device that irradiates in air (dashed curve) and in the biological tissue of a hand (solid curve) placed at a distance close to $D = 10\ mm$ from the SRR superstrate. The comparison highlights a good impedance matching of the microwave applicator loaded with the biological tissue in the frequency range $10.4 \div 11.5\ GHz$. A scattering parameter modulus $|S_{11}|$ minimum of $|S_{11}|_{min} = -42\ dB$ at the $f = 10.6\ GHz$ frequency has been measured. Moreover, the measured results are in good agreement with simulated one of Figure 2.6b, although we can observe a shift of the resonance frequency of few hundred of MHz, in fact a scattering parameter modulus minimum of $|S_{11}|_{min} = -36.9\ dB$ at the $f = 10.9\ GHz$ frequency has been simulated. The second resonance frequency at $f = 12.7\ GHz$ of the simulated results is less pronounced respect to the experimental results around at $f = 12.3\ GHz$. These differences may be due to manufacturing tolerances and the possible air film between the two layers of the dielectric that constitute the metamaterial lens.

Figure 2.10 shows the measured scattering parameter modulus $|S_{11}|$ of the SIW Cavity-Backed Patch antenna, with (solid curve) and without (dashed curve) the metamaterial superstrate that irradiates in the biological tissue. We can observe that the electromagnetic field of the antenna without metamaterial lens is almost completely reflected from human tissue. We underline that the simulations of Figure 2.7 perfectly agree with the experimental results of Figure 2.9 and Figure 2.10. In particular, in Figure 2.10 the measured scattering parameter modulus $|S_{11}|$ in the case of antenna with SRR metamaterial and tissue (full curve) exhibits a strong dip close to the frequency $f = 10.7\ GHz$. At the frequency $f = 11\ GHz$ the impedance matching is good enough since the measured scattering parameter modulus is close to $|S_{11}| = -14\ dB$. In fact, Figure 2.7a shows a homogeneous propagation/distribution of the simulated electromagnetic field.

Moreover, Figure 2.10 shows that the measured scattering parameter modulus in the case of antenna and tissue without SRR metamaterial (dashed curve) is close to $|S_{11}| = -4\ dB$. This implies an impedance mismatch, the presence of the stationary wave and a not homogeneous distribution of the simulated electromagnetic field with nodal regions. It is in perfect agreement with the simulation in Figure 2.7b. In other words, the SRR metamaterial provides an impedance matching and a consequent suppression of the reflected wave.

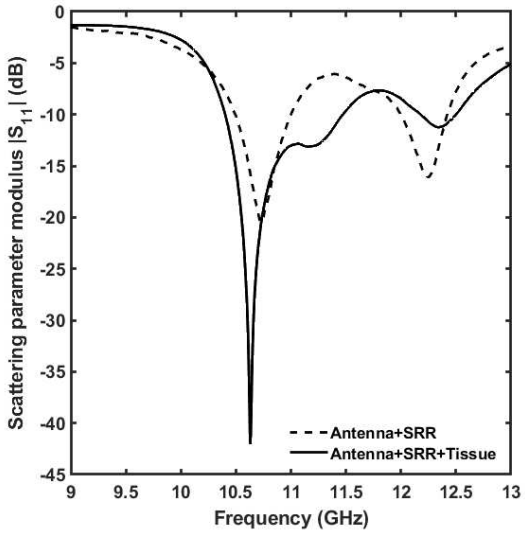

Figure 2.9 Measured scattering parameter modulus $|S_{11}|$ versus frequency of SIW Cavity-Backed Patch antenna with metamaterial lens, that irradiates in biological tissue (solid curve) and in air (dashed curve) [1].

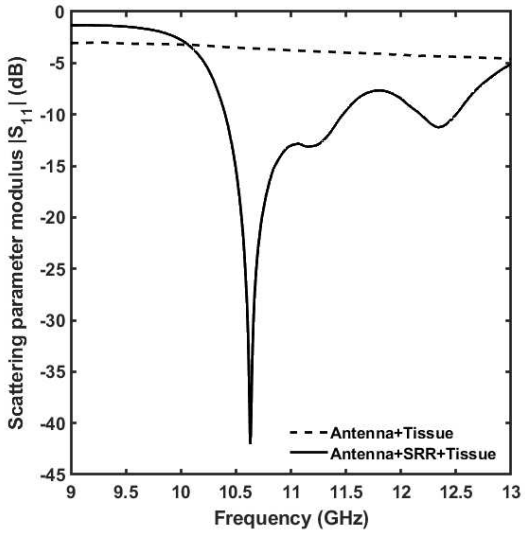

Figure 2.10 Measured scattering parameter modulus $|S_{11}|$ versus frequency of SIW Cavity-Backed Patch antenna with (solid curve) and without (dashed curve) the metamaterial superstrate that irradiates in the biological tissue [1].

The SIW antenna covered by the metamaterial layer has been characterized with the antenna measurement system in anechoic chamber, StarLab SATIMO, shown in Figure 2.11. The measured gain of the antenna with and without the metamaterial is illustrated in Figure 2.12, we can observe that SRR superstrate

produces an improvement of the gain in the frequency range over $f = 11\ GHz$ with an increasement of 4 dB at $f = 12.2\ GHz$.

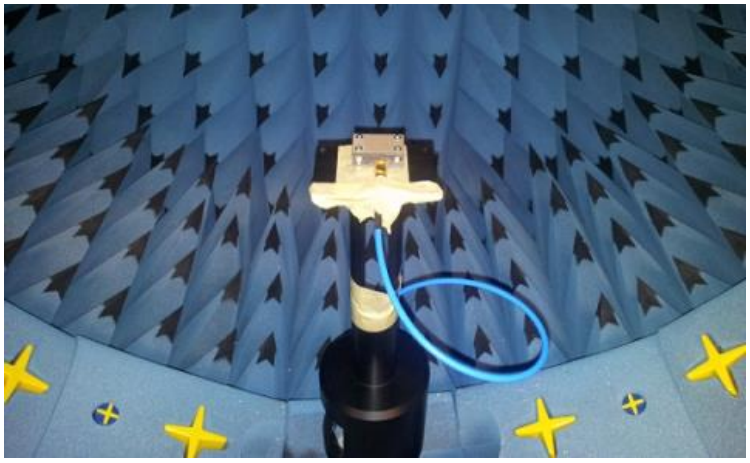

Figure 2.11 SIW Cavity-Backed Patch antenna with metamaterial lens in the anechoic chamber StarLab SATIMO [1].

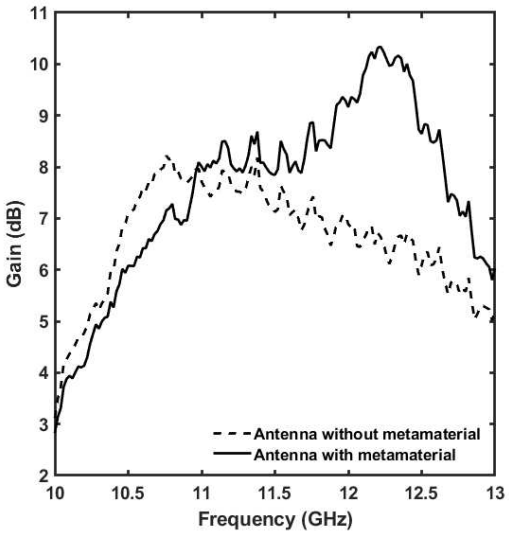

Figure 2.12 Measured gain versus frequency of SIW Cavity-Backed Patch antenna with and without metamaterial [1].

2.5 Comparison with literature

A comparison with other microwave applicators is complex due to the large variety of parameters characterizing the investigations reported in literature, among which the kind of antenna, frequency, kind of metamaterial, applied microwave power and obtained performances characterized in terms of Heating Zone Dimension (HZD), SAR zone, maximum temperature at focusing depth.

For the proposed device the SAR, the peak SAR averaged over the mass $m = 1g$ and over the mass $m = 10g$, the 50% SAR zone, the $42°C$ HZD, for an input power $P = 1\,W$ at $f = 11\,GHz$ frequency are evaluated, in the case of the microwave applicator placed at distance $D = 10\,mm$ from the skin surface of the human tissue. Table 2.IV shows that the obtained results are interesting if compared with literature ones. The reduced HZD zone and high SAR peak evidence the strong focusing obtained via the designed SRR metamaterial. This paves the way for novel promising applications.

TABLE 2.IV
COMPARISON WITH OTHER MICROWAVE APPLICATORS FOR CANCER THERAPY

Ref	*Antenna / Frequency*	*Metamaterial*	*Biological tissue*	*Results*
[15]	Line source extended infinitely 2.45 GHz	Flat left-handed metamaterial (LHM)	Superficial tumour	$T_{max} = 44.7\,°C$ at 0.71 cm below the skin surface $42°C$ HZD of 1 cm × 1.2 cm Electromagnetic field source $43.44\,Vcm^{-1}$
[50]	Multiple Line source extended infinitely 2.45 GHz	Flat left-handed metamaterial (LHM)	Superficial tumour	$42°C\ HZD\ of$ 6.2 cm × 1.3 cm
[52]	Zero-order resonator antenna 434 MHz	Zero-order resonator (ZOR) metamaterial	Superficial tumour	50% SAR zone of 6 cm × 24 cm
[124]	Dipole antenna 4.15 GHz	Flat left-handed metamaterial (LHM)	Breast tissue	$T_{max} = 46\,°C$ at 7.5 cm from the border of the LHM lens
[125]	Multiple microwave sources 6 GHz	Flat left-handed metamaterial (LHM)	Breast tissue	$42°C$ HZD of 1.13 cm × 0.89 cm × 0.61 cm, two LHM lens $42°C$ HZD of 0.87 cm × 0.87 cm × 0.61 cm, four LHM lens
[126]	Microstrip antenna 2.45 GHz	Electromagnetic band gap (EBG)	Breast tissue	Peak $SAR_{1g} = 25\,mWg^{-1}$ Peak $SAR_{10g} = 4.54\,mWg^{-1}$
[127]	Coaxial antenna 2.45 GHz	Left-handed metamaterial (LHM)	Superficial tumour	50% SAR zone of 1.81 cm × 0.32 cm
In this thesis	SIW cavity backed patch antenna Ku-band	Split ring resonator (SRR)	Superficial tumour	Peak $SAR_{1g} = 51.1\,mWg^{-1}$ Peak $SAR_{10g} = 14.2\,mWg^{-1}$ 50% SAR zone of 1.6 cm × 0.2 cm $42°C$ HZD of 1.4 cm × 1.3 cm × 0.4 cm

2.6 Concluding remarks

A metamaterial lens based on SRR has been designed to be employed as a lens to be put on a SIW cavity backed patch antenna in order to improve the impedance matching of the antenna when loaded with human tissue and to enhance the focusing of the electromagnetic field into the biological tissue to be treated.

A prototype has been fabricated employing the standard, low-cost PCB technology and has been characterized by using a Network Analyzer. The simulated scattering parameter modulus of the antenna loaded with the biological tissue with and without metamaterial lens is $|S_{11}| = -37\ dB$ and $|S_{11}| = -14\ dB$ at the $f = 11\ GHz$ frequency respectively. The measured minimum of the scattering parameter modulus $|S_{11}| = -42\ dB$ has been measured at the $f = 10.6\ GHz$ frequency. The experimental results are in good agreement the simulations. The impedance matching improvement has been proved. The electromagnetic field distributions simulated have highlighted the focusing capability of the metamaterial lens. The antenna measurement in the anechoic chamber has confirmed that this kind of SRR lens can find actual application to focus the electromagnetic field of microwave applicators used in dermatology for the thermal therapy of skin cancer.

3 Design of mini-invasive microwave applicators for interstitial hyperthermia cancer treatment

3.1 Introduction

In the case of deep-seated tumour, invasive therapy is generally required. However, microwave (MW) interstitial applicator could be used. Heating at microwave frequencies allows the rapid achievement of thermal lesions extremely localized around the tumour mass alone, resulting in necrosis of cancer cells, avoiding damage to healthy tissues. In addition, the small size of these applicators allows an efficient mini-invasive therapy, which can reduce the traumatic impact of surgery, reduce post-operative recovery time, and thus improve the patient wellness. For internal applicators, the electromagnetic (EM) energy is transferred to biological tissues by intracavitary, percutaneous or laparoscopic techniques, and among the types of radiant elements studied there are monopole, dipole, slot, and helical antennas [23-39]. Moreover, the treatment session can be supervised with the aid of ultrasound scanning, magnetic resonance imaging, or an EM tracking system [128].

In this chapter, various solutions for the design and manufacturing of low-cost mini-invasive interstitial needle applicators are investigated for hyperthermal treatment of hepatic tumour, by considering the patient wellness as primary goal. Some novelty points with respect to the literature are provided, such as:

i) an extensive comparison of different geometries in order to identify the simpler one for an easy fabrication process and device cost reduction,
ii) investigation of different materials by considering a wide range of permittivity, heat capacity, thermal conductivity,
iii) exploitation of 3D-printing technique to construct a simplified insulating section by employing the material E-Shell 300,

iv) insertion of a metamaterial (MTM) lens into the needle microwave applicator is investigated for a more efficient hyperthermia cancer therapy.

3.2 Design overview

Percutaneous microwave applicators are antennas emitting directly into the human tissue, driven with the aid of a hypodermic tube. The tissue is heated by the electromagnetic field absorption. The antenna design plays an essential role in the optimization of the radiation pattern within the treated tissue and of the efficiency of electromagnetic energy transfer. These aspects are also influenced by the dielectric features of the biological medium. A correct impedance matching of the radiating section of the applicator with the human tissue is the first design objective. Indeed, stationary waves and dispersions along the feeding line can cause overheat of the applicator and undesired damages to the surrounding healthy tissues.

The design has involved the following steps:

i) miniaturization of the radiant system, to allow the antenna fitting a biopsy needle for mini-invasive therapy,
ii) choice of a coaxial cable with small section, able to guarantee sufficient power delivering with minimum attenuations,
iii) optimization of the antenna to obtain temperature increase of the target tissue with a quite spherical profile. This last feature is important for an efficient treatment with a scalable size. In fact, it is possible to control the damaged region size by varying the input power and the time duration of the ablation session.

The designed MW applicator is a triaxial antenna [26,32] working at $f = 2.45\ GHz$, in the Industrial, Scientific, and Medical (ISM) frequency band. It is designed for the thermal hepatic tumour ablation [32-33,37-38].

It is schematically composed by three sections:

i) *the radiating section*, a coaxial antenna that terminated with a metallic tip,
ii) *the insulating section*, realized with biocompatible dielectric material that embedded the radiating section. This section helps applicator insertion into the biological tissue, provides mechanical protection,

avoids the adhesion to the necrotized tissue, and improves power coupling with the biological medium.

iii) *a steel hypodermic tube for biopsy* (shaft), in which the antenna is fitted and that allows the percutaneous insertion of the antenna into the biological tissue and gives robustness to the applicator.

Figure 3.1shows the lay-out of the needle microwave applicator for cancer therapy. The bio-electromagnetic design of the antenna has been performed numerically by using the Finite Integration Technique (FIT), and the effects of the interaction between EM fields and biological tissue have been numerically evaluated by using transient thermal analysis, that integrates the bio-heat equation (BHE) [129]. All the phases of the multiphysics design have been performed by numerical simulations with Microwave and Multiphysics modules of CST Studio Suite®.

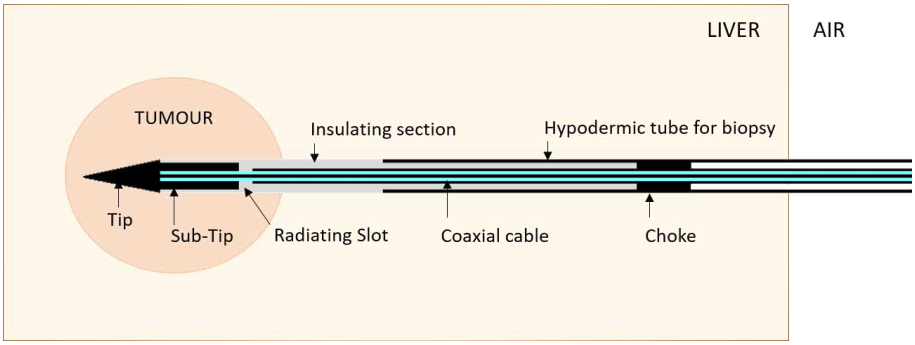

Figure 3.1 Lay-out of the needle microwave applicator for cancer therapy [3].

3.2.1 Electromagnetic design details

In the EM applicator design, the geometrical parameters are defined and optimized in order to minimize the scattering parameter modulus $|S_{11}|$, maximizing the impedance matching of the antenna loaded by the biological tissue and aiming to obtain a spherical shape of the thermal lesion with controlled size. The EM field distribution inside the biological tissue is simulated by evaluating the specific absorption rate (SAR) [23,25].

3.2.1.1 Needle Microwave Applicator design

The starting geometry is shown in Figure 3.2a. It consists of a monopole antenna with a metal conical tip. Different geometries, shown in Figure 3.2b, Figure 3.2c and Figure 3.2d, are simulated in order to optimize power delivery from the antenna to the biological tissues:

i) by introducing a choke [30,36-38], to improve the aspect ratio and the homogeneity of the thermal lesions and to minimize the return loss at the operating frequency,

ii) by adding a cylindrical metal element made of steel (*sub-tip*), that extend the tip inside the insulating section and has allowed the tuning of the resonance frequency,

iii) by considering multi-slot configurations [35,39].

With the aim to design a mini-invasive applicator, the cross section of the antenna has been miniaturized to fit a 14G ($1.74\,mm \div 2.20\,mm$) and a 16G ($1.39\,mm \div 1.69\,mm$) metal biopsy needle applicator.

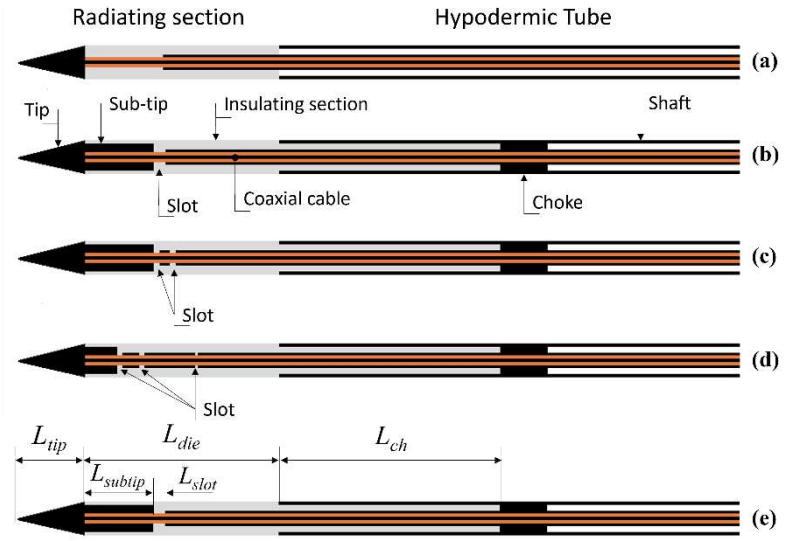

Figure 3.2 Drafts of the designed applicators: (a) starting, (b) choked single slot, (c) choked double slot, (d) chocked triple slot, and (e) dimensions reported in Table 3.III in the Paragraph 3.3.1.1 [2].

3.2.1.2 MTM lens design

A preliminary investigation is carried out on the use of a metamaterial lens in order to obtain a further improvement in the performance of the 16G applicator.

An array of Closed Loop Resonator (CLR) has been considered for the design and optimization of the MTM lens. In particular, two types of geometry have been designed: the Closed Square-Ring Resonator (CSRR) and the Closed Circular-Ring Resonator (CCRR), schematically illustrated in Figure 3.3a e Figure 3.3b, respectively. The metasurface consists of a two-dimensional array of CLR, bended around the radiating section of the needle applicator, to form a cylindrical surface (see Figure 3.3c). Each unit cell consists of two or three conductive

rings printed on the dielectric which encapsulates the radiating section of the applicator. Regarding the CSRR, the width of the metal strip of the two square rings and the distance between them is equal to the value of w, so the length of the inner ring is related to the outer one. In the case of the CCRR, the smaller ring is scaled with respect to the central one by a factor 0.5, and this is scaled by the same scale factor in relation to the outer ring. Therefore, the parameters w_1, w_2, w_3, as well as r_1, r_2, and r_3 are related to each other.

In the numerical investigation, the dimensions of the geometrical parameters have been varied in the ranges listed in Table 3.I. For the optimization of the real model, polytetrafluoroethylene (PTFE) with dielectric constant $\epsilon_r = 2.1$ for the substrate, and copper for the metal loops, have been considered.

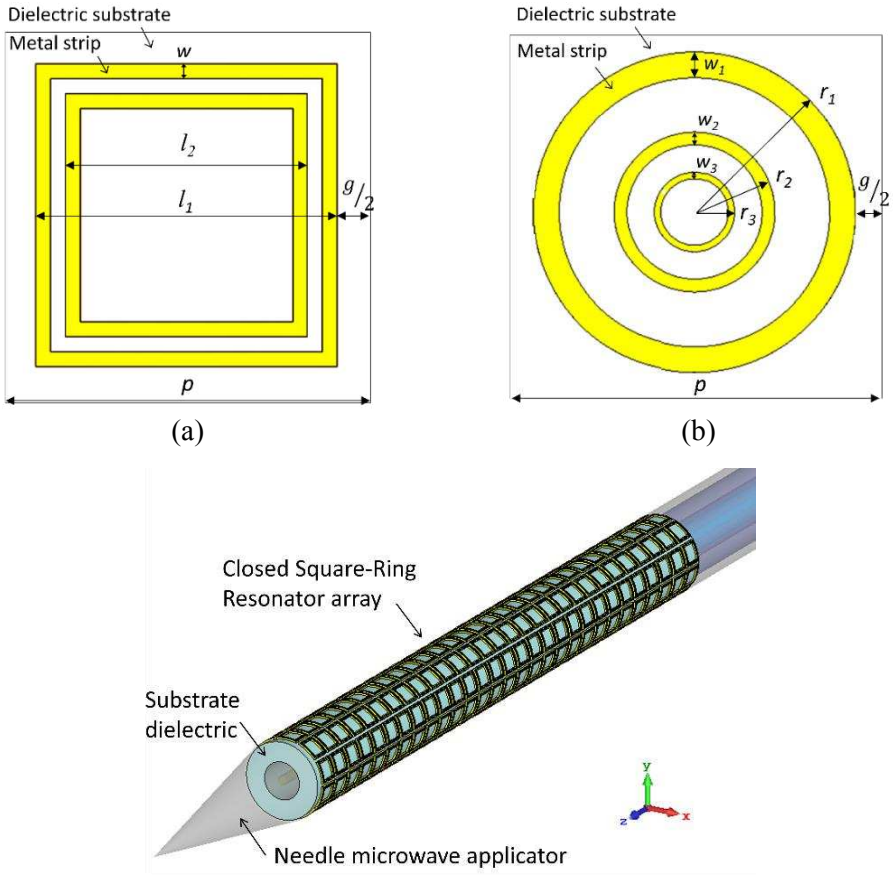

Figure 3.3 Schematic of the metamaterial. (a) Closed Square-Ring Resonator unit cell. (b) Closed Circular-Ring Resonator unit cell. (c) Radiant section of the needle applicator (in transparency) covered by the metamaterial cylindrical surface [4].

TABLE 3.I
PARAMETERS OF THE METAMATERIAL UNIT CELL

Parameter	*Description*	*Range of values for optimization (mm)*
p	unit cell size	$0.25 \div 1.25$
g	gap between the outer rings of two adjacent unit cells	$0.05 \div 0.25$
w_i	metal strip width	$0.004 \div 0.025$
l_i	length of the square-ring	$0.25 \div 1.00$
r_i	radius of the circular-ring	$0.025 \div 0.50$
tk	thickness of the metal strip	$0.025 \div 0.05$

3.2.2 Thermal design details

In the thermal simulations, the blood perfusion effects are considered in order to evaluate the ablation region in an *in-vivo* animal model and a cooling system is considered in order to minimize the heating of the non-target tissue in contact with the applicator along the feeding transmission line. Thermal distribution inside the biological tissue is estimated by exploiting the bio heat equation (BHE) [128], considering such as reference temperature the normal internal body temperature of $T_r = 37°C$. Maximum temperature, profile, and dimensions of the thermal lesions for the different applicators are simulated and compared. The ablation region profile is obtained by using $T = 50\ °C$ isothermal contour line; diameter a and longitudinal length b have been determined, as shown in Figure 3.4. The aspect ratio AR is determined as the ratio of the diameter to the longitudinal length $AR = a/b$, in order to evaluate the applicator capability to produce an ablation region as spherical as possible.

3.2.3 Design specifications

In order to perform realistic simulations, all EM and physical characteristics are considered. The dielectric and physical characteristics of the different materials of the applicator have been taken into account in the simulations, and the electrical characteristics and thermal properties of the liver and the tumour have been considered for a correct evaluation of the effects of the interaction between EM field and biological tissue. Also, the human blood perfusion coefficients are considered to perform *in-vivo* simulations. The liver tissue is modelled as a cube with side $L_{liver} = 100\ mm$. The cancer is modelled as a sphere with diameter $d_{tumour} = 15\ mm$. The liver tissue and the cancer are considered homogeneous and the dielectric and physical parameters, listed in Table 3.II, have been taken

from literature [22,36,130]. However, these features may vary on the patient age, health condition, and gender. In the simulations, the applicator is inserted into the liver tissue cube at $D_T = 65\ mm$ depth.

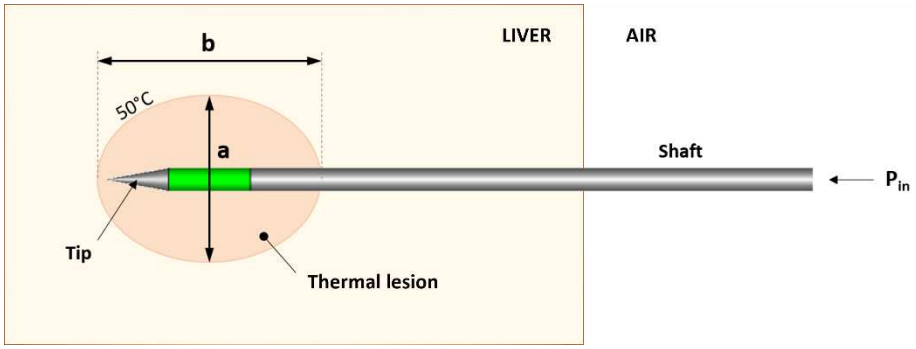

Figure 3.4 Scheme of the ablation zone. The $T = 50\ °C$ isothermal line determinate the boundary of the thermal lesion.

TABLE 3.II
BIOLOGICAL MATERIAL PROPERTIES USED IN THE SIMULATIONS

Physical parameters	*Biological material*	
	Hepatic Tissue [36]	*Hepatic Tumour* [22,130]
Relative permittivity ϵ_r	43.03	54.88
Electric Conductivity σ $(S\ m^{-1})$	1.69	1.99
Density ρ $(Kg\ m^3)$	1041	1045
Thermal Conductivity k $(W\ K^{-1}\ m^{-1})$	0.51	0.50
Heat Capacity c $(KJ\ K^{-1}\ Kg^{-1})$	3.60	3.76
Blood flow Coefficient B $(W\ K^{-1}\ m^{-3})$	68000	36480
Basal Metabolic Rate A $(W\ m^{-3})$	12000	–

3.3 Simulation results

3.3.1 Applicator geometry optimization

3.3.1.1 16G Applicator

The parameters for the applicators are listed in Table 3.III. Their values are identified after several preliminary simulations and by considering fabrication constraints. The applicator lengths are shown in Figure 3.2e.

a) Basis structure

The draft of the first designed applicator is shown in Figure 3.2a. Figure 3.5 shows the modulus of the scattering parameter S_{11} as a function of the frequency f for different L_{slot} values. As expected, the value and the position of the minimum of modulus of the scattering parameter S_{11} varies with L_{slot}. The slot is the antenna aperture providing the electromagnetic power irradiation, its optimal length is strictly related to the operating wavelength, the dielectric properties of the materials, the biological load.

b) Choked structure

Since the metallic shaft causes undesired coupling with the external conductor of the coaxial cable, a choke balun has been introduced, by soldering the hypodermic tube inner surface and the outer conductor of the coaxial cable at one-quarter wavelength from the radiating section [30,36-38], as shown in Figure 3.2b. This configuration improves axial ratio and homogeneity of the thermal lesions and aids the impedance matching.

Figure 3.6 reports the modulus of the scattering parameter S_{11} as a function of the frequency f for different L_{slot} values, for the choked applicator. The best result corresponds to $L_{slot} = 8\,mm$ (solid curve). However, the minimum S_{11} does not correspond to the desired frequency $f = 2.45\,GHz$. Therefore, further refinements must be considered.

c) Choked structure with sub-tip

A steel cylinder covering the coaxial cable in the radiating section, called sub-tip [36,39], with length $L_{subtip} = 5\,mm$, has been added to maximize power delivery to under treatment tissues, see Figure 3.2b.

Figure 3.7 illustrates the modulus of the scattering parameter S_{11} as a function of the frequency f for different values of L_{slot}, for the choked applicator with sub-tip. The best impedance matching occurs for $L_{slot} = 1\,mm$. The simulation for an *in-vivo* model is performed to evaluate the thermal behaviour of the optimized applicator.

Figure 3.8 shows the longitudinal (up) and transversal (down) distribution of the temperature after an ablation time duration $t = 200\,s$. The simulation is carried out considering an average input power $P_{avg} = 20\,W$. The suitable input average power P_{avg} should be chosen considering the desired thermal lesion size. By simulation results, the minimum average power to ablate the whole cancer sphere of diameter $d_{tumour} = 15\,mm$ is $P_{avg} = 20\,W$, since the thermal lesion is defined with the isothermal line at $T = 50°\,C$. This value is identified via a

number of simulations by increasing the input average power in the range from $P_{avg} = 2\ W$ to $P_{avg} = 30\ W$. The choked applicator has a simpler geometry than that of the choked applicator with sub-tip. It has been investigated with the aim to identify an easier construction geometry. However, its response is strongly affected by slot length. Consequently, the optimized choked applicator with sub-tip has been considered.

TABLE 3.III
OPTIMIZED PARAMETERS OF THE 16G APPLICATOR OF FIGURE 3.2E

Parameter	*Value (mm)*	*Description*
L_{tip}	5	Tip length
L_{die}	15	Insulating section length
L_{slot}	1	Radiating slot gap
L_{subtip}	5	Sub-tip length
L_{ch}	21.1	Choke length
d_{tip}	1.69	Base tip diameter
d_{die}	1.69	Insulating section diameter
$d_{in,sh}$	1.39	Shaft inner diameter
$d_{out,sh}$	1.69	Shaft outer diameter
d_{cable}	0.787	Coaxial cable outer conductor maximum diameter
$d_{out,coax}$	0.6027	Coaxial cable outer conductor minimum diameter
$d_{in,coax}$	0.2032	Coaxial cable inner conductor diameter

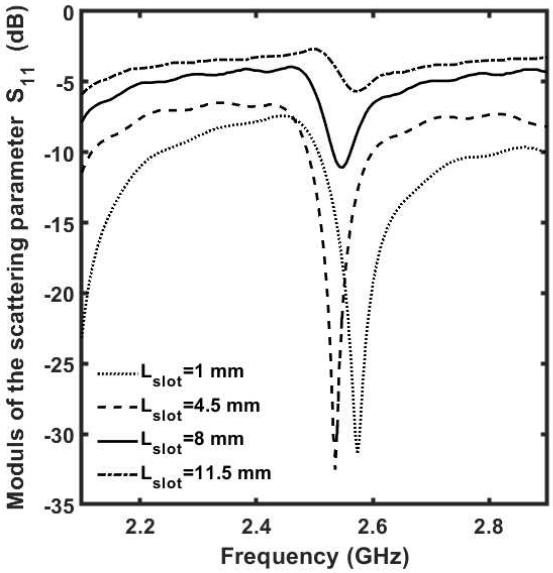

Figure 3.5 Modulus of the simulated scattering parameter S_{11} as a function of the frequency f, for different L_{slot} values. Starting designed 16G MW applicator, Figure 3.2a [2].

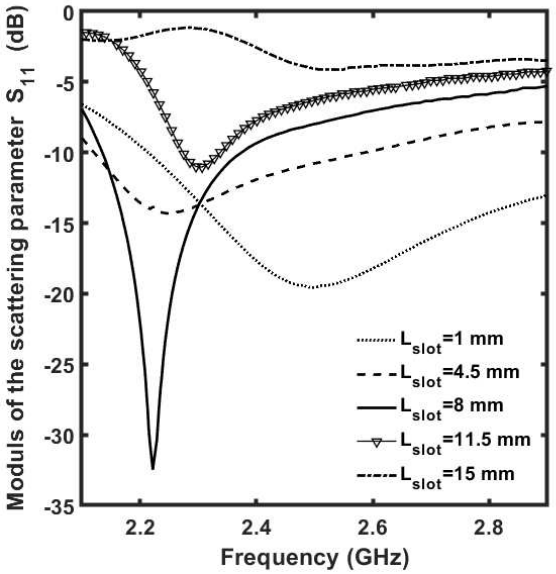

Figure 3.6 Modulus of the simulated scattering parameter S_{11} as a function of the frequency f, for different L_{slot} values. Choked applicator 16G MW applicator without sub-tip [2].

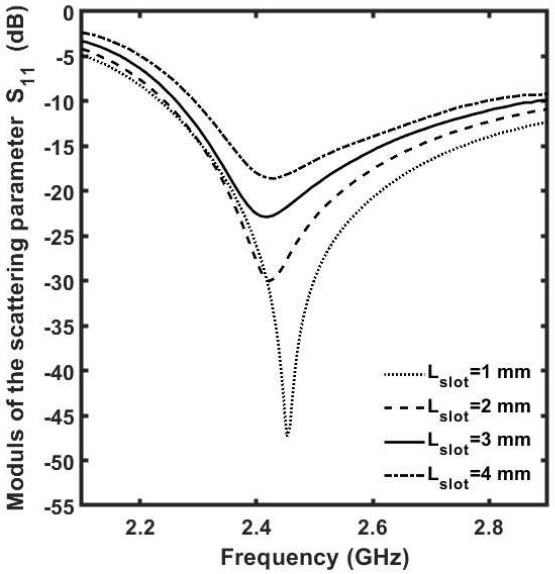

Figure 3.7 Modulus of the simulated scattering parameter S_{11} as a function of the frequency f, for different L_{slot} values. 16G MW applicator, Figure 3.2b [2].

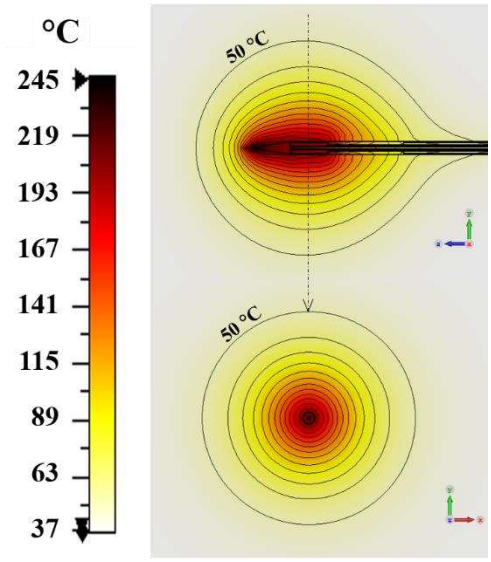

Figure 3.8 Temperature distribution simulated into the hepatic tissue after an ablation time duration $t = 200\ s$, for average power $P_{avg} = 20\ W$. 16G MW applicator, Figure 3.2b [2].

3.3.1.2 14G Applicator

An antenna to fit a 14G hypodermic tube has been investigated, to reduce construction costs, while obtaining comparable performances and maintaining mini-invasive design. Its slightly bigger radius allows a simpler assembly operation and an easier implementation of a cooling circuit. The 14G hypodermic tube has inner radius $d_{in,sh} = 1.74\ mm$ and outer radius $d_{out,sh} = 2.2\ mm$. Three multi-slot applicators have been designed: choked single, double, and triple slot antennas, illustrated in Figure 3.2b, Figure 3.2c and Figure 3.2d, respectively. They have been optimized and their performances in terms of impedance matching with the biological tissue and axial ratio of the thermal lesion are compared with the 16G choked single slot applicator.

Figure 3.9 shows the comparison of the modulus of the scattering parameters S_{11} for the three geometries of the 14G applicator and the single slot 16G applicator; the simulated scattering parameters at $f = 2.45\ GHz$ are $S_{11} = -28.75\ dB$, $S_{11} = -56.43\ dB$, and $S_{11} = -39.55\ dB$, $S_{11} = -47.34\ dB$ for 14G choked single slot, 14G double slot, 14G triple slot, and 16G single slot antennas respectively.

The ablated zone sizes for single, double, and triple configurations as a function of the ablation time duration t has been evaluated via an accurate simulation. Figure 3.10 shows the axial ratio for the three configurations as a function of the ablation ratio for the three configurations as a function of the ablation time

duration t, when the applicator is fed by an average input power $P_{avg} = 20\ W$. The 14G single slot and the 14G double slot applicators allow an axial ratio bigger than that obtained with the 14G triple slot one, whereas the 16G single slot antenna shows the best result. The 14G applicator demonstrates a good impedance matching with the biological load also when the tumour diameter varies. The applicator impedance matching when it is inserted into four different tumour diameters is depicted in Figure 3.11.

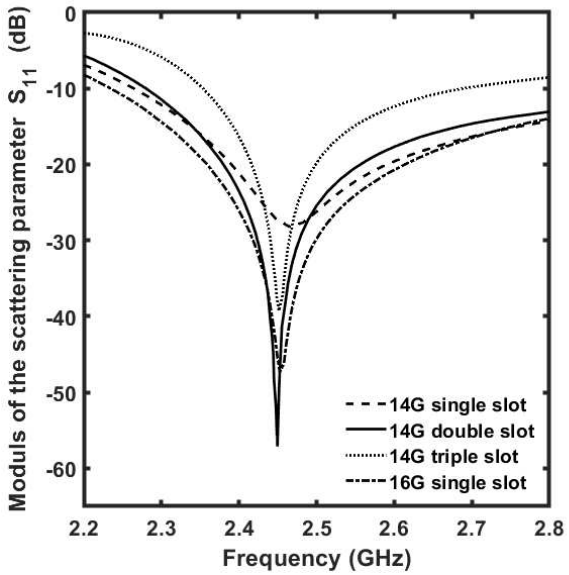

Figure 3.9 Modulus of the simulated scattering parameter S_{11} as a function of the frequency f, average input power $P_{avg} = 20\ W$. 16G MW applicator, Figure 3.2b vs. 14G MW applicator, Figure 3.2b, 14G MW applicator, Figure 3.2c, and 14G MW applicator, Figure 3.2d [2].

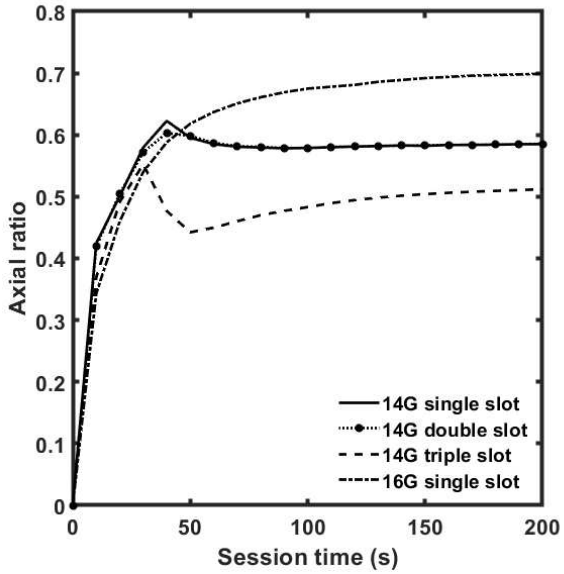

Figure 3.10 Simulated axial ratio of the thermal lesion as a function of the ablation time duration t, average input power $P_{avg} = 20\ W$. 16G MW applicator, Figure 3.2b vs. 14G MW applicator, Figure 3.2b, 14G MW applicator, Figure 3.2c, and 14G MW applicator, Figure 3.2d [2].

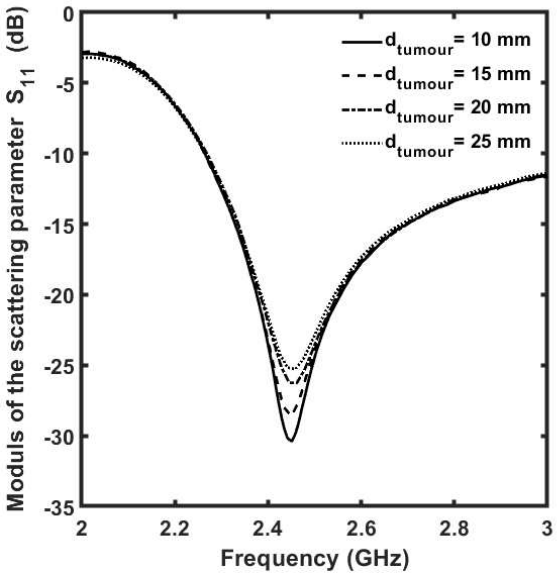

Figure 3.11 Modulus of the simulated scattering parameter S_{11} as a function of the frequency f, for different tumour diameters d_{tumour}. 14G MW applicator, Figure 3.2b [2].

3.3.2 Dielectric material optimization

In the simulations, PTFE with a nominal permittivity of $\varepsilon_r = 2.1$ is used for the insulating section. However, to evaluate the possibility of fabricating this section by 3D-printing technology, the effects of the changes in the physical parameters of the dielectric on the applicator performance have been examined. In particular, the dielectric constant ε_r, thermal conductivity k and thermal capacity c variations have been investigated. For the study of the insulating section, the 14G choked single slot MW applicator has been considered. The geometrical dimensions of the applicator are $d_{in,sh} = 1.74\ mm$, $d_{out,sh} = 2.2\ mm$, $d_{in,coax} = 0.3535\ mm$, $d_{out,coax} = 0.965\ mm$, $d_{cable} = 1.19\ mm$, $d_{tip} = 2.2\ mm$, and $L_{slot} = 1\ mm$.

3.3.2.1 Study on the permittivity of the insulating section

Changes in the dielectric constant of $\pm 20\%$ around the nominal value $\varepsilon_r = 2.1$ is examined. Figure 3.12 shows the modulus of scattering parameter S_{11} as a function of frequency f, when different insulating section permittivity ε_r values are considered. A bigger dielectric constant allows smaller devices. For the permittivity value of $\varepsilon_r = 2.52$ a suitable choke length, equal to $L_{ch} = 19.1\ mm$ is identified instead of $L_{ch} = 21.1\ mm$ identified for $\varepsilon_r = 2.1$ for the same operation frequency $f = 2.45\ GHz$.

3.3.2.2 Study on the thermal conductivity and capacity of the insulating section

The effects of the change in the thermal conductivity and capacity of $\pm 10\%$ around the nominal values of $k = 0.2\ W\ m^{-1}\ K^{-1}$ and $c = 1\ kJ\ K^{-1}\ kg^{-1}$ are examined.

Figure 3.13 depicts the dimensions and axial ratio of the thermal lesion as a function of the ablation time duration t, when different thermal conductivity k values are considered, keeping the thermal capacity c constant at the nominal value.

Figure 3.14 depicts the dimensions and axial ratio of the thermal lesion as a function of the ablation time duration t, when different thermal capacity c values are considered, keeping the thermal conductivity k constant at the nominal value. By considering the thermal lesion sizes and the axial ratio at session time $t = 200\ s$, the following evidences can be observed:

i) for an increase of $+10\%$ of thermal conductivity k, an increase of $+1.7\%$ of the thermal lesion longitudinal length is obtained, the

diameter of the thermal lesion does not vary, thus the axial ratio decreases of -1.07%;

ii) for an increase of $+10\%$ of the thermal capacity c an increase of $+1.05\%$ of the thermal lesion longitudinal length and of $+0.65\%$ of the thermal lesion diameter is obtained, thus the axial ratio increases of $+0.4\%$.

3.3.2.3 Study on the material of the insulating section

Innovative 3D additive printing techniques have been considered for the manufacturing of the insulating section, in order to reduce costs and simplify the fabrication process. To evaluate the feasibility of ad-hoc constructed insulating sections, a photo-reactive polymer for additive manufacturing, used for medical applications (Envision TEC E-Shell 300) has been considered for the 14G applicator instead of the PTFE. The new material has been characterized, via a dielectric measurement set-up based on open-ended coaxial probes, SPEAG DAK probe, and a vector network analyser (VNA) Field Fox Keysight Technologies [131] (see Figure 3.15). The measured real permittivity and loss tangent of the E-Shell 300 in the frequency range $f = 2 \div 3\ GHz$ are $\varepsilon_r = 2.73$ and $tan\delta = 0.0278$.

Figure 3.16 shows the simulated modulus of scattering parameter S_{11} as a function of the frequency f, for the insulating section made of PTFE (solid curve) and the E-Shell 300 series (dash-dot curve). The impedance matching with E-Shell 300 has been optimized, varying the choke length L_{ch}. The minimum of the scattering parameter is $S_{11} = -27.2\ dB$, for $L_{ch} = 18\ mm$.

Figure 3.17 shows the axial ratio of the thermal lesion as a function of the ablation time duration t. It is bigger for the PTFE case, allowing a thermal lesion closer to a theoretical sphere. This condition is more convenient, because allows to avoid damage of healthy tissue along the needle applicator.

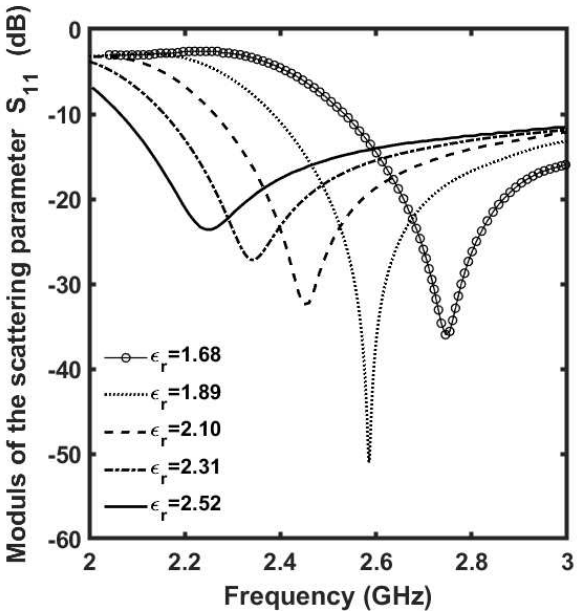

Figure 3.12 Modulus of the simulated scattering parameter S_{11} as a function of the frequency f, as the insulating section permittivity varies. 14G MW applicator, Figure 3.2b [2].

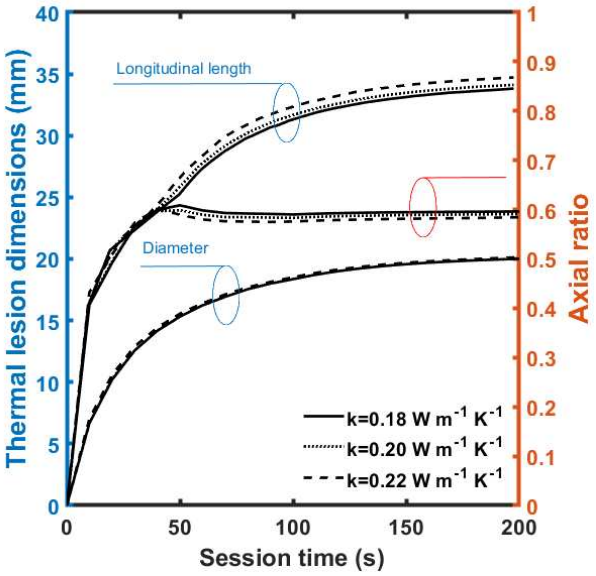

Figure 3.13 Simulated dimensions and axial ratio of the thermal lesion as a function of the ablation time duration t, for different values of thermal conductivity k; $c = 1\ kJ\ K^{-1}\ kg^{-1}$; average power $P_{avg} = 20\ W$. 14G MW applicator, Figure 3.2b [2].

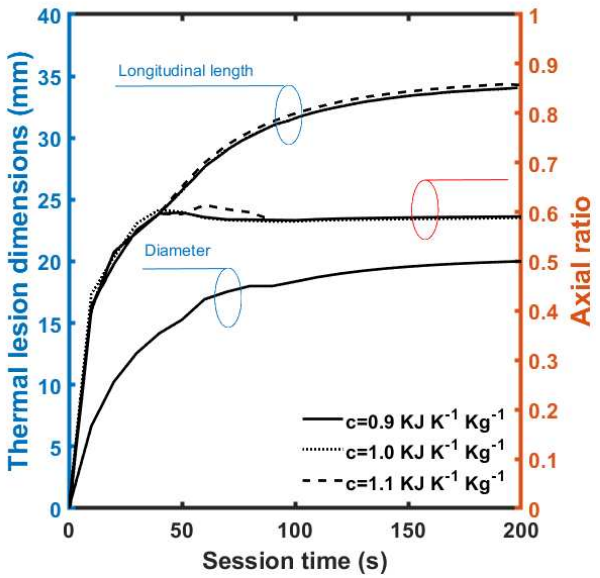

Figure 3.14 Simulated dimensions and axial ratio of the thermal lesion as a function of the ablation time duration t, for different values of thermal capacity c; $k = 0.2\ W\ m^{-1}\ K^{-1}$; average power $P_{avg} = 20\ W$. 14G MW applicator, Figure 3.2b [2].

Figure 3.15 Set-up for the dielectric characterization of a biocompatible 3D printing material for the insulating section and measured sample

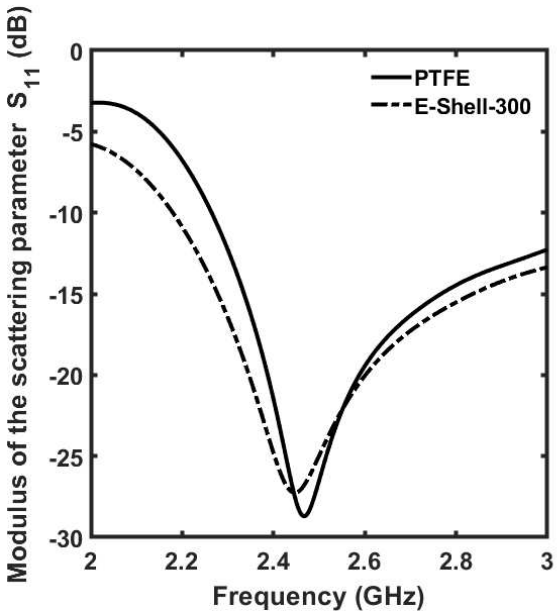

Figure 3.16 Modulus of the simulated scattering parameter S_{11} as a function of the frequency f, for PTFE (solid curve) and E-Shell 300 (dash-dot curve). 14G MW applicator, Figure 3.2b [2].

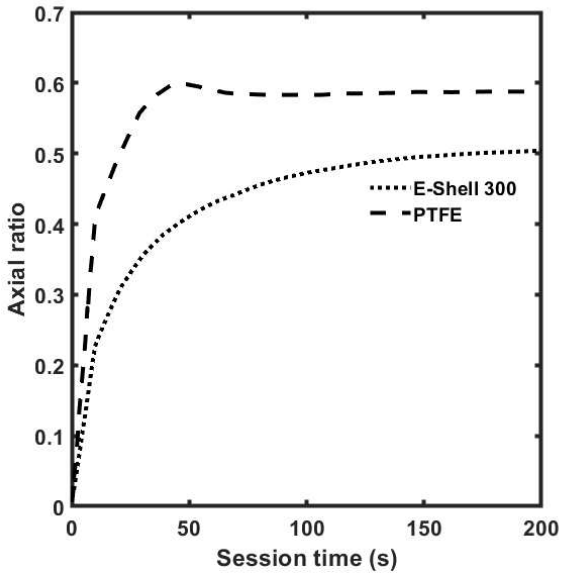

Figure 3.17 Simulated axial ratio of the thermal lesion as a function of the ablation time duration t, average power $P_{avg} = 20\,W$. 14G MW applicator, Figure 3.2b [2].

3.3.3 Effects of cooling system on MW heating

To improve the axial ratio of the ablation zone by minimizing the harmful overheating of the biological tissue adjacent to the shaft, caused by the by thermal propagation and by the formation of parasite currents, a cooling circuit has been considered. The cooling is typically obtained with the flow of a refrigerant fluid in cooling channels located into the hypodermic tube. In particular, an open-loop cooling circuit, employing a peristaltic pump, and allowing a suitable flux of saline solution, is designed in order to stabilize the temperature at $T = 37°C$ in the needle shaft. Moreover, a better control of the applicator performance during the therapeutic treatment could be possible with a real time temperature monitoring system integrated with the applicator, e.g., an optical fiber temperature sensor [132].

In the simulations, the cooling circuit model has been approximated with an ideal constant temperature source put into the hypodermic tube. In particular, the cooled region goes from the MW generator to the choke, i.e., the area to the left of the choke in Figure 3.2b, Figure 3.2c and Figure 3.2d. The considered cooling fluid is water with a temperature fixed to $T_b = 37\ °C$, close to the normal body temperature. The effects of the cooling circuit on the thermal performance of the 14G and 16G single slot MW applicators of Figure 3.2b have been evaluated by simulations with and without the cooling circuit.

Figure 3.18 shows the isothermal curves simulated in the case of the 14G applicator. The thermal lesion shape obtained for the needle with cooling circuit is more spherical (Figure 3.18a) than that pertaining to other case (Figure 3.18b), where the typical comet-tail profile can be observed. To further increase the thermal lesion sphericity, the simulated cooling circuit has been extended to the radiating section. Temperature distribution, shape and dimensions of the thermal lesion change due to the extended cooling circuit increasement as shown in Figure 3.19. The axial ratio for the applicator with extended cooling circuit is $AR = 0.73$.

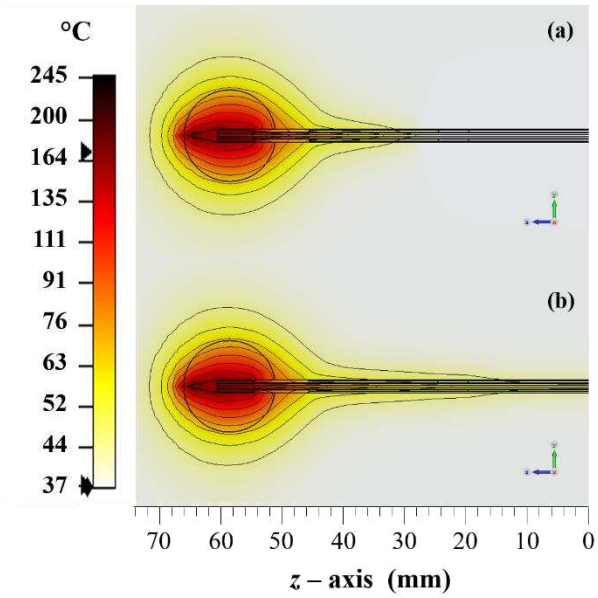

Figure 3.18 Temperature distribution of the irradiated tissue simulated in the longitudinal section with an average power in input of $P_{avg} = 20\ W$. 14G MW applicator, Figure 3.2b, (a) with and (b) without cooler circuit [2].

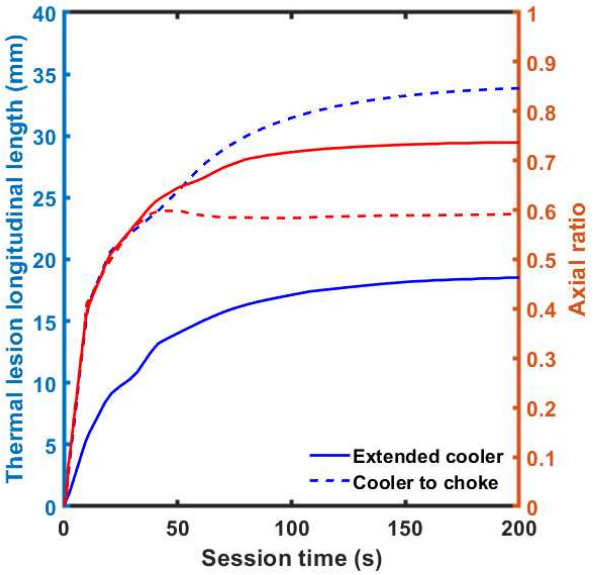

Figure 3.19 Simulated longitudinal length and axial ratio of the thermal lesion as a function of ablation time duration t of the 14G MW applicator, Figure 3.2b, with cooler stopped at choke (dashed curve) and extended at slot (solid curve), average power $P_{avg} = 20\ W$ [2].

3.3.4 16G applicator optimization for the prototyping

The sequence of the investigation results reported in the previous paragraphs constitute the basis of a "trial and error" design approach, allowing to optimize the geometries of these antennas. In the Table 3.IV, the simulations results related to all designed applicators are reported.

The choked single slot with sub-tip version is chosen for the construction. An almost spherical thermal lesion close to the antenna radiation section has required more elaborate geometry and more complicate fabrication process.

The fabrication of the applicators has presented critical issues due to the limits of the available technology. In particular, the assembly of the radiating section with the tip/sub-tip section and with the shaft proved to be particularly critical for the prototyping of the 16G applicator. Therefore, some changes have been made with the aim of simplifying prototyping:

i) the radiating section has been simplified, modifying the joint between the sub tip and the coaxial cable,
ii) inside the shaft, between the radiating section and the choke, the PTFE dielectric material has been removed.

The simplified geometry has been further optimized, considering air in place of PTFE removed from the shaft in the simulations, by varying only the sub-tip length L_{subtip}, the slot length L_{slot} and the choke length L_{ch}. The optimized lengths are $L_{subtip} = 4\ mm$, $L_{slot} = 3\ mm$ and $L_{ch} = 28\ mm$, the other dimensions are reported in Table 3.III. Figure 3.20 shows the drafts of the modified 16G applicator.

In order to compare the simulation results with experimental one, *ex-vivo* thermal simulations are performed by neglecting the blood perfusion coefficients and metabolic rate. Figure 3.21 shows the longitudinal section of the temperature distribution into the hepatic tissue simulated after an ablation duration time of $t = 600\ s$, with a power supply of $P = 20\ W$. A thermal lesion at $T = 50°C$ of $34\ mm \times 41\ mm$ axial sizes is simulated.

TABLE 3.IV
SIMULATION RESULTS WITH DIFFERENT ANTENNA GEOMETRIES

Parameter	*Type of applicator*				
	16G single slot	*14G single slot*	*14G single slot with E-Shell 300*	*14 G dual slot*	*14 G triple slot*
Minimum scattering parameter modulus (dB)	– 47.3	– 28.7	– 27.2	– 56.4	– 39.6
Maximum SAR (averaged over the mass $m = 1\ g$, at $P_{avg} = 20\ W$) (kW/kg)	5.61	5.19	5.12	5.12	4.97
Maximum temperature (at $P_{avg} = 20\ W, t = 200\ s$) $(°C)$	244	184	172	182	175
Lesion longitudinal length (at $P_{avg} = 20\ W, t = 200\ s$) (mm)	36.7	34.2	39.0	34.3	39.2
Lesion diameter (at $P_{avg} = 20\ W, t = 200\ s$) (mm)	28.2	20.0	19.8	20.1	20.1
Axial Ratio (at $P_{avg} = 20\ W, t = 200\ s$)	0.77	0.58	0.51	0.59	0.51

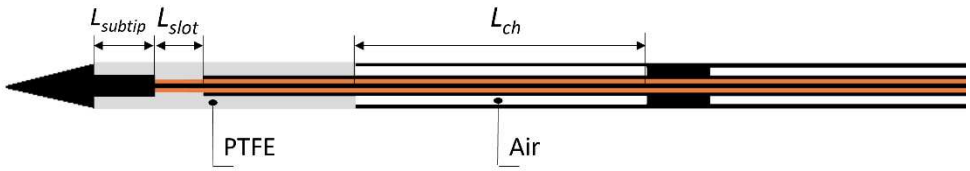

Figure 3.20 Draft of the 16G choked single slot applicator optimized for the prototyping

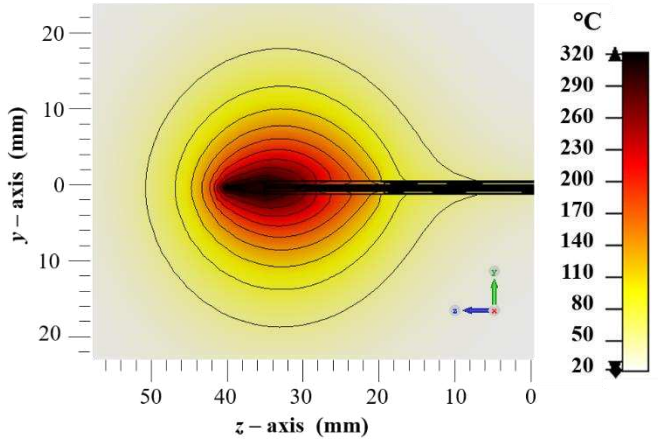

Figure 3.21 Longitudinal section of the temperature distribution into the hepatic tissue simulated with a power supply of $P = 20\ W$, after an ablation duration time of $t = 600\ s$. *Ex-vivo* thermal simulation of the 16G needle MW applicator optimized for the prototyping [3].

3.3.5 MTM lens optimization

For the design and optimization of the metamaterial lens, the 16G applicator modified for the prototyping, shown in Figure 3.20, has been considered in the simulations. The geometry and dimensions of the applicator are reported in the Paragraph 3.3.4. Only the PTFE insulating section has been slightly modified, by reducing the diameter to allow the insertion of the MTM lens.

Figure 3.22 shows the modulus of the scattering parameter S_{11} as a function of the frequency f simulated by considering different metal strip widths w and compared with that of the applicator without the MTM, for the microwave needle applicator with CSRR metalens.

Figure 3.23 shows the modulus of the scattering parameter S_{11} as a function of the frequency f simulated by considering lengths of the radius of the outer circle r_1 and compared with that of the applicator without the MTM, for the microwave needle applicator with CCRR metalens.

All numerical simulations highlighted that the insertion of the MTM lens does not significantly change the operating frequency around $f = 2.45\ GHz$ of the applicator. Furthermore, as expected, the value of the minimum of modulus of the scattering parameter S_{11} varies with the dimensions of the geometric parameters. Considering the dielectric characteristics of the biological tissue in which the EM waves propagate and the operating frequency of the applicator, the unit cell size p has been varied from $0.2\ mm$ to $2\ mm$. The best results have been obtained for values around $0.25\ mm \div 0.5\ mm$.

Three case studies, concerning a 16G microwave needle applicator with MTM lens, are reported:

i) CSRR-based MTM lens, identified as CSRRa with lattice length of $p = 0.51\ mm$,
ii) CSRR-based MTM lens, identified as CSRRb, with lattice length of $p = 1\ mm$,
iii) CCRR-based MTM lens, with lattice length of $p = 0.25\ mm$.

All parameters related to the three metalenses are reported in the Table 3.V.

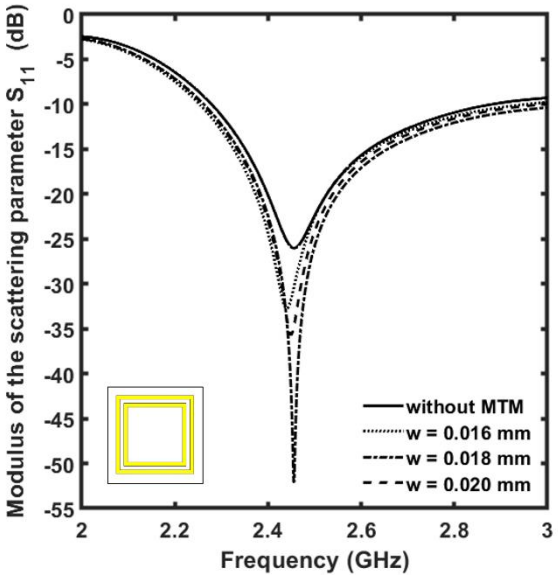

Figure 3.22 Modulus of the simulated scattering parameter S_{11} as a function of the frequency f of the 16G applicator without and with CSRR MTM lens for different metal strip widths w, with $p = 0.51\ mm$ and $g = 0.06\ mm$

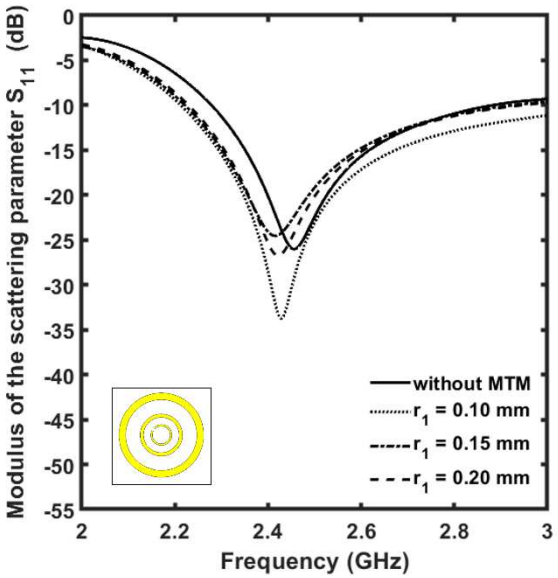

Figure 3.23 Modulus of the simulated scattering parameter S_{11} as a function of the frequency f of the 16G applicator without and with CCRR MTM lens for different lengths of the radius of the outer circle r_1, with $w_1 = 0.016\ mm$ and $g = 0.05\ mm$

TABLE 3.V
PARAMETERS OF THREE OPTIMIZED MTM LENSES

Parameter	*Metamaterial*		
	CSRRa (mm)	*CSRRb (mm)*	*CCRR (mm)*
p	0.51	1.00	0.25
g	0.06	0.05	0.05
w	0.018	0.018	–
w_1	–	–	0.016
l_1	0.45	0.95	–
r_1	–	–	0.1

3.3.5.1 Improvement in impedance matching

The comparison of the of the scattering parameter modulus S_{11} simulated for the microwave needle applicator with the three MTM lenses and without MTM lens highlights an improvement of the impedance matching around the center frequency of the ISM band, as shown in Figure 3.24. The numerical results are summarized in Table 3.VI. The CSRRa MTM lens introduces no shift in the operating frequency and the minimum of the scattering parameter modulus S_{11} is significantly reduced. For the CCRR MTM lens, the enhancement is less pronounced and negligible frequency shift occurs, the bandwidth is increased by about $160\ MHz$. The CSRRb MTM lens exhibits an intermediate behaviour with respect to the two previous cases. It allows an easier fabrication due to the larger size.

3.3.5.2 Increase of the absorbed power loss

In order to evaluate the biological effects of the insertion of the MTM lens on the microwave needle applicator in terms of the microwave energy absorbed by the hepatic tissue and tumour, the Specific Absorption Rate (SAR) and the power loss have been numerically estimated. The SAR value, averaged over the mass $m = 1\ g$, has been calculated considering a peak power in input to needle applicator of $P_{pk} = 20\ W$, the power loss has been normalized to the input power, and the results are listed in Table 3.VII.

By comparing the results of Table 3.VII, the insertion of the metalens on the needle applicator allows a slight increase in the maximum SAR values, both in the healthy liver and in the tumour, located near the radiating section of the same, while globally the mean value of SAR and absorbed EM power is increased in the tumour tissue and reduced in the healthy tissue. These improved trends are confirmed for all three MTM lens designs reported here, although more evident for the metalens based on CSRRa and CCRR.

These results indicate a preliminary performance improvement opportunity and pave the way for further study to subsequent developments.

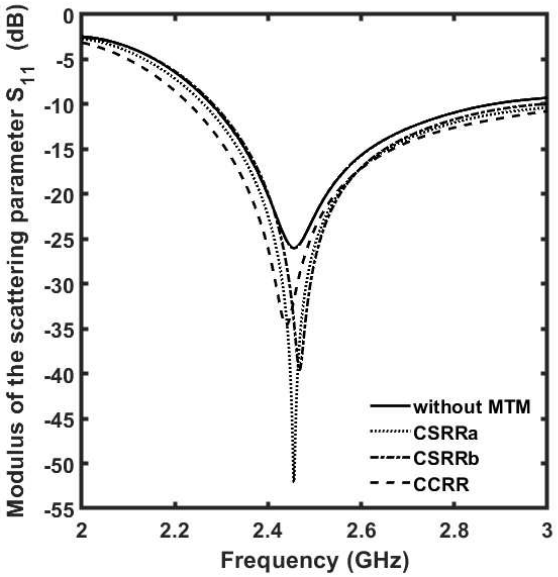

Figure 3.24 Modulus of the simulated scattering parameter S_{11} as a function of the frequency f of the 16G applicator without and with MTM lens based on Closed Square-Ring Resonator and Closed Circular-Ring Resonator [4].

TABLE 3.VI
CSRRA, CSRRB AND CCRR PARAMETERS

Parameter	*Needle applicator*			
	no MTM	*CSRRa*	*CSRRb*	*CCRR*
Minimum modulus of the scattering parameter S_{11} (dB)	-26.0	-52.1	-39.6	-34.6
Frequency of the minimum modulus of the scattering parameter S_{11} (GHz)	2.456	2.456	2.468	2.439
Modulus of the scattering parameter modulus S_{11} at $f = 2.45\ GHz$ (dB)	-25.9	-42.7	-31.6	-33.1
Bandwidth at $-10\ dB$ (MHz)	603	738	702	769

TABLE 3.VII
PERFORMANCE OF NEEDLE APPLICATOR WITHOUT AND WITH CSRRA, CSRRB AND CCRR METALENSES

Parameter	*Needle applicator*			
	no MTM	*CSRRa*	*CSRRb*	*CCRR*
Maximum SAR (W/kg) (averaged over the mass $m = 1\ g$, at $f = 2.45\ GHz$, and $P_{pk} = 20\ W$)				
Hepatic Tumour	2662	2748	2681	2755
Hepatic Tissue	1478	1669	1595	1589
Mean SAR (W/kg) (averaged over the mass $m = 1\ g$, at $f = 2.45\ GHz$, and $P_{pk} = 20\ W$)				
Hepatic Tumour	1575	1663	1595	1642
Hepatic Tissue	6.31	6.23	6.25	6.22
Total Power Loss (normalized to input power)				
Hepatic Tumour	0.390	0.402	0.395	0.405
Hepatic Tissue	0.554	0.544	0.547	0.544

3.4 Measurements

By the simulation results the choked single slot with sub-tip is chosen for the construction. A 14 G and a 16 G prototypes are fabricated and characterized.

3.4.1 14G Applicator

The Micro-Coax UT047C-ULL cable has been chosen for the 14G prototype fabrication. Its nominal diameter $d_{cable} = 1.19\ mm$ allows to fit it in the hypodermic tube of 14 gauge. Moreover, the low loss ultralow density PTFE (ULD PTFE) of the dielectric part permits a more thermal stability than solid PTFE, lowering of the power dissipations. This coax cable resists to an operating temperature until $T_{max} = 250\ °C$. The antenna was fabricated by stripping the cable shielding conductor to make the slot and soldering the internal conductor to the metallic tip. The applicator radiating part was embedded in a tube of PTFE.

Figure 3.25 shows the measurement of the scattering parameter modulus $|S_{11}|$ by using the vector network analyser Field Fox Keysight Technologies.

The modulus of the measured scattering parameter S_{11} as a function of the frequency f for various biological load conditions is shown in Figure 3.26:

i) with a biological load located from the tip till the radiating slot (dashed curve),
ii) with a biological load located on overall the radiating part till the shaft (solid curve),
iii) by immersing the prototype in a water filled vessel (dotted curve).

In particular, the biological load was obtained by keeping the applicator between hand fingers, with the aim of a preliminary characterization close to the *in-vivo* condition. The case ii) is shown in Figure 3.25. The impedance matching is good, also changing load conditions. In the best load condition, the modulus of the scattering parameter measured at the operating frequency $f = 2.45\ GHz$ was $|S_{11}| \cong -40\ dB$.

The applicator is put into a bovine liver and fed by a MW source with an average power $P_{avg} = 10\ W$ for 180 seconds, to carry out the *ex-vivo* validation. The obtained thermal lesion, identified by the tissue discolouration caused by the elevated temperature, is shown in Figure 3.27. The decolorated area has longitudinal length of $b = 32\ mm$, diameter of $a = 19\ mm$, and axial ratio $AR = 0.59$, in good agreement with simulations. The MW applicator designed provides good results. Ablation zone with well-defined contours into the biological tissue can be achieved by controlling the temperature increase. The surrounding healthy tissues are not damaged by the ablation session, confirming that this method preserves mini-invasive and patient wellness-oriented characteristics.

Figure 3.25 Experimental measurement of the scattering parameter modulus $|S_{11}|$ of 14G MW applicator prototype [5].

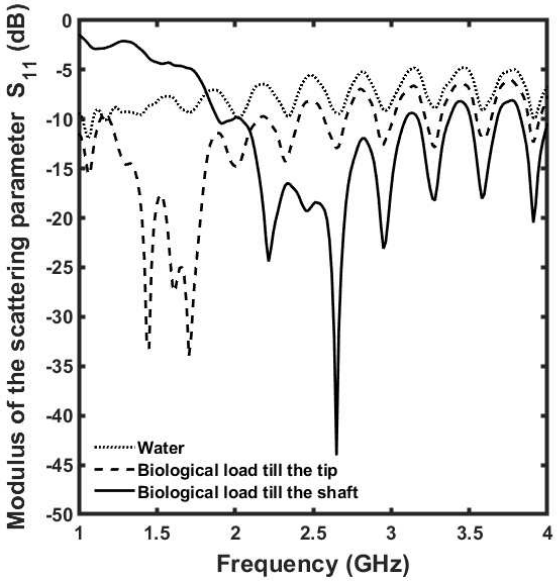

Figure 3.26 Characterization of the 14G MW applicator prototype, Figure 3.2b. Measured modulus of the scattering parameter S_{11} as a function of frequency f for different biological load [2].

Figure 3.27 Thermal lesion in bovine liver obtained during the experimental *ex-vivo* validation produced using a power supply of $P_{avg} = 10\ W$ for $t = 180\ s$. 14G MW applicator prototype [2].

3.4.2 16G Applicator

The Micro-Coax UT-031-LL cable has been chosen for the 16G prototype fabrication. Its nominal diameter $d_{cable} = 0.787\ mm$ allows to fit it in the hypodermic tube of 16 gauge.

The modulus of scattering parameter S_{11}, measured under different biological load conditions is obtained by using the vector network analyser Field Fox Keysight Technologies. Figure 3.28 shows the 16 G needle microwave

applicator prototype connected to the VNA for characterization. Figure 3.29 shows the scattering parameter modulus $|S_{11}|$ as a function of the frequency f measured with the 16 G applicator prototype for different biological load conditions.

Figure 3.30 shows the experiment pertaining to a thermal lesion of bovine *ex-vivo* liver, produced with the 16G prototype by using a power supply of $P = 20\ W$ for $t = 600\ s$. The thermal lesion (tissue discolored zone in Figure 3.30) of $34\ mm \times 40\ mm$ axial sizes is measured, in good agreement with simulation result of Figure 3.21

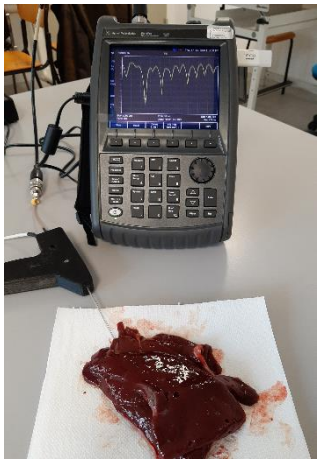

Figure 3.28 Experimental measurement of the scattering parameter modulus $|S_{11}|$ of 16G MW applicator prototype [4].

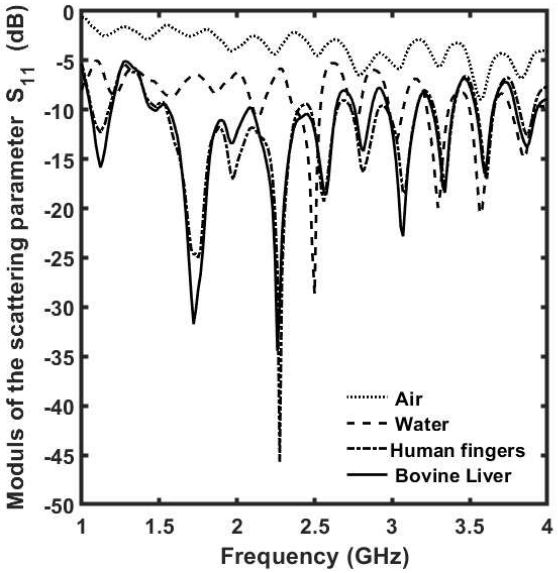

Figure 3.29 Characterization of the 16G MW applicator prototype, Figure 3.20. Measured modulus of the scattering parameter S_{11} as a function of frequency f for different biological load.

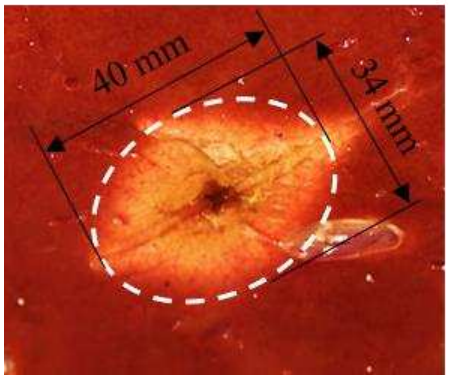

Figure 3.30 Thermal lesion in bovine liver obtained during the experimental *ex-vivo* validation produced using a power supply of $P_{avg} = 20\ W$ for $t = 600\ s$. 16G MW applicator prototype [3].

3.5 Concluding remarks

An extensive analysis of various design solutions has been performed in order to the fabrication of low-cost MW needle applicators for hyperthermia tumour therapy. Electromagnetic and thermal simulations are performed; the thermal lesion shape dimensions are evaluated as a function of the ablation duration time and for several values of the input power. Two prototypes of 14 gauge and 16 gauge have been designed, fabricated, and characterized. The experimental results are in good agreements with simulations. Their employment can be considered as a desirable alternative to surgical resection, reducing side effects to healthy tissues and increasing patient wellness, as mini-invasive approach. The 14G applicator having relatively larger size is simpler to be constructed and allow a cost reduction during its mechanical assembling. The simplified geometry allows a cost reduction also in the case of the most compact 16G version. In addition, various metamaterial lenses based on Closed Loop Resonator are designed and optimized to improve the performance of the 16G MW applicator. The numerical results are an interesting preliminary study and show great potential for subsequent developments and improvement of the MW needle applicator.

Further point of investigation to be developed in the future consists in the design of an optical fiber temperature sensor to be integrated with the MW applicator for an accurate thermal monitoring of the ablation session in real-time, based, as example, on optical fiber sensor [132]. Further than improvements can be achieved employing a double source system, e.g., by including a fiber laser source in the medium infrared (Mid-IR) wavelength range, where the biological tissues exhibit strong absorption [133-135].

4 Design of metamaterial lenses for the improvement of ultra-wide band planar antennas

4.1 Introduction

In recent years, a raising demand of environmental and medical applications has focused the academic research on ultra-wide band planar antennas for microwave imaging, tumour detection and ground penetrating radar [66,77-75]. These antennas offer a variety of advantages, not only in term of broadband but also for the consistent radiation output, reduced sidelobe level, low cost, and light weight. However, obtaining a printed antenna with both a high gain and broadband end-fire capabilities proves to be a challenging task. In the literature, various interesting approaches are introduced to enhance the radiation performance of these antennas [54-65].

In the following, the design and optimization of metalenses to improve the radiation performance of an antipodal Vivaldi antenna, operating in the $f_{AVA} = 3 \div 13.5\ GHz$ band, are reported. The preliminary design of the metalens has been performed with the S-Parameter Retrieval (SPR) method [117-118], and the optimization of the antenna with the metalens has been performed with full-wave numerical simulations. Some prototypes have been fabricated with the PCB process. The characterization of the fabricated prototypes shows good agreement with the simulation.

4.2 Design overview

The metalenses are designed to improve a pristine AVA, consisting of two symmetrical, exponentially tapered patch flares printed on the opposite sides of the dielectric substrate. The equations reported in [70] has been used for the design of the exponentially tapered flares. The metalens modelling has been

performed by means of the SPR method, based on the assumption of layer homogenization. The design has involved the following steps:

i) the S-parameters of the metalens have been numerically simulated with the commercial EM simulation software, CST Studio Suite®

ii) the complex impedance Z_{eff}, the complex refractive index N_{eff}, the effective electric permittivity ε_{eff}, and the effective magnetic permeability μ_{eff} have been calculated from the simulated S-parameters, using the inversion algorithm based on the Kramers–Kronig relationship [117-118]. The retrieved effective parameters have been used for the preliminary design.

iii) The metalens integrated into the antenna substrate has been optimized in the full-wave simulations [118] to take into account coupling effects between the metalens and the antenna.

4.2.1 Antenna design

The AVA is schematically illustrated in Figure 4.1. It is an exponentially tapered three-flare patch antenna operating in the frequency range $f_{AVA} = 3 \div 13.5\ GHz$. The shapes of the flare edges allow an enhancement in compactness [68]. In the design, the antenna optimization has been performed by numerical simulations by varying i) the flares widths w_1, w_2, w_3, and ii) the distances between the flares d_1, d_2.

The resulting geometrical parameters for the optimized antenna, allowing the gain maximization to parity of bandwidth, are listed in Table 4.I.

The Rogers RO4350B laminate, with a dielectric permittivity of $\varepsilon_r = 3.66$ and a loss tangent of $tan\delta = 0.0037$, having a commercial thickness of $t = 0.762\ mm$ and standard copper cladding with a thickness of $t_c = 0.035\ mm$, has been chosen.

Figure 4.2 shows the modulus of the scattering parameter S_{11} and the gain G as a function of the frequency f of the AVA simulated with the parameters of Table 4.I. The simulated frequency $-10\ dB$ bandwidth is about $BW = 10.5\ GHz$, over the frequency range $f_{AVA} = 3 \div 13.5\ GHz$, the gain is close to $G = 10\ dB$ for frequencies higher than $f > 7.5\ GHz$, and the maximum gain is about $G_{max} = 10.3\ dB$ at the frequency $f = 8\ GHz$.

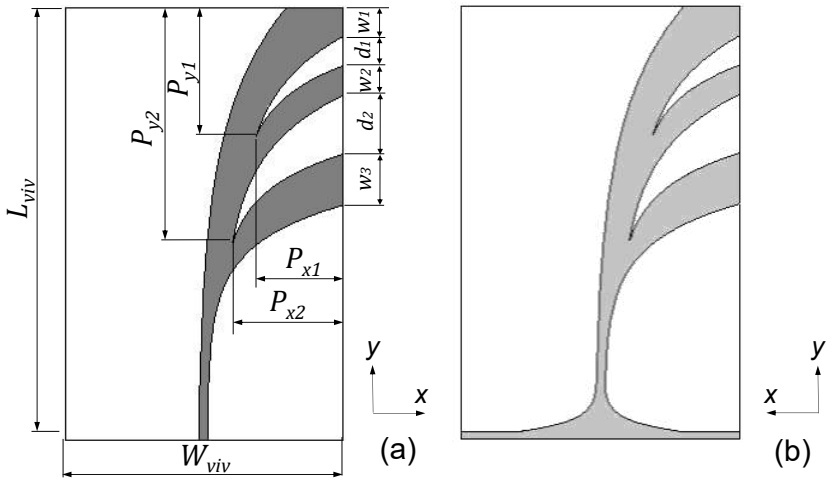

Figure 4.1 Scheme of the AVA: (a) Top view, and (b) Bottom view [7].

TABLE 4.I

GEOMETRIC PARAMETERS OF AVA

Parameter	*Value (mm)*	*Description*
L_{viv}	73.7	Antenna length
W_{viv}	48	Antenna width
P_{x1}	15	x-position of the inner point of the first tapered slot
P_{y1}	22	y-position of the inner point of the first tapered slot
P_{x2}	19	x-position of the inner point of the second tapered slot
P_{y2}	58.4	y-position of the inner point of the second tapered slot
w_1	5	First flare width
w_2	5	Second flare width
w_3	8.7	Third flare width
d_1	5	Distance between the first and the second flares
d_2	10	Distance between the second and the third flares

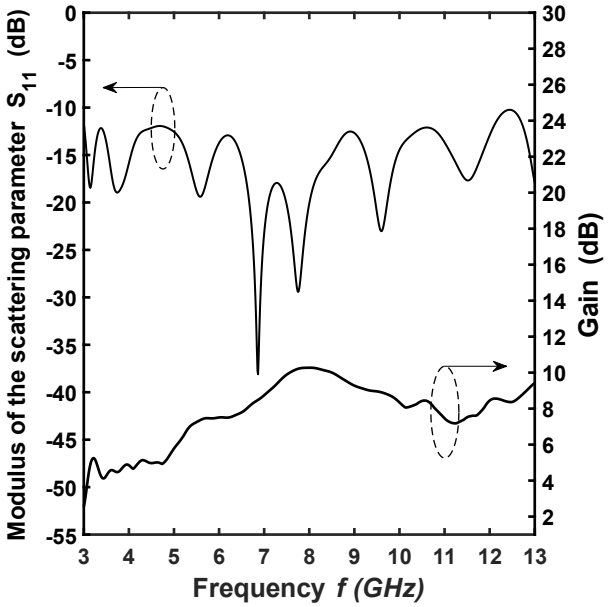

Figure 4.2 Simulated modulus of the scattering parameter S_{11} and realized gain G as a function of the frequency f of the AVA [7].

4.2.2 Metamaterial lens design

In order to improve the radiation characteristics of the AVA, in terms of gain and directivity, without significantly affecting the bandwidth, some metalenses are designed. First of all, a metalens based on a geometry well-known in literature, the Split Ring Resonator (SRR), and then a metalens based on a novel L-shaped geometry, that allows a design with a high degree of freedom, have been investigated.

4.2.2.1 Metalens based on Split Ring Resonator

The geometry of the unit cell consists of a modified version of the well-known Split Ring Resonator (SRR), as shown in Figure 4.3a. Its equivalent resonant circuit is shown in Figure 4.3b. When electromagnetic radiation propagates through the metalens, currents, and local charges are induced on the metal rings. Capacitive effects C_{split} occur at the non-parallel capacitive gap. A metal dot, placed in the center of the circular ring, induces the capacitive coupling effect C_{coup} with the ring, increasing the metalens global effective capacitance. Self-inductance effects L_{ring} occur along the circular ring. The metal inclusions are placed on both sides of the substrate, so strong mutual coupling effects occur between the top and bottom layer of the unit cell.

The unit cell geometry has been optimized by numerical simulations when arranged in planar arrays integrated on the AVA substrate. The SRR unit cell scheme, with the geometric parameters considered for the modelling and the simulations, is shown in Figure 4.4. For the optimization, geometries with and without the central dot have been considered by varying: i) the ring radius r_c ; ii) the angular aperture of the split α; iii) the strip width w; and iv) the unit cell lattice lengths d_x, d_y, d_z. The optimized geometric parameters of the SRR unit cell are listed in Table 4.II.

To investigate the transmission properties of the designed metalens, numerical analysis has been performed by following two different approaches.

i) In the first step, a single unit cell under appropriate boundary conditions, as shown in Figure 4.5 has been considered. Starting from the simulated S-parameters of the structure of Figure 4.4, with the values listed in Table 4.II, the metalens effective parameters have been calculated using the S-Parameter Retrieval method [117-118]. The simulated modulus of the S-parameters of SRR unit cell as a function of the frequency f is shown in the Figure 4.6a. The retrieved effective parameters as a function of the frequency f: complex refractive index N_{eff}, effective electric permittivity ε_{eff}, and effective magnetic permeability μ_{eff} are shown in Figure 4.6b, Figure 4.6c, and Figure 4.6d respectively. The modulus of the scattering parameter S_{11} is smaller than $-4\ dB$ for frequencies below $f < 13\ GHz$, as shown in Figure 4.6a. The complex effective refractive index $N_{eff} = n_{eff} + jk_{eff}$ of Figure 4.6b shows a constant non-resonant value in the whole bandwidth. These results, even if approximated, give valuable information regarding a non-resonant and promising good behaviour for all the considered metalenses over the bandwidth of interest [57,59].

ii) In a second step, all the different metalenses, constituted by the actual number of cells have been investigated too, with and without the AVA, confirming the feasibility of the chosen geometry.

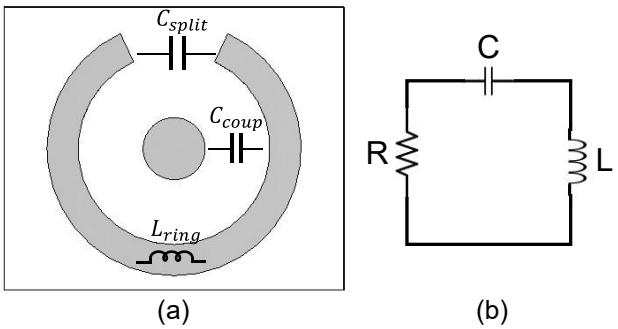

Figure 4.3 (a) Scheme of the designed SRR unit cell and (b) its equivalent circuit [7].

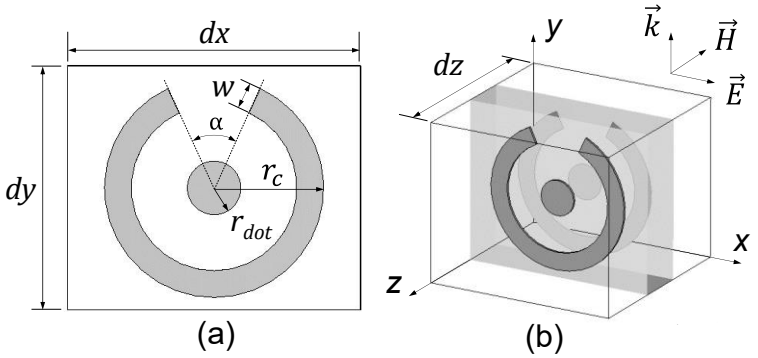

Figure 4.4 Scheme of the SRR unit cell: (a) Top and bottom view, and (b) 3D view [7].

TABLE 4.II

GEOMETRICAL PARAMETERS OF THE SRR UNIT CELL

Parameter	*Value*	*Description*
d_x	3 mm	Unit cell lattice length along x −axis
d_y	2.5 mm	Unit cell lattice length along y −axis
d_z	3 mm	Unit cell lattice length along z −axis
r_c	1.125 mm	Ring radius
r_{dot}	0.275 mm	Dot radius
α	50°	Angular aperture of the split
w	0.275 mm	Strip width

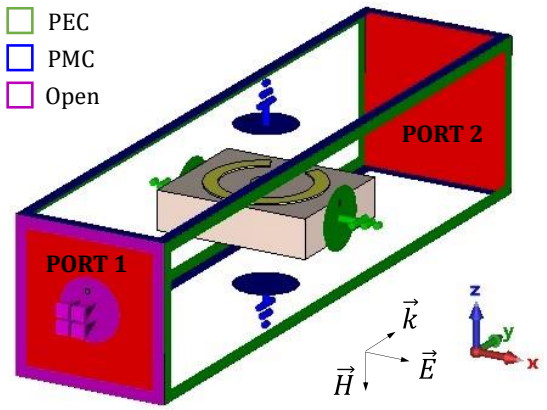

Figure 4.5 Simulation model and the boundary conditions for the effective parameters retrieval [7].

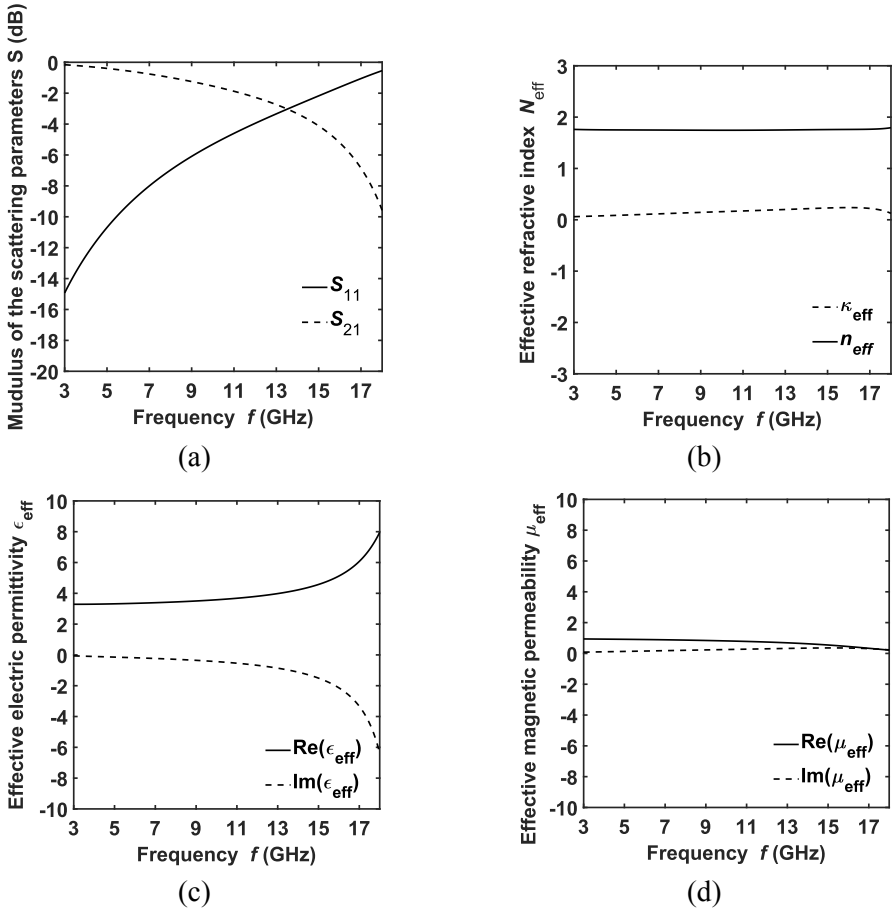

Figure 4.6 (a) The simulated S-parameters and the retrieved effective parameters as a function of the frequency f: (b) complex refractive index N_{eff}, (c) effective electric permittivity ε_{eff}, and (d) effective magnetic permeability μ_{eff} of SRR unit cell [7].

4.2.2.2 Novel L-Shaped Metalens

For the preliminary design, in the first step, an equivalent homogeneous layer (EHL) has been considered in place of the metalens, with the aim of finding the optimized values of the effective parameters ε_{eff} and μ_{eff} to increase the gain and maintain the bandwidth. As a second step, the design of the metalens unit cell is performed in order to obtain values of the effective parameters ε_{eff} and μ_{eff} as close as possible to the optimized ones. This condition is verified via SPR method [117-118]. Finally, in the third step, the full simulation of the antenna and metamaterial is performed for the actual design refinement before the antenna fabrication. The EHL is shown in Figure 4.7 as a green layer.

Figure 4.8 shows the full-wave simulation of the gain G as a function of the frequency of the AVA (solid curve) and the AVA with EHL having a thickness of $d_{EHL} = 0.832\ mm$ for the best values of effective permittivity ε_{eff} and effective permeability μ_{eff} (dashed curve). The thickness of $d_{EHL} = 0.832\ mm$ corresponds to the sum of the substrate and the double metal strips thicknesses, $d_{EHL} = t + 2 \times t_c$. A metalens having an effective permittivity of $\varepsilon_{eff\,MG} = 5.75$ and an effective permeability of $\mu_{eff\,MG} = 1.5$ could allow a maximum gain (MG) improvement of about $\Delta G = 4\ dB$.

A metalens based on the novel L-shaped unit cell has been optimized. Figure 4.9a shows the investigated unit cell. The geometry consists of an arrangement of L-shaped metal elements printed on both sides of the antenna substrate. In the proposed unit cell structure, it is possible to recognize an external square ring with four splits and two internal stubs. Different inductive and capacitive effects are induced depending on the electric field orientation of the traveling wave with respect to the metalens plane. Considering the electric field (E-field) polarized along the x-axis, inductive effects along the metal strips and capacitive effects at the gaps occur, as shown in Figure 4.9a. The equivalent inductors, namely L, represent the self-inductance produced by the metal L-shaped elements. The equivalent capacitances originate from the electric charges accumulated via the splits, namely C_1, and by the coupled charges between the adjacent metal L-shaped elements, namely C_2, C_3, and C_4 [140]. The equivalent circuit of the L-shaped unit cell is depicted in Figure 4.9b; its effective complex impedance Z_{eff} can be fine-tuned by varying the geometries of the conductive metal inclusions, the gap width between them, and the dielectric permittivity of the substrate [112,141].

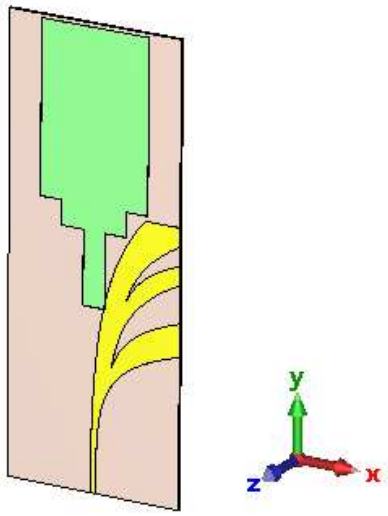

Figure 4.7 Schematic of AVA with EHL (green region) in place of the metalens [6].

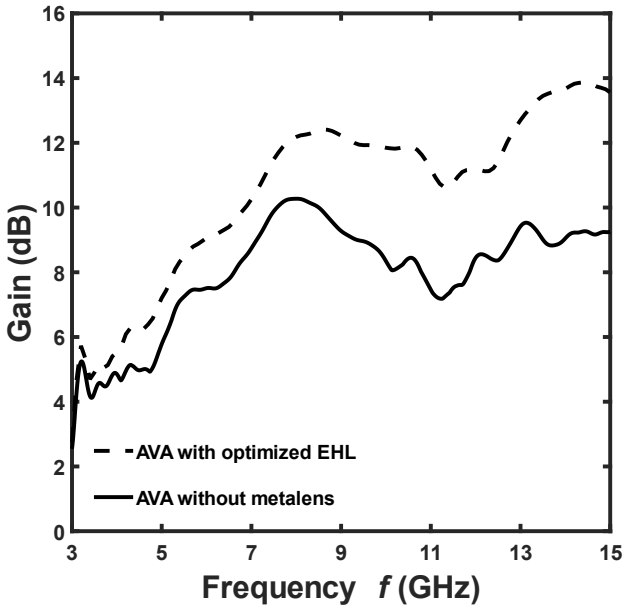

Figure 4.8 Full-wave simulation of the gain G as a function of frequency for AVA (solid curve) and AVA with EHL having a thickness of $d_{EHL} = 0.832\ mm$ for the optimized effective permittivity $\varepsilon_{eff\ MG}$ and effective permeability $\mu_{eff\ MG}$ (dashed curve) [6].

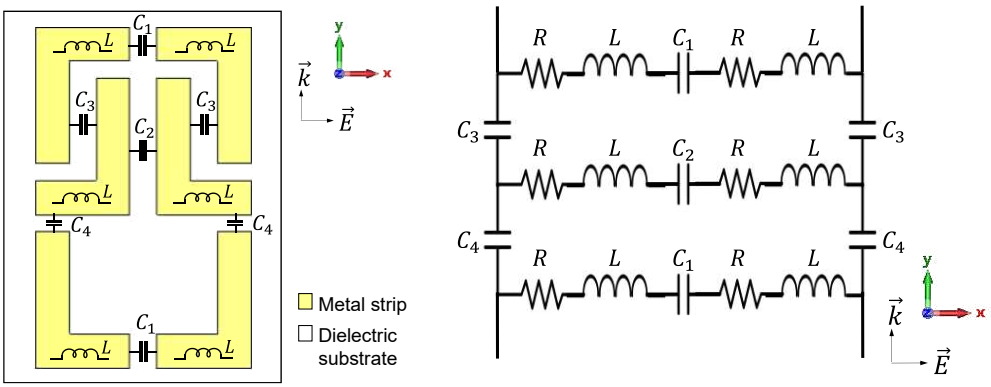

(a) (b)

Figure 4.9 (a) Schematic of the designed L-shaped unit cell and (b) its equivalent circuit [6].

For the SPR method, the S-parameters simulations of the stand-alone unit cell, i.e., before its integration with AVA geometry, are performed by considering the same substrate of the antenna. The top and the 3D views of the L-shaped unit cell with the relative geometric parameters are shown in Figure 4.10a and Figure 4.10b, respectively.

In the second design step, in order to retrieve the effective parameters of the metalens, the unit cell illustrated in Figure 4.11 has been considered. In the simulation, the $\vec{E}\,\vec{k}$-plane of the unit cell corresponds to the Vivaldi xy-plane; see Figure 4.1 and Figure 4.11. The plane EM wave excitation is obtained (see Figure 4.11) via the Waveguide Port 1, with open boundary conditions applied in the propagation direction. The perfect electric conductor (PEC) and the perfect magnetic conductor (PMC) boundary conditions are suitably applied.

The L-shaped unit cell geometry has been optimized in order to obtain a broadband gain enhancement to parity of the bandwidth [57-58]. The geometry of the proposed unit cell offers a high degree of freedom for metalens optimization. The inductive effects can be tuned in different ways, depending on the EM polarization, by varying the length of the L-element independently along the x-direction, L_x, and y-direction, L_y. Similarly, the capacitive effects can be tuned by varying the gap widths of the splits g_x and g_y. Moreover, changing the metal strip width w affects both the capacitive and inductive effects. Therefore, the L-shaped unit cell resonant behavior has been evaluated by changing all the above-mentioned geometrical parameters and the lattice lengths d_x and d_y.

Table 4.III reports the optimized values obtained in the third design step of the unit cell of the metalens integrated into the antenna. To identify these

parameters, the exact number and distribution of cells, described in the following Paragraph 4.2.3, have been considered.

To give an insight into the metalens behavior, the simulated amplitudes and phases of the S_{11} and S_{12} parameters of the L-shaped unit cell versus the frequency are shown in Figure 4.12 for the optimized parameters of Table 4.III.

The average values of the real part of the effective electric permittivity $Re(\varepsilon_{eff,av}) = 4.98$ and of the effective magnetic permeability $Re(\mu_{eff,av}) = 0.75$, retrieved with SPR method from the aforesaid S_{11} and S_{12} curves, are close enough to the theoretical optimized values $\varepsilon_{eff\,MG} = 5.75$ and $\mu_{eff\,MG} = 1.5$ identified in the first design step and provide an almost constant value of the effective refractive index over the whole frequency range. It is reported in Figure 4.12c.

A congruent number of unit cells allows better results, taking into account the couplings between adjacent unit cells [142]. Therefore, a single cell, 3×3, and 6×6 clusters of unit cells have been also investigated, obtaining practically the same results. As a consequence, the frequency range $f = 3 \div 15\ GHz$ can be considered a potential operation region for the antenna. This means that the L-shaped metalens can improve the antenna radiation performance in the whole band [57-58].

Indeed, the designed lens has a higher average refractive index than that of the antenna substrate, so a waveguiding effect is possible. The EM field is better confined via the lens, enhancing the radiation beam in the end-fire direction. In addition, the high refractive index region obtained with the metalens can be used to change the EM wavefronts from spherical to approximately planar ones, resulting in a more confined radiation pattern and higher directivity. This is explained by considering that the phase velocity of the wavefront in the central region is smaller than that of the wavefront edges due to the higher refractive index metalens.

The approximated equivalent circuit reported in Figure 4.9b models the proposed unit cell behavior. By exploiting the Advanced Design System (ADS) [142] and making use of the tuning module, the following set of values, $L = 0.22\ nH$, $C_1 = 1.6\ pF$, $C_2 = 0.3\ pF$, $C_3 = 1.2\ pF$, $C_4 = 0.55\ pF$, and $R = 2.625\ \Omega$, have been identified, leading to a modulus of the scattering parameter $|S_{11}|$ in good agreement with that of Figure 4.12a.

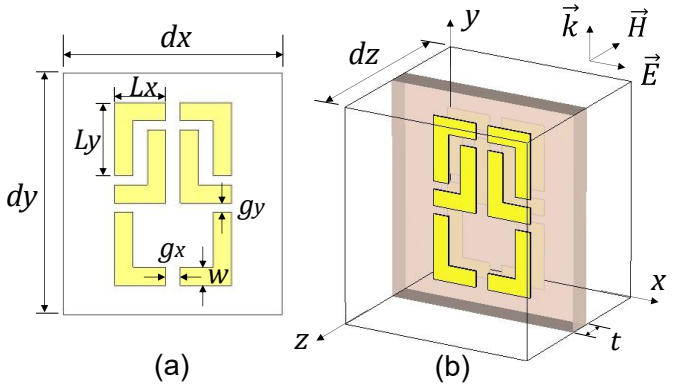

Figure 4.10 Schematic of L-shaped unit cell: (a) top view, and (b) 3D view [6].

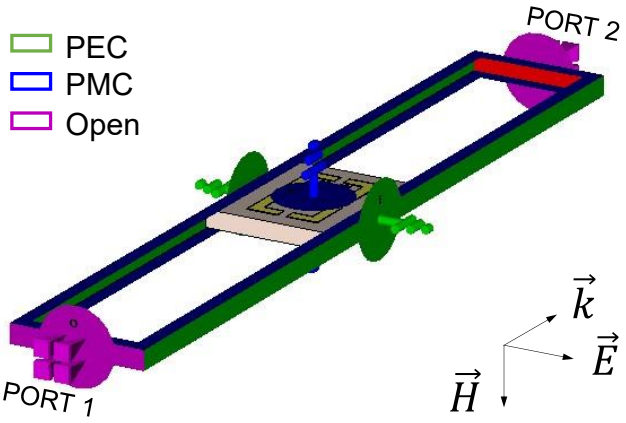

Figure 4.11 Schematic of the simulation model for the second design step of the L-shaped unit cell [6].

TABLE 4.III

GEOMETRICAL PARAMETERS OF THE L-SHAPED UNIT CELL

Parameter	*Value (mm)*	*Description*
L_x	1.40	L-element length along x-axis
L_y	2.00	L-element length along y-axis
w	0.50	Metal strip width
g_x	0.40	Distance between two adjacent metal elements along x-axis
g_y	0.25	Distance between two adjacent metal elements along y-axis
dx	6.00	Lattice length along x-axis
dy	6.60	Lattice length along y-axis
dz	≥ 0.832	Transversal thickness considered for scattering parameters evaluation to be used in the SPR method
t	0.762	Substrate thickness
t_c	0.035	Metal strip thickness

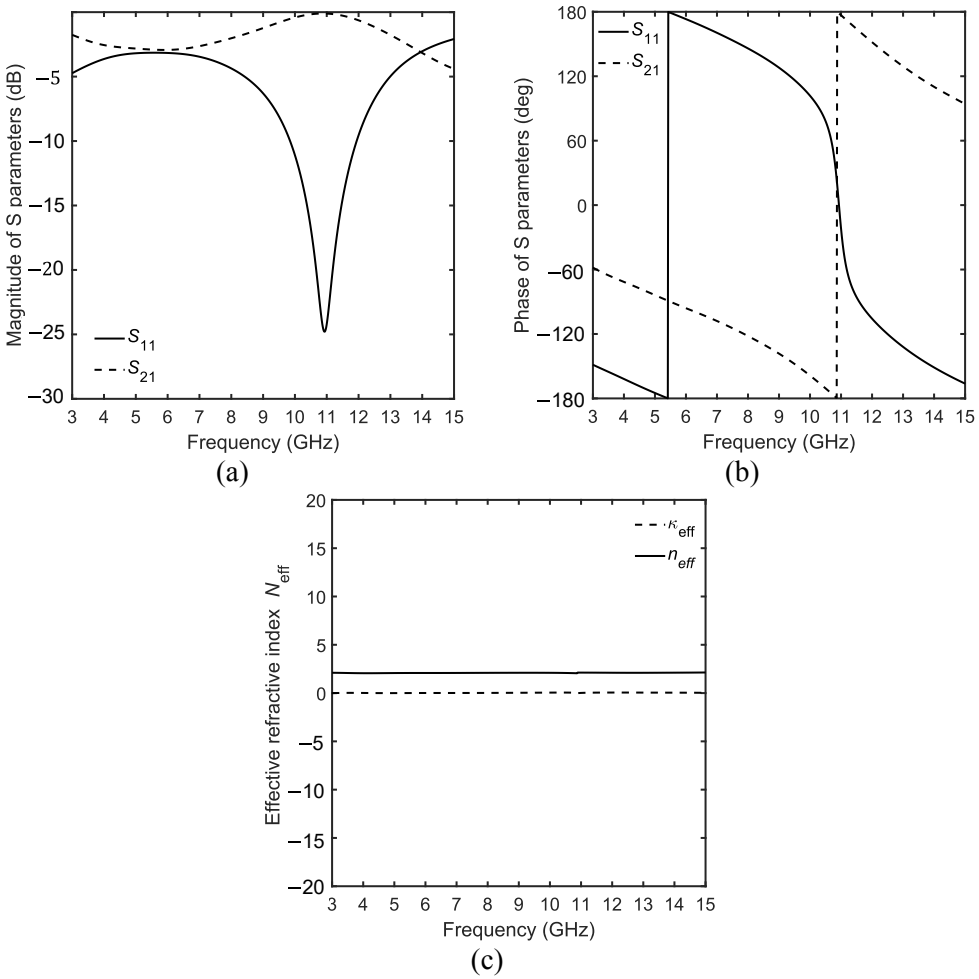

Figure 4.12 (a) Magnitude and (b) phase of the simulated S-parameters and retrieved effective parameters of L-shaped unit cell as a function of frequency. (c) Refractive index N_{eff} [6].

4.2.3 Antenna with metamaterial lens design

In the last design step, the metalens has been integrated into the substrate of the antenna and placed close to the tapered slot in the end-fire direction for the optimization by numerical full-wave simulations in the frequency band $f = 3 \div 15\ GHz$, in order to refine the results, by improving the realized gain of the antenna without reducing its bandwidth.

The optimized values, reported in Table 4.II for metalens based on SRR and in Table 4.III for L-Shaped metalens, have been found via full-wave simulations with a trial-and-error approach. Then, further optimization of the antenna with metalens has been performed by varying, in the full-wave simulation, the

number and distribution of the unit cells and the distance along the y-direction between the metalens and antenna. Several configurations have been simulated and compared.

4.2.4 Validation of the approach with the SPR method

In order to validate the chosen approach [117-118], the three following cases, for which the effective volumetric material properties have been retrieved and used for the modelling of the L-shaped metalens, are investigated:

(a) $d_{eff} = 3 \times dy;\ dz = 6\ mm$

(b) $d_{eff} = 3 \times dy;\ dz = 1\ mm$

(c) $d_{eff} = 3 \times dy;\ dz = 0.832\ mm$

where dy is the cell length along y-axis, d_{eff} is the effective thickness along propagation direction used in the retrieval algorithm [118], dz is the transversal thickness considered for scattering parameters evaluation to be used in the retrieval method. The dimensions of the L-shaped unit cell are as given in Table 4.III.

Figure 4.13 shows the schematic of the simulation model for the 3×3 unit cell numerical characterization. The plane EM wave propagation is obtained via excitation of the port 1 with the suitable boundary conditions (PEC, PMC, OPEN). The ε_{eff}, μ_{eff} values are retrieved exploiting the scattering parameters of the two-port network of Figure 4.13. It is worth noting that dz is the height of the ports 1 and 2, see Figure 4.10b and Figure 4.13. This explains the ε_{eff}, μ_{eff} dependence on dz. By increasing dz the scattering parameters are simulated with increased air region thickness and PML conditions.

The retrieved parameters, by considering the 3×3 unit cell case, are:

i) $\varepsilon_{eff} = 1.62$, μ_{eff}=0.94 for case (a) i.e., thickness $dz = 6\ mm$;

ii) $\varepsilon_{eff} = 4.76$, μ_{eff}=0.78 for case (b) i.e., thickness $dz = 1\ mm$;

iii) $\varepsilon_{eff} = 4.98$, μ_{eff}=0.75 for case (c) i.e., thickness $dz = 0.832\ mm$.

The full-wave simulations of AVA with EHL, having as electromagnetic parameters the average retrieved ε_{eff} and μ_{eff}, and the specified thicknesses $d_{EHL} = dz$ used in the retrieval method, have been performed and compared with the full-wave simulation of AVA with L-shaped metalens.

Figure 4.14 shows the schematic of AVA with EHL (green region) introduced in place of metalens for the three cases. The dimensions, in the x-direction and y-direction of the EHL, are the same for the L-shaped metalens.

Figure 4.15 illustrates full-wave simulated gain G as a function of frequency f of the AVA with L-shaped metalens (black curves), AVA with EHL having thickness $dz = 6\ mm$, $\varepsilon_{eff} = 1.62$, $\mu_{eff} = 0.94$ (blue curve), AVA with EHL having thickness $dz = 1\ mm$, $\varepsilon_{eff} = 4.76$, $\mu_{eff} = 0.78$ (green curve), and AVA with EHL having thickness $dz = 0.832\ mm$, $\varepsilon_{eff} = 4.98$, $\mu_{eff} = 0.75$ (red curve). A very good agreement is evident, confirming the validity of the followed approach.

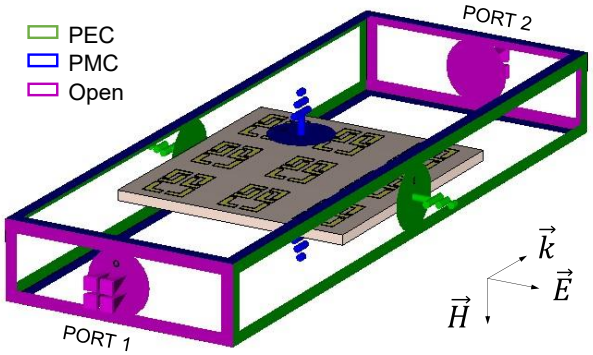

Figure 4.13 Schematic of the simulation model for the 3 × 3 unit cell numerical characterization.

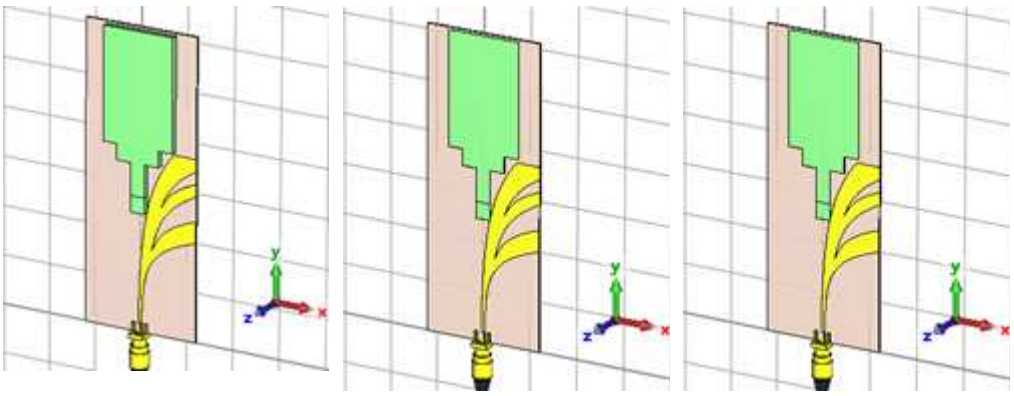

(a) (b) (c)

Figure 4.14 Schematic of AVA with EHL (green region) introduced in place of metalens
(a) $dz = 6\ mm$, $\varepsilon_{eff} = 1.62$, $\mu_{eff} = 0.94$
(b) $dz = 1\ mm$, $\varepsilon_{eff} = 4.76$, $\mu_{eff} = 0.78$
(c) $dz = 0.832\ mm$, $\varepsilon_{eff} = 4.98$, $\mu_{eff} = 0.75$

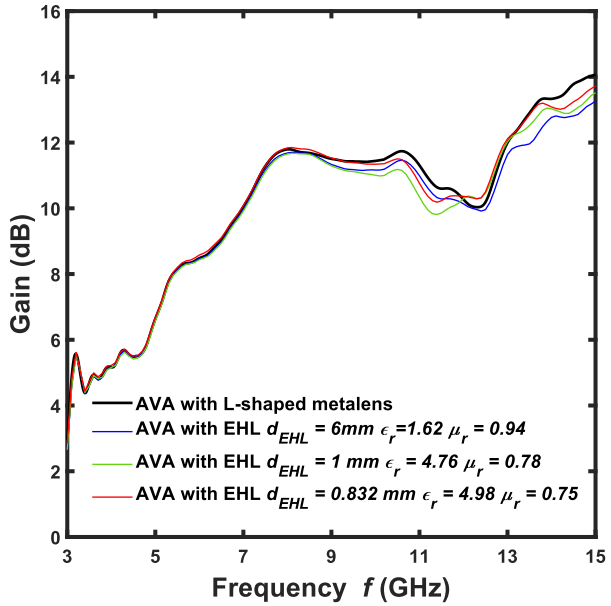

Figure 4.15 Full-wave simulated gain G as a function of frequency f of the AVA with L-shaped metalens (black curves), AVA with EHL having thickness $dz = 6\,mm$, $\varepsilon_{eff} = 1.62$, $\mu_{eff} = 0.94$ (blue curve), AVA with EHL having thickness $dz = 1\,mm$, $\varepsilon_{eff} = 4.76$, $\mu_{eff} = 0.78$ (green curve), and AVA with EHL having thickness $dz = 0.832\,mm$, $\varepsilon_{eff} = 4.98$, $\mu_{eff} = 0.75$ (red curve).

4.3 Simulation results

4.3.1 Antenna with metalens based on SRR (AVA SRR)

Different configurations of metalenses have been considered. Three of the most interesting and optimized antennas are shown in Figure 4.16. The antenna with a triangular metalens, labelled as AVA SRR#1, is shown in Figure 4.16a. The metalens, placed between the flares of the antenna in the end-fire direction, consists of a triangular array of fifteen SRR unit cells.

The second antenna, labelled as AVA SRR#2 in Figure 4.16b, has been obtained from AVA SRR#1 by introducing a rectangular metalens at a distance h_1 from the triangular one, with an air gap between them. The rectangular metalens consists of sixty elements arranged in a $N \times M = 4 \times 15$ array.

For the metalenses of the third antenna, labeled as AVA SRR#3 in Figure 4.16c, variable unit cells size has been exploited to have a good behavior for different frequencies.

In the design, the optimization of the AVA with these three different SRR metalenses has been performed in the frequency range $f = 3 \div 13\ GHz$, varying:

i) the metalens position,
ii) the number of unit cells for both triangular and rectangular array,
iii) the distance between triangular and rectangular metalens h_1,
iv) the scaling factor k of the unit cells in the case of alternate rows, i.e., for AVA SRR#3.

The optimized geometric parameters of the AVA SRR antennas are listed in Table 4.IV. An optimized scaling factor of $k = 1.125$ has been identified, after several simulations, to scale up the unit cells of the alternate rows for both triangular and rectangular metalenses of AVA SRR#3.

Figure 4.17 depicts the simulated modulus of the scattering parameter S_{11} as a function of the frequency f. The optimized AVA SRR#1 (dashed curve) maintains the wideband pristine behavior of AVA. For the optimized AVA SRR#2 (dash-dotted curve) and AVA SRR#3 (dotted curve), the introduction of rectangular metalens in addition to the triangular one, slightly reduces the $-10\ dB$ bandwidth at high frequencies.

Figure 4.18 shows the simulated gain G (black curves) and gain increase ΔG (red curves) as a function of frequency f. For AVA SRR#1 a maximum gain of $G_{max} = 10.8\ dB$ and a maximum gain increase of $\Delta G_{max} = 1.7\ dB$ at the frequency $f = 12.9\ GHz$ have been simulated. Better gain performances are obtained over the whole bandwidth for AVA SRR#2, with a maximum gain $G_{max} = 11.2\ dB$ at $f = 8.1\ GHz$ and a maximum gain increase $\Delta G_{max} = 2\ dB$ at $f = 11.8\ GHz$. AVA SRR#3 exhibits the highest gain only below $f < 10.3\ GHz$ with a maximum value $G_{max} = 11.4\ dB$ at $f = 8.2\ GHz$ and a maximum gain increase of $\Delta G_{max} = 2.1\ dB$ at $f = 10.1\ GHz$.

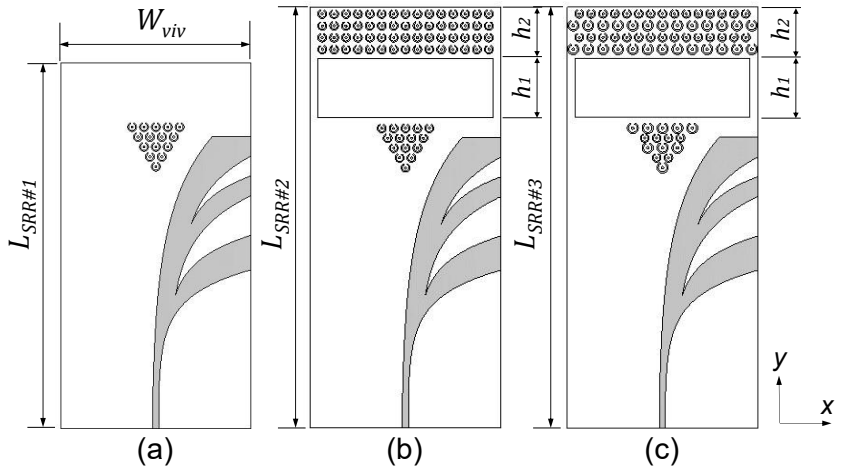

Figure 4.16 Scheme of the designed antenna with metalenses: (a) AVA SRR#1, (b) AVA SRR#2, and (c) AVA SRR#3 [7].

TABLE 4.IV

GEOMETRIC PARAMETERS OF THE AVA SRR ANTENNAS

Parameter	*Value (mm)*	*Description*
$L_{SRR\#1}$	92.15	AVA SRR#1 length
$L_{SRR\#2}$	106.7	AVA SRR#2 length
$L_{SRR\#3}$	106.7	AVA SRR#3 length
h_1	15	Distance between triangular and rectangular metalens
h_2	13	Rectangular metalens length

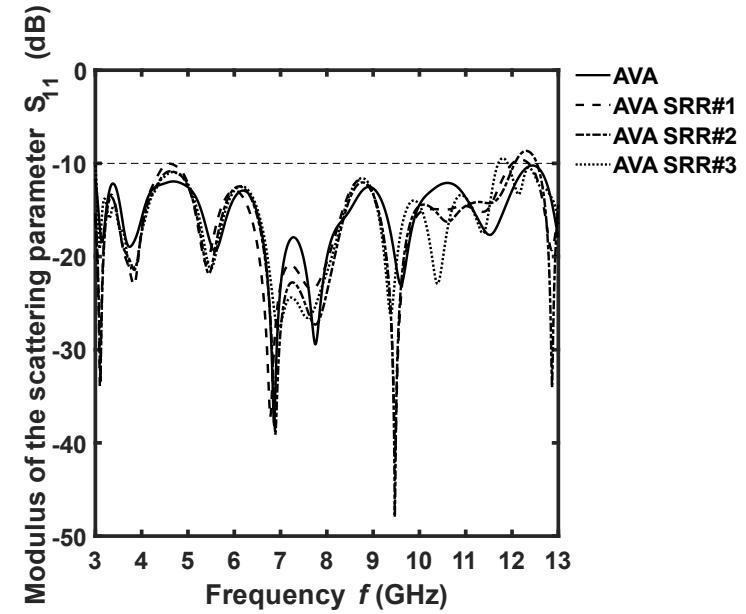

Figure 4.17 Simulated modulus of the scattering parameter S_{11} as a function of the frequency f, for the AVA without metalens (solid curve), the AVA SRR#1 (dashed curve), the AVA SRR#2 (dash-dotted curve), and the AVA SRR#3 (dotted curve) [7].

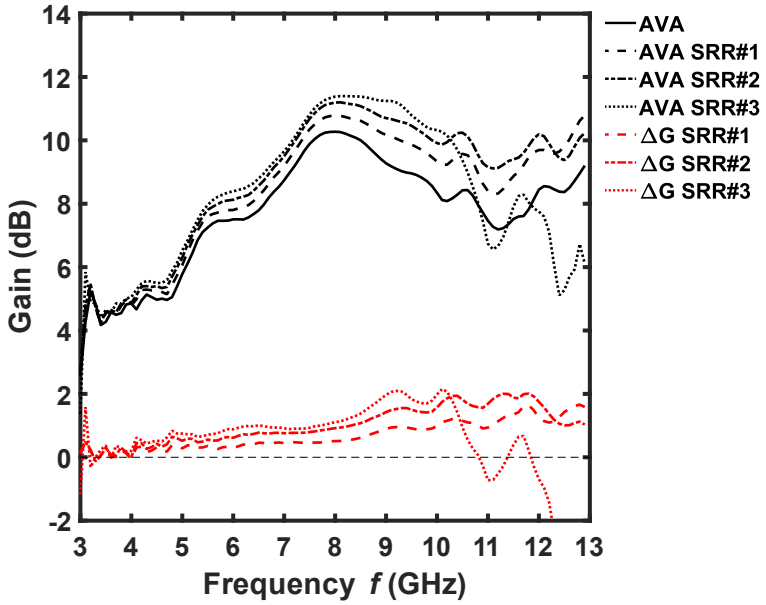

Figure 4.18 Simulated gain G (black curves) and gain increase ΔG (red curves) as a function of frequency f, for the AVA without metalens (solid curve), the AVA SRR#1 (dashed curve), the AVA SRR#2 (dash-dotted curve), and the AVA SRR#3 (dotted curve) [7].

4.3.2 Antenna with novel L-Shaped metalens (AVA L-shaped)

In Figure 4.19a, the metalens of the optimized AVA L-shaped#1 consists of an array of 41 L-shaped unit cells integrated on the antenna substrate, increasing the antenna length along the $y-$axis by $L_y = 47\ mm$. This antenna exhibited particularly promising performance over the whole band, in particular at high frequencies.

The AVA L-shaped#2, shown in Figure 4.19b, consists of an array of 67 L-shaped unit cells integrated into the antenna substrate; the larger metalens also requires a slight increase in the antenna substrate width along the $x-$axis. The AVA L-shaped#2 allows better performance at low frequencies.

In Figure 4.20, the modulus of the simulated scattering parameter $|S_{11}|$ as a function of frequency is illustrated for the AVA without a metalens (black curve) and the AVA L-shaped#1 (magenta curve) and AVA L-shaped#2 (green curve) metalenses. The bandwidth $f_{ava\ L\#1} = 3 \div 15\ GHz$ of AVA L-shaped#1 is increased with respect to $f_{AVA} = 3 \div 13.5\ GHz$ of the AVA without a metalens. The L-shaped#2 allows an improvement in impedance matching for frequencies of $f < 6.5\ GHz$ but reduces the $-10\ dB$ bandwidth to the range of $f_{ava\ L\#2} = 3 \div 11.8\ GHz$.

In Figure 4.21, the realized gain G (solid curves) of the three antennas and the gain increase ΔG (dashed curves) with respect to the gain without a metalens, simulated as a function of the frequency, are reported, with the same choice for the curve colors. For the AVA L-shaped#1, the gain increase can be observed over the whole frequency range, with an average value of about $\Delta G_{av} = 2\ dB$ and a maximum of $\Delta G_{max} = 4.8\ dB$ at a frequency of $f = 15\ GHz$. The maximum gain is $G_{max} = 14.1\ dB$ at a frequency of $f = 15\ GHz$. For the AVA L-shaped#2, a gain increase of about $\Delta G = 2\ dB$ is obtained for frequencies of $f < 6\ GHz$ and $f > 8\ GHz$. The simulated maximum gain is $G_{max} = 12.2\ dB$ at a frequency of $f = 15\ GHz$.

The L-shaped#1 metalens improves both the antenna bandwidth and the gain in the whole band, especially at higher frequencies. The AVA L-shaped#1 at higher frequencies irradiates a beam more confined than that of AVA L-shaped#2. The L-shaped#2 metalens allows a better gain improvement at the lower frequencies but reduces the bandwidth at higher frequencies.

The simulated E-field distributions in the xy-plane of the AVA without a metalens and AVA L-shaped#1 at a frequency of $f = 14\ GHz$ are shown in

Figure 4.22. As expected, the near-field of the antenna with a metalens exhibits wavefronts that are flatter than those of the AVA without a metalens, and the radiation in the end-fire direction is increased. Moreover, the L-shaped#1 metalens reduces the antenna back propagation. The simulated 3D view of the normalized radiation patterns, at a frequency of $f = 14\ GHz$ for the AVA and AVA L-shaped#1, are compared in Figure 4.23. The lens improves the antenna's directivity and reduces the half-power bandwidth (HPBW).

To verify the effects of the metalens on the antenna performances, the full-wave simulations of the gain G as a function of the frequency for AVA L-shaped#1 (solid curve) and AVA with EHL, having a thickness of $d_{EHL} = 0.832\ mm$ and values of permittivity $\varepsilon_r = 4.98$ and permeability $\mu_r = 0.75$ (dashed curve), are compared in Figure 4.24. The dimensions in the x-direction and y-direction of the EHL are the same for the metalens L-shaped#1, and the thickness d_{EHL} corresponds to the sum of the substrate and double metal strips thicknesses. A particularly good agreement is evident.

To conclude, the L-shaped#1 metalens is chosen as an interesting solution for prototype fabrication.

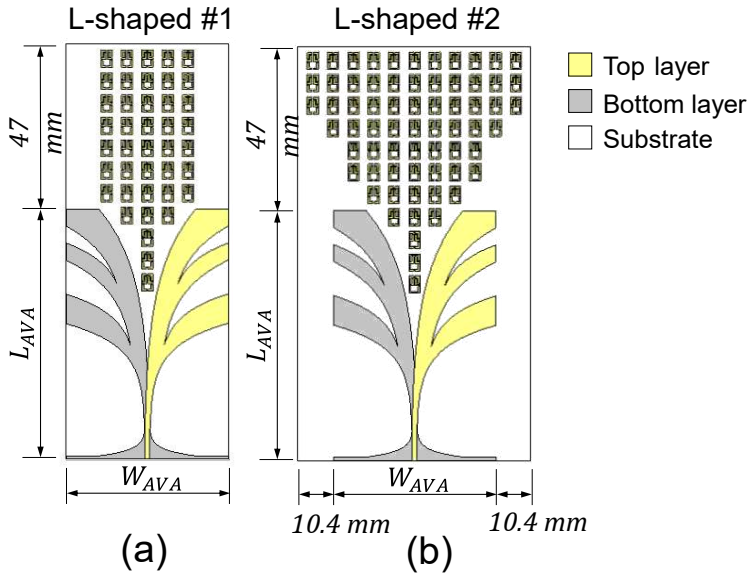

Figure 4.19 Schematic of AVA with L-shaped metalenses: (a) AVA L-shaped#1, array of 41 L-shaped unit cells, and (b) AVA L-shaped#2, triangular array of 67 L-shaped unit cells [6].

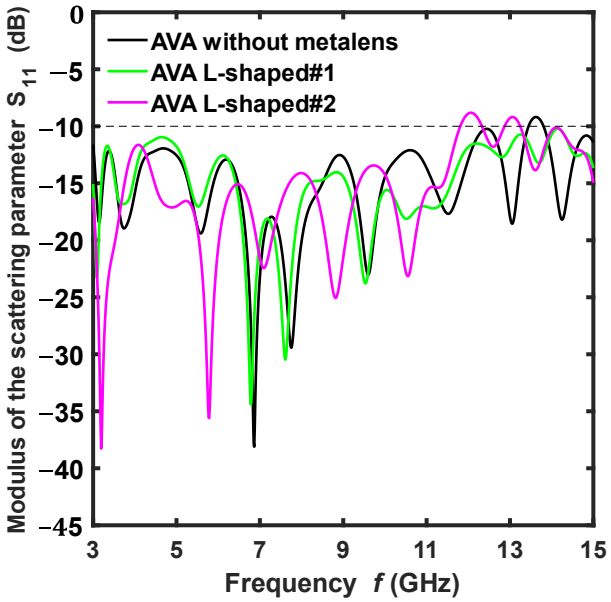

Figure 4.20 Full-wave simulation of the AVA with different L-shaped metalenses: modulus of the scattering parameter S_{11} as a function of frequency f [6].

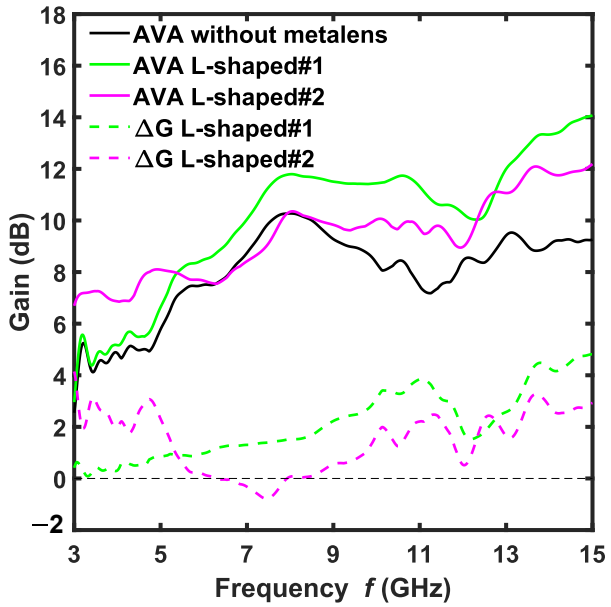

Figure 4.21 Full-wave simulation of the AVA with different L-shaped metalenses: realized gain G and gain increase ΔG as a function of frequency f [6].

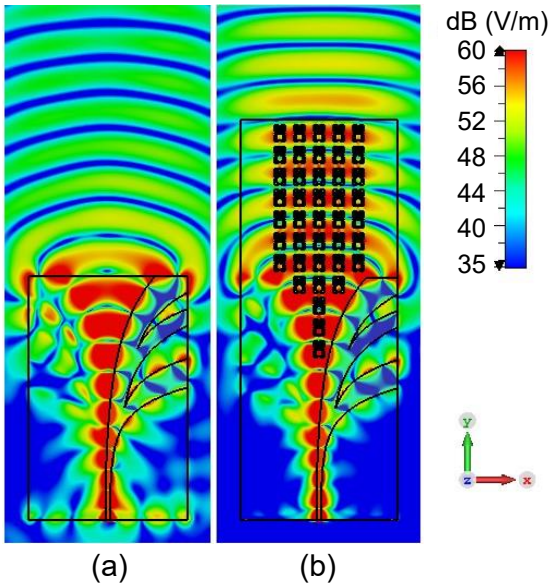

Figure 4.22 Full-wave simulation of the E-field distribution in $xy-$plane at $f = 14\ GHz$ of (a) AVA without metalens and (b) AVA-L-shaped#1 [6].

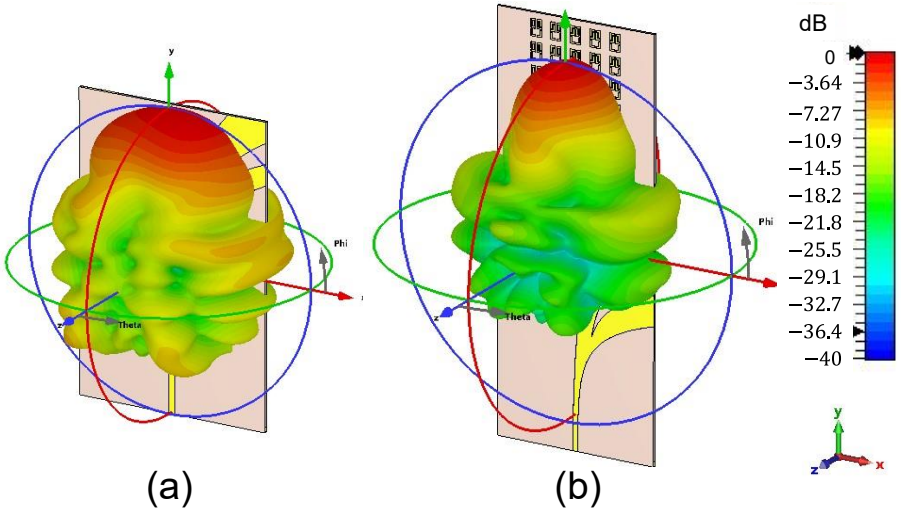

Figure 4.23 Full-wave simulation of the normalized radiation patterns 3D view at frequency $f = 14\ GHz$ of (a) AVA without metalens and (b) AVA L-shaped#1 [6].

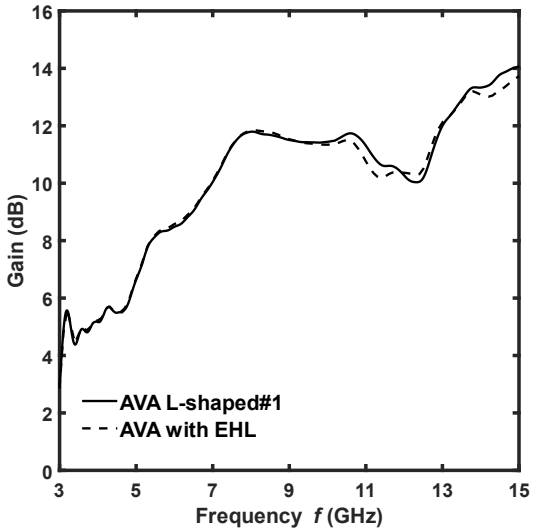

Figure 4.24 Full-wave simulation of the gain G as a function of frequency for AVA L-shaped#1 (solid curve) and AVA with EHL, having thickness $d_{EHL} = 0.832\,mm$ and values of permittivity $\varepsilon_r = 4.98$ and permeability $\mu_r = 0.75$ (dashed curve) [6].

4.4 Measurements

Antenna prototypes, AVA, and AVA with metalens, have been fabricated with Rogers RO4350B dielectric substrate, with $\varepsilon_r = 3.66$ and $tan\delta = 0.0037$, by using the easy and low-cost PCB fabrication process.

4.4.1 AVA SRR prototypes

Figure 4.25shows the antenna prototypes AVA, AVA SRR#1, AVA SRR#2, and AVA SRR#3. The geometrical parameters are listed in Table 4.I and Table 4.II. They have been characterized with the N5224A PNA Microwave Network Analyzer and the Satimo StarLab Antenna Pattern Measurement System.

Figure 4.26 shows the measured modulus of the scattering parameter $|S_{11}|$ as a function of frequency f for all the AVA prototypes. The experimental results confirm the $-10\,dB$ bandwidth over the entire band $f = 3\,GHz \div 13\,GHz$ in all cases.

Figure 4.27 shows the comparison between simulated (solid curves) and measured (dotted curves) gain G as a function of frequency f for the four AVA antennas. The experimental results agree with the simulations, confirming that the designed metalenses allow a gain improvement over the entire band in the case

of AVA SRR#1 and AVA SRR#2, and at low frequencies for AVA SRR#3. A maximum gain of $G_{max} = 11.5\ dB$ at $f = 13\ GHz$ for AVA SRR#1, of $G_{max} = 11.4\ dB$ at $f = 8.6\ GHz$ for AVA SRR#2, and of $G_{max} = 12\ dB$ at $f = 8.6\ GHz$ for AVA SRR#3, have been measured.

Figure 4.28 allows an easier comparison between simulated (solid curves) and measured (dotted curves) gains, illustrating the increase ΔG of the three AVA with metalens with respect to the AVA without metalens. The measured curves are close enough with the simulated ones. Table 4.V summarizes the main results.

Figure 4.29 shows the measured E-plane and H-plane radiation patterns of the AVA with metalens compared to that of AVA without metalens at the frequencies where the maximum gain increase ΔG occurs. The measured Half-Power Beamwidth (HPBW) of the AVA is reduced over the entire band when the metalenses are integrated on the antenna. The measured $-3\ dB$ beamwidth in the H-plane is reduced from $HPBW_{AVA} = 46.36°$ to $HPBW_{SRR\#1} = 40.70°$ for AVA SRR#1 at $f = 12.3\ GHz$, from $HPBW_{AVA} = 51.27°$ to $HPBW_{SRR\#2} = 33.6°$ for AVA SRR#2 at $f = 12\ GHz$, and from $HPBW_{AVA} = 62.91°$ to $HPBW_{SRR\#3} = 43.29°$ for AVA SRR#3 at $f = 9\ GHz$.

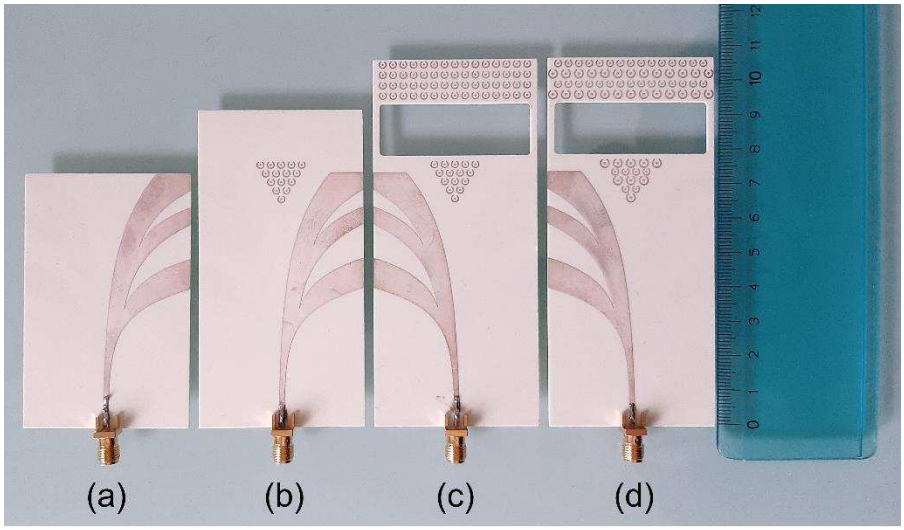

Figure 4.25 Fabricated prototypes: (a) AVA, (b) AVA SRR#1, (b) AVA SRR#2, and (c) AVA SRR#3 [7].

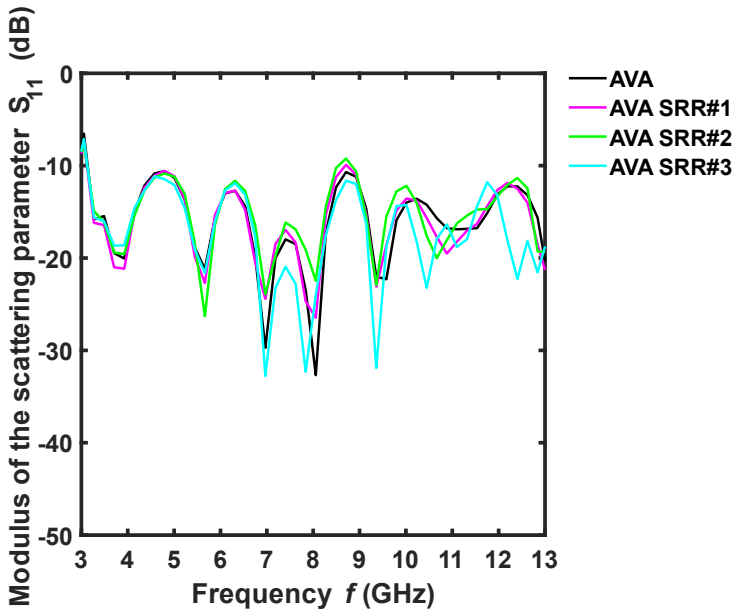

Figure 4.26 Measured modulus of the scattering parameter S_{11} as a function of the frequency f, for the AVA without metalens (black curve), the AVA SRR#1 (magenta curve), the AVA SRR#2 (green curve), and the AVA SRR#3 (cyan curve) [7].

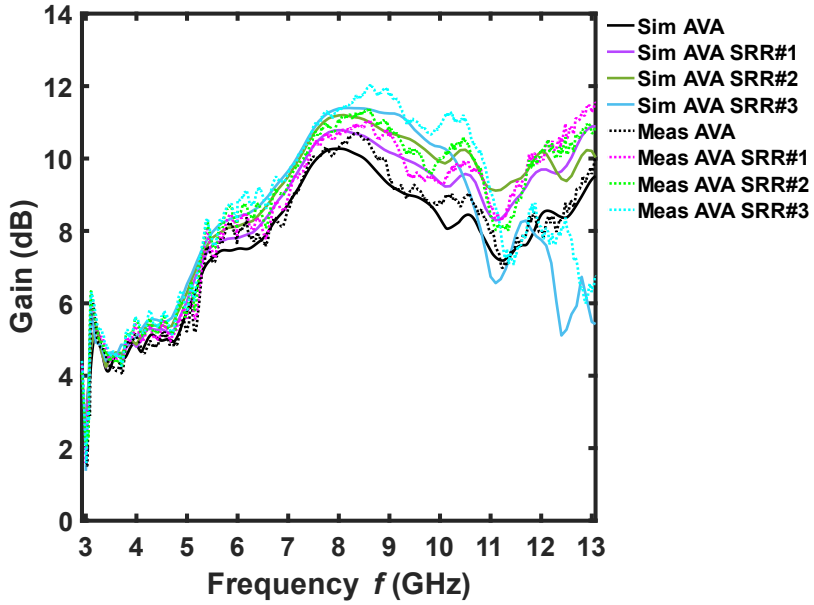

Figure 4.27 Simulated (solid curves) and measured (dotted curves) gain as a function of frequency f, for the AVA without metalens (black curve), the AVA SRR#1 (magenta curve), the AVA SRR#2 (green curve), and the AVA SRR#3 (cyan curve) [7].

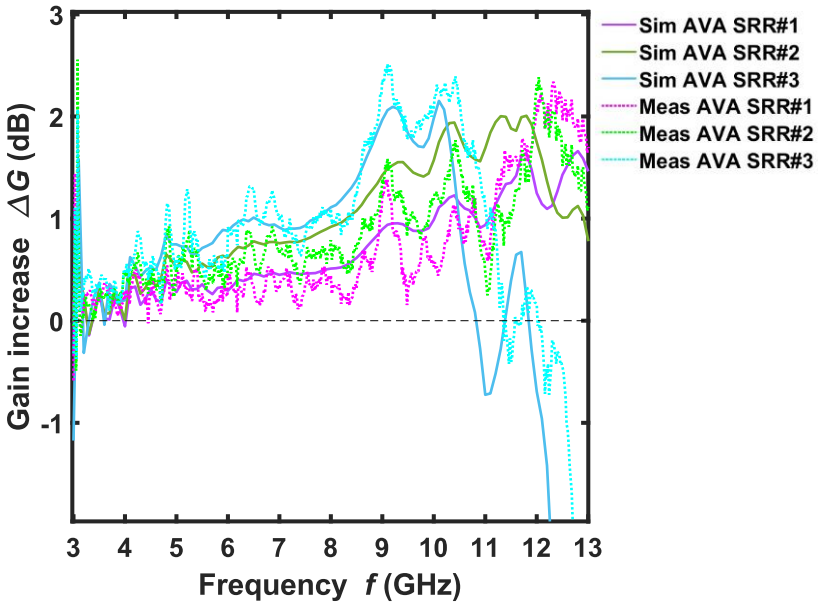

Figure 4.28 Simulated (solid curves) and measured (dotted curves) gain increase as a function of frequency f, for the AVA SRR#1 (magenta curve), the AVA SRR#2 (green curve), and the AVA SRR#3 (cyan curve) [7].

TABLE 4.V

SIMULATED AND MEASURED MAXIMUM GAIN G_{max} AND MAXIMUM GAIN INCREASE ΔG_{max} OF THE AVA SRR ANTENNAS.

	Simulated		*Measured*	
	Freq. (GHz)	G_{max} *(dB)*	*Freq. (GHz)*	G_{max} *(dB)*
SRR#1	12.9	10.8	13	11.5
SRR#2	8.1	11.2	8.6	11.4
SRR#3	8.2	11.4	8.6	12
	Freq. (GHz)	ΔG_{max} *(dB)*	*Freq. (GHz)*	ΔG_{max} *(dB)*
SRR#1	12.9	1.7	12.3	2.3
SRR#2	11.8	2	12	2.4
SRR#3	10.1	2.1	9	2.5

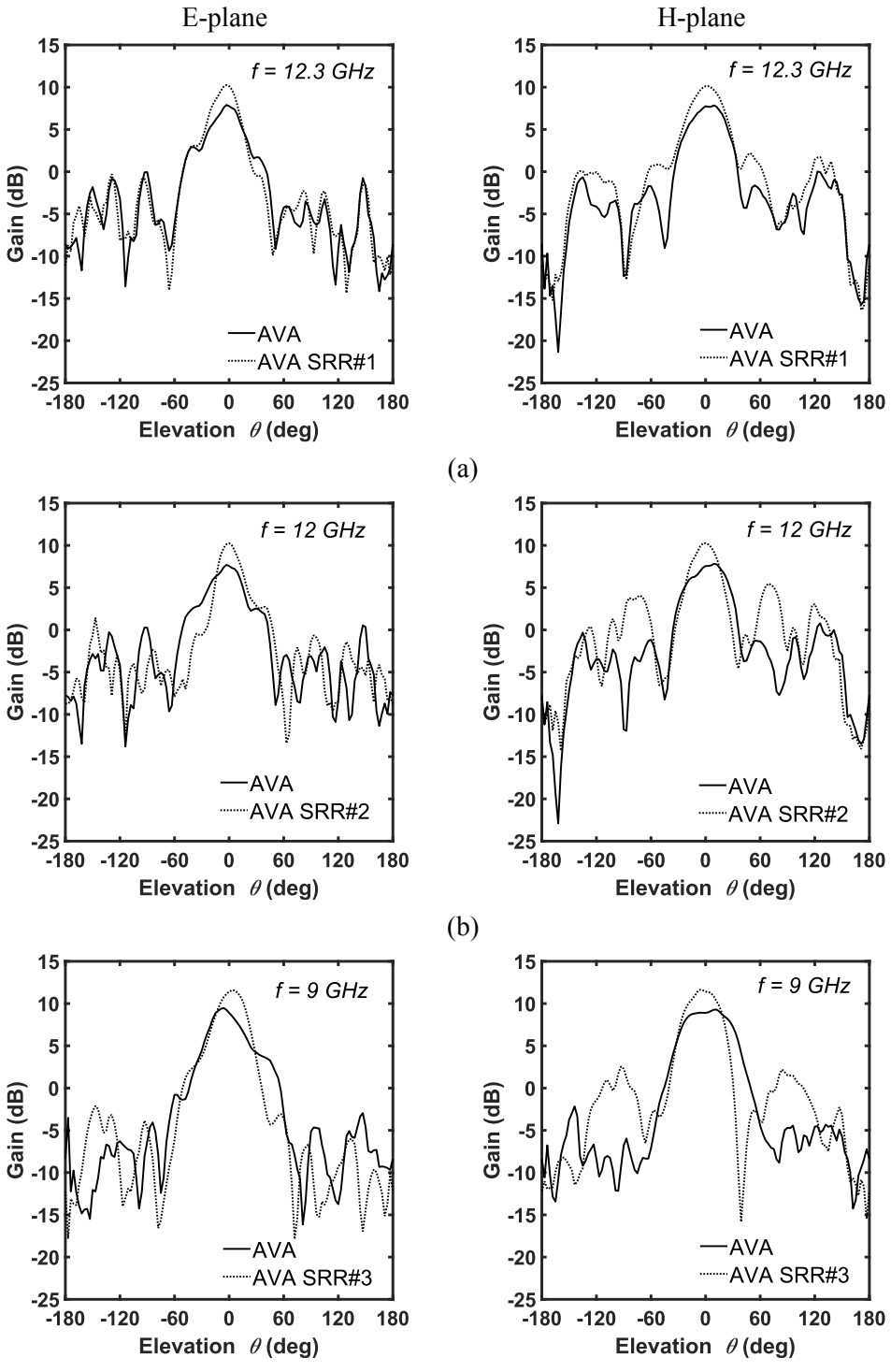

Figure 4.29 Measured E-plane (left column) and H-plane (right column) radiation patterns of the AVA (solid curve) and (a) AVA SRR#1 (dotted curve) at frequency $f = 12.3\ GHz$, (b) AVA SRR#2 (dotted curve) at frequency $f = 12\ GHz$, and (c) AVA SRR#3 (dotted curve) at frequency $f = 9\ GHz$ [7].

4.4.2 AVA L-Shaped prototype

The prototype AVA L-shaped#1 is shown in Figure 4.30. The scattering parameter S_{11}, input impedance Z_{ant}, and voltage standing-wave ratio (VSWR) versus the frequency of the two antennas have been measured with the Agilent Technologies N5224A PNA Network Analyzer. The calibration of the PNA has been performed with an N4693A 2-Port Electronic Calibration Module, setting the IF bandwidth to $IF_{BW} = 1\ KHz$ and the stimulus power to $P_s = -10\ dBm$. The uncertainty in the measured S_{11} parameter is $\pm 0.04\ dB$ for the magnitude and $\pm 0.264°$ for the phase. The radiation performance characterization has been performed with the antenna measurement system in an anechoic chamber, StarLab SATIMO. The system has been calibrated in gain with reference horn antennas. The uncertainty band of the instrument is $e_{gain} = \pm 0.7\ dB$. For the measurements, we have set a step of $\Delta f = 10\ MHz$ for linear frequency distribution and a grid size of $\Delta\theta = \Delta\phi = 4.5°$ for spatial resolution.

The simulated (solid curves) and the measured (dotted curves) moduli of the scattering parameter S_{11} as a function of the frequency, for the AVA (black curves) and AVA L-shaped#1 (green curves) are illustrated in Figure 4.31. The metalens allows an increase in the antenna bandwidth at high frequencies. A band of $f_{AVA} = 3 \div 13.5\ GHz$ for the AVA and an increased band of $f_{ava\ L\#1} = 3 \div 14.7\ GHz$ for the AVA L-shaped#1 have been measured. The simulated and measured curves are in good agreement.

The measured VSWRs of AVA and AVA L-shaped#1 prototype is $VSWR < 2$ in almost the whole operating frequency band. The introduction of the metalens reduces the VSWR for frequencies $f > 9.5\ GHz$. The measured antenna impedance of both prototypes varies around the characteristic impedance of the feed line $Z_c = 50\ \Omega$. The introduction of metalens slightly reduces the impedance mismatch at high frequencies, in agreement with the measured parameter S_{11} reported in Figure 4.31.

The simulated and measured gain of AVA and AVA L-shaped#1 as a function of the frequency is illustrated in Figure 4.32. A maximum gain $G_{max} = 10.7\ dB$ at a frequency of $f = 8.4\ GHz$ for the AVA and $G_{max} = 14.21\ dB$ at a frequency of $f = 14.6\ GHz$ for the AVA L-shaped#1 have been measured. The AVA L-shaped#1 has an improved gain with respect to the AVA over the whole bandwidth, especially for the frequencies $f > 8\ GHz$, where the measured average gain increase is about $\Delta G_{avg} = 3\ dB$ and the maximum measured gain

increase is $\Delta G_{max} = 4.8\ dB$ at a frequency of $f = 13.8\ GHz$. Additionally, for the gain, a good agreement between the simulation and measurement is obtained.

The E-plane and H-plane radiation patterns of the antenna prototypes have been measured and compared in the whole operating frequency band. The measured E-plane (solid curve) and H-plane (dashed curve) half-power bandwidths of the AVA (black curve) and AVA L-shaped#1 (green curve), as a function of the frequency, are illustrated in Figure 4.33. The HPBW of the antenna with metalens is reduced over the whole band in both planes, with a maximum HPBW reduction of $\Delta HPBW_{max} = 31.3°$ at a frequency of $f = 14\ GHz$ for the E plane and of $\Delta HPBW_{max} = 28.3°$ at a frequency of $f = 5\ GHz$ for the H plane. The difference between the beamwidths in the E and H planes is reduced after the insertion of the metalens, hence the radiation pattern is more symmetrical.

Figure 4.34 shows the E-plane and H-plane radiation patterns of AVA (dashed curve) and AVA L-shaped#1 (full curve), measured at frequencies $f = 14\ GHz$ and $f = 5\ GHz$ where the maximum HPBW reduction occurs.

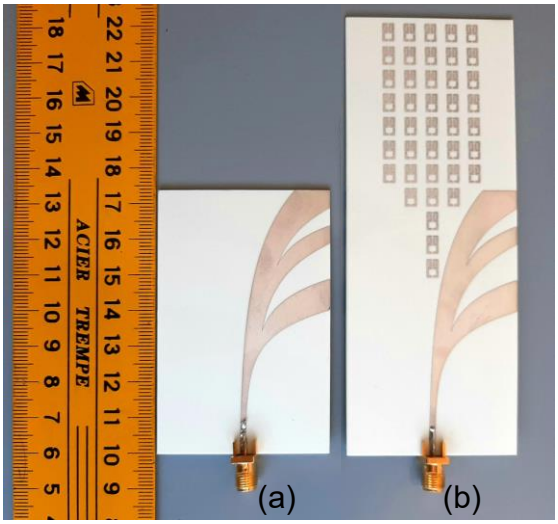

Figure 4.30 Prototypes of antipodal Vivaldi antenna without and with metalens: (a) AVA, and (b) AVA L-shaped#1 [6].

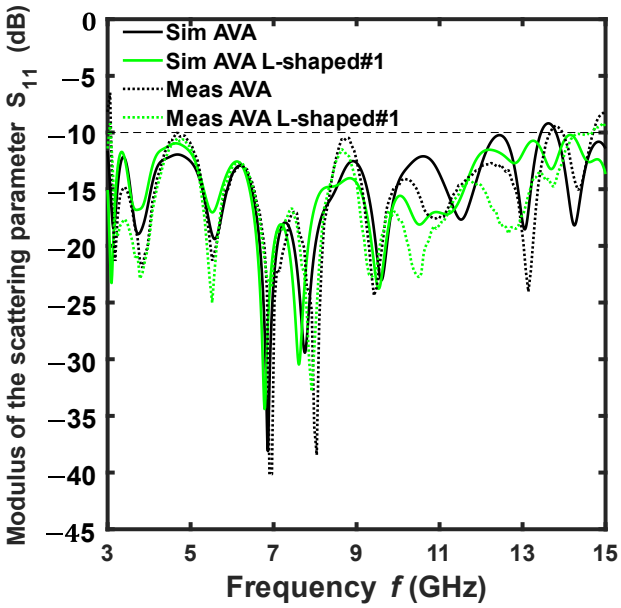

Figure 4.31 Comparison between full-wave simulation (solid curves) and measurement (dotted curves) of the AVA (black curves), and AVA L-shaped#1 (green curves): modulus of the scattering parameter S_{11} as a function of frequency f. [6]

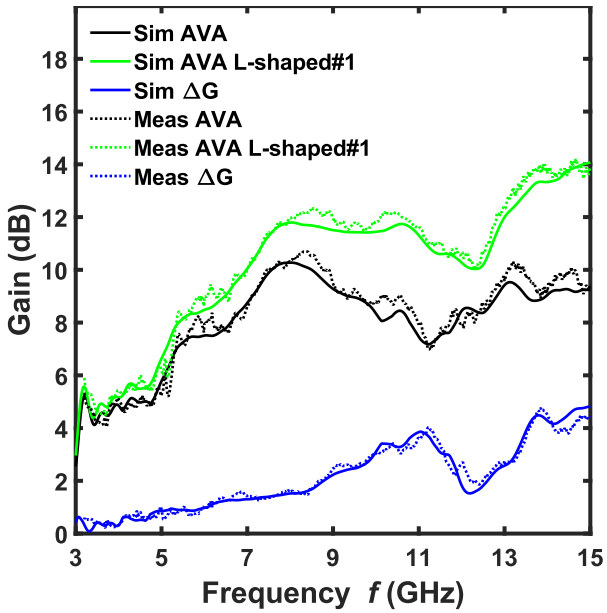

Figure 4.32 Comparison between full-wave simulation (solid curves) and measurement (dotted curves) of the AVA (black curves), and AVA L-shaped#1 (green curves): realized gain G and gain increase ΔG of frequency f [6].

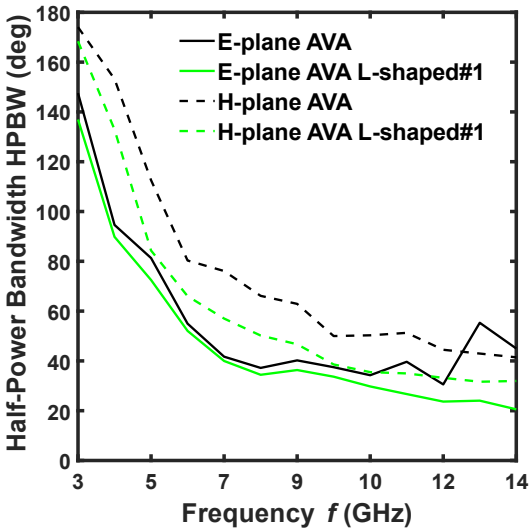

Figure 4.33 Measured E-plane (solid curve) and H-plane (dashed curve) half-power bandwidth of AVA (black curve) and AVA L-shaped#1 (green curve) as a function of frequency f . [6]

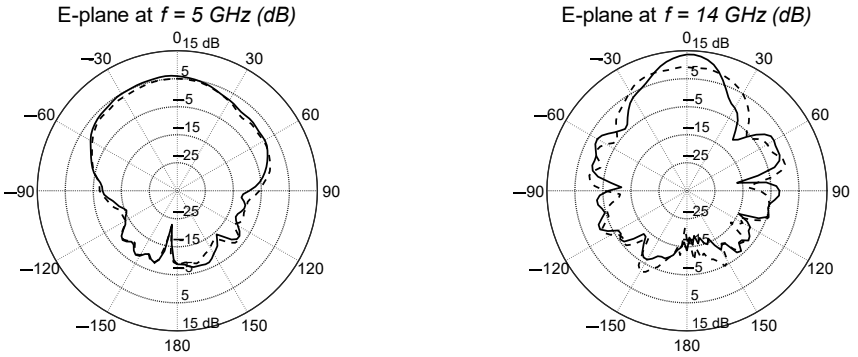

(a)

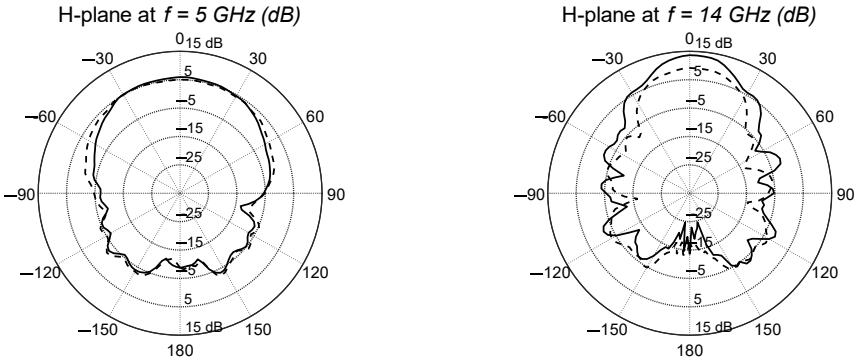

(b)

Figure 4.34 Simulated (solid curves) and measured (dotted curves) gain increase as a function of frequency f, for the AVA SRR#1 (magenta curve), the AVA SRR#2 (green curve), and the AVA SRR#3 (cyan curve) [6].

4.5 Comparison with literature

A comparison between the proposed AVAs with metalens and other AVAs reported in literature is shown in Table 4.VI. The comparison with the literature is not trivial if size, bandwidth, and gain are simultaneously considered. However, by comparing the measured performances of the proposed AVA L-shaped#1 with the state of the art, the size is smaller to parity of gain. As an example, the size of the AVA with a metalens [54] is $120 \times 260\ mm$, and a director element is employed in addition to the metalens. The size of AVA L-shaped#1 is $48 \times 121\ mm$, without a director. Regarding the AVAs SRR, the measured max gain is higher than that of [68,70,143-144] for similar operating bandwidth. Moreover, the AVAs SRR of this work enable higher miniaturization degree than that of [54-55,58-60]. The antenna reported in [54] allows a higher max gain but it benefits of both a metalens and a director element requiring a size increase.

TABLE 4.VI

EXPERIMENTAL RESULTS COMPARISON OF THE METALENSES INVESTIGATED AND SIMILAR PUBLISHED WORK

Ref	*Size* $(\lambda \times \lambda)^{(1)}$	*Operating Bandwidth* (GHz)	*Max Gain* G (dB)	*Max Gain Increase* ΔG (dB)
[54]	$5.8\lambda \times 12.6\lambda$	$1 \div 28$	14.6	nr
[55]	$5.3\lambda \times 2.5\lambda$	$24.1 \div 28.5$	14.0	nr
[58]	$1.7\lambda \times 3.1\lambda$	$6 \div 18$	12.0	3.6
[59]	$2.1\lambda \times 3.7\lambda$	$6 \div 18$	nr	2.5
[60]	$3.1\lambda \times 2.1\lambda$	$1.4 \div 12$	12.4	4
[66]	$1.3\lambda \times 1.4\lambda$	$0.7 \div 2.1$	nr[2]	1.9
[68]	$0.79\lambda \times 0.90\lambda$	$3.1 \div 10.6$	5.0	na[3]
[70]	$1.32\lambda \times 1.65\lambda$	$2.5 \div 14$	10.0	na
[143]	$1.30\lambda \times 1.52\lambda$	$3.7 \div 18$	6.9	na
[144]	$0.95\lambda \times 1.57\lambda$	$4.7 \div 11$	8.0	na
SRR#1	$1.28\lambda \times 2.45\lambda$	$3 \div 13$	11.5	2.3
SRR#2	$1.28\lambda \times 2.85\lambda$	$3 \div 13$	11.4	2.4
SRR#3	$1.28\lambda \times 2.85\lambda$	$3 \div 13$	12.0	2.5
L-Shaped#1	$1.4\lambda \times 3.5\lambda$	$3 \div 14.7$	14.2	4.8

(1) λ represents the wavelength at the center frequency of the operating bandwidth. (2) nr: not reported; (3) na: not applicable.

4.6 Concluding remarks

Metalenses have been designed and optimized in the frequency band of $f = 3 \div 15\ GHz$ in order to enhance the radiation performance of an antipodal Vivaldi antenna. Simulated and measured performances are in good agreement, confirming the improvement of the gain in a wide frequency range, preserving the operating bandwidth. A maximum gain of about $G_{max} = 12\ dB$ and a maximum gain increase of about $\Delta G_{max} = 2.5\ dB$ have been measured, for the AVA SRR#3 antenna. Moreover, the metalens L-shaped#1 improves both the pristine AVA bandwidth and the gain, especially at high frequencies. A maximum gain increase of $\Delta G_{max} = 4.8\ dB$ and a maximum HPBW reduction of $\Delta HPBW_{max} = 31.3°$ have been measured at the frequency of $f = 13.8\ GHz$ with respect to the pristine AVA. A frequency band of $f_{ava\ L\#1} = 3 \div 14.7\ GHz$, slightly larger than that of the pristine AVA, has been measured. The metalens L-shaped#2 can give better results at lower frequencies.

5 Design of a Substrate-Integrated Waveguide microwave device for sensing applications

5.1 Introduction

This chapter reports the design and the optimization of a planar microwave sensor based on Substrate-Integrated Waveguide (SIW) technology to detect water presence in diesel. Currently, standard methods used in laboratories for water contamination detection are relatively costly and lead substantial delays in analysis. An attractive alternative method is based on microwave sensors made with microstrip technology, that allow real-time and low-cost water in fuel detection [80-86]. In addition, microwave planar sensors are compact and highly integrated devices, however, the microstrip technology is characterized by low electromagnetic field confinement and radiant losses. A possible solution is given by SIW technology, that allows to reduce both the insertion and radiation losses, thanks to its good electromagnetic guidance and, at the same time, to obtain low profile and low-cost planar devices. Moreover, substrate-integrated waveguides have higher power handling capability [98–102].

In the following, the design of a microwave SIW applicator for water-in-fuel detection is reported. To the best of our knowledge, the microwave frequency range $f = 9 \div 11\ GHz$ is investigated to this aim for the first time, allowing the creation of a very compact device. The sensor characterization, using a vector network analyzer (VNA), confirms the simulation results with a quite good agreement. These performances are intriguing when compared to the literature results [87-88,95].

5.2 Design overview

The aim of the design is to obtain a low cost, planar/low-profile and compact (of few square centimetres) microwave applicator, providing good performance in terms of sensitivity and resolution, even if operating at a single frequency, to be employed in a simple online set-up, for example including a microwave source and an MW power meter.

The employed dielectric substrate is Rogers RT/Duroid 5880 ($\varepsilon_r = 2.2$, $tan\delta = 0.0009$) of commercial thickness $h_{sub} = 1.575\,mm$, whereas metallic parts are made of copper ($\sigma = 5.8 \times 10^7\ S/m$) with thickness $h = 0.035\,mm$.

The design, optimization, and characterization of the SIW applicator is performed with reference to both the air and water-in-diesel surrounding medium (background). For the case of the water-in-diesel background, a preliminary wideband investigation has been performed in order to obtain the real complex dielectric constant of some fuel samples containing different concentrations of contaminant water, as detailed in Paragraph 5.2.1 below.

5.2.1 Preliminary wide band investigation of fuel-water blend

The SIW microwave applicator is designed to work in the frequency range $f = 9 \div 11\ GHz$ with CST Studio Suite® software. This frequency range has been chosen by observing the behaviour of the complex dielectric permittivity of the fuel–water blend, on the basis of a wide-band investigation performed with a SPEAG DAK 3.5 probe [131] and a N9927A FieldFox Handheld Microwave Vector Analyzer by Keysight [145]. This preliminary investigation has highlighted changes in complex dielectric permittivity at the aforementioned frequencies, thus promising potential applications for sensing.

Five fuel samples have been prepared containing different concentrations of contaminant water. In particular, $\rho = 0\ ppm$ (pure diesel), $\rho = 50\ ppm$, $\rho = 200\ ppm$, $\rho = 500\ ppm$, and $\rho = 1000\ ppm$ of water have been prepared. Water concentrations higher than $\rho = 500\ ppm$ were not investigated because they are not interesting for practical applications, as they are over the acceptable limits regarding water contamination. The concentration $\rho = 1000\ ppm$ has been taken into account to verify the characteristics slope for extreme contaminations.

Figure 5.1 shows the SPEAG DAK 3.5 probe-N9927A VNA characterization set-up. For each sample, the dielectric constant measurement has been repeated seven times. These measurement results have been averaged to reduce measurement noise and fitted with a polynomial.

Table 5.I reports the order and the coefficient of determination R^2 of the polynomial fitting the five measured dielectric constant curves. The fitting order has been chosen to maximize R^2. The measured complex dielectric constants for the five samples as functions of the frequency are reported in Figure 5.2 (real part ε') and Figure 5.3 (imaginary part ε'').

It is worth observing that the real part ε' increases as the water concentration increases in a wide frequency range, $f = 8 \div 13\ GHz$. To obtain reference values for the ad-hoc designed water–diesel fuel blend SIW applicator, we directly considered the SPEAG DAK 3.5 probe-N9927A VNA-measured characteristics. In particular, by choosing different frequencies, e.g., $f = 9, 10, 11, 12, 13\ GHz$, different sensing characteristics, i.e., regression curves, can be drawn, as reported in Figure 5.4. At these frequencies, a direct proportionality between the water concentration ρ and the real part ε' occurs. Therefore, they are of interest for sensing applications. On the contrary, the frequencies $f < 7\ GHz$ or $f > 14\ GHz$ are not considered. The characteristics are quite similar, even if with a different coefficient of determination R^2, indicating the proportionate amount of variation in the response variable explained by the independent variable in the linear regression model. We underline that this preliminary investigation has been performed to roughly identify a frequency range where the variation in the complex dielectric constant with water concentration promises potential applications to be investigated.

Table 5.II reports the measured sensitivities for the five curves of Figure 5.4, confirming this observation. The direct proportionality between the real part ε' and the water concentration ρ pave the way to design an ad hoc water in diesel microwave sensor.

Figure 5.1 Characterization set-up with VNA Keysight N9927A FieldFox and DAK 3.5 probe [10].

TABLE 5.I

ORDER AND COEFFICIENT OF DETERMINATION R^2 OF THE POLYNOMIAL FITTING THE MEASURED DIELECTRIC CONSTANT CURVES.

Sample	*Fitting Order*	R^2 *of the Polynomial Fitting*
$\rho = 0\ ppm$	8	0.95
$\rho = 50\ ppm$	3	0.93
$\rho = 200\ ppm$	3	0.97
$\rho = 500\ ppm$	9	0.91
$\rho = 1000\ ppm$	8	0.90

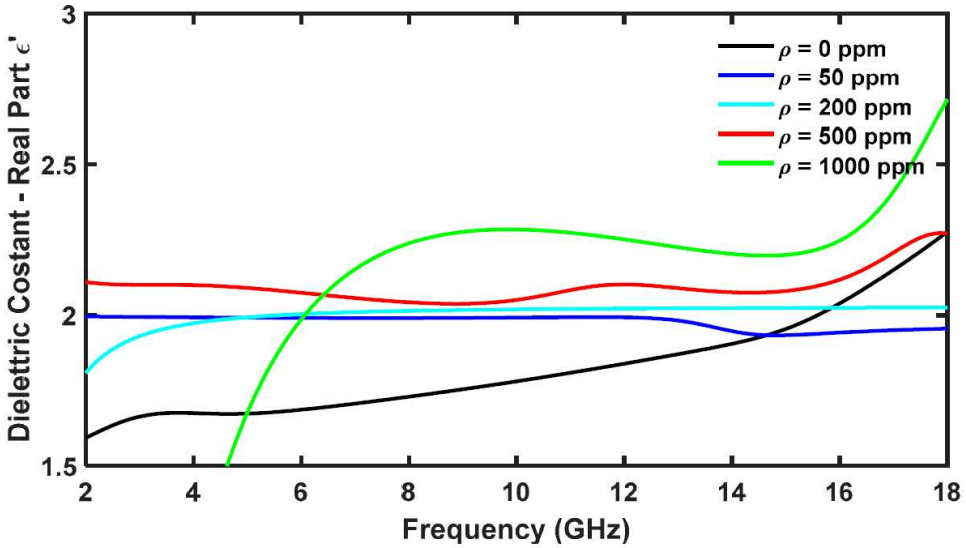

Figure 5.2 Measured real part ε' of the dielectric constant as a function of the frequency f for different water concentrations ρ in diesel [10].

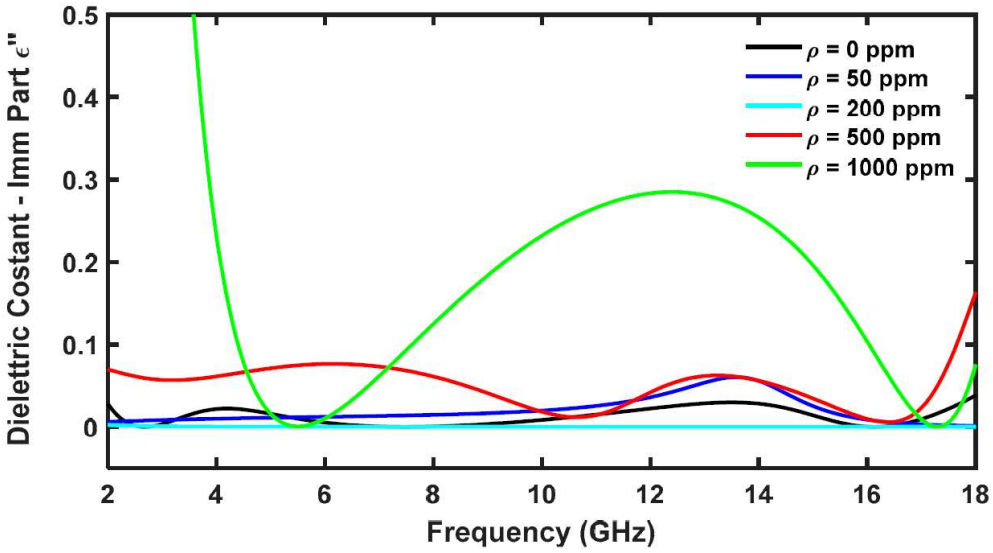

Figure 5.3 Measured real part ε' of the dielectric constant as a function of the frequency f for different water concentrations ρ in diesel [10].

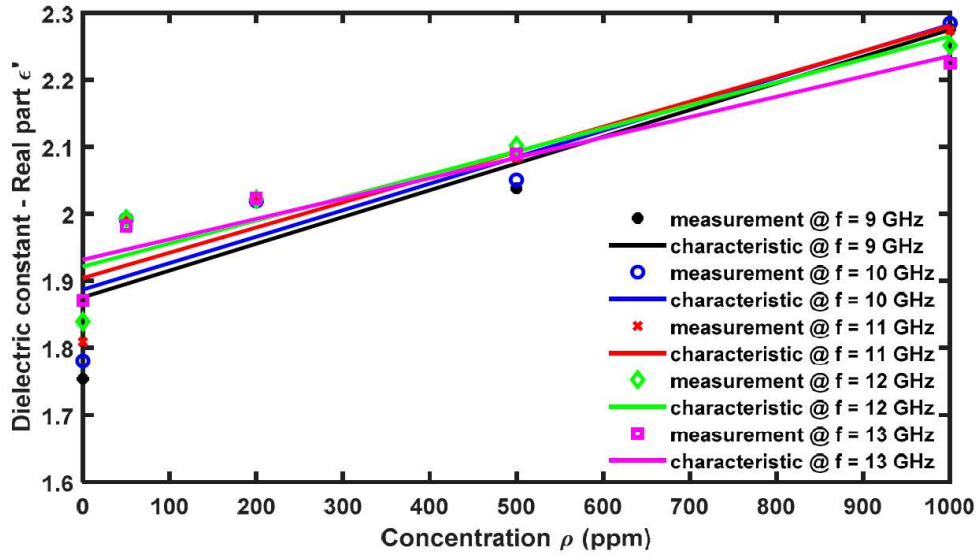

Figure 5.4 Real part ε' of the dielectric constant, measured with SPEAG DAK 3.5 probe-N9927A VNA, as a function of the water concentration ρ in diesel, for different frequencies [10].

TABLE 5.II
SENSITIVITIES OF THE SPEAG DAK 3.5 PROBE-N9927A VNA AS A WATER-IN-FUEL SENSOR FOR DIFFERENT FREQUENCIES.

Frequency	*Sensitivity* $\Delta\varepsilon_r/\Delta\rho$ $(\times 10^{-3}/ppm)$	R^2
9	0.399	0.79
10	0.395	0.82
11	0.376	0.86
12	0.344	0.88
13	0.304	0.91

5.2.2 SIW sensor with air background. Single slot configuration

The first geometry, reporting the main parameters, is shown in Figure 5.5. The preliminary values of the geometric parameters are reported in Table 5.III. The geometry depicted in Figure 5.5 is obtained considering a SIW guide fed by a microstrip line. The strip line sizes W_{feed} and L_{feed} are designed to ensure a characteristic impedance $Z_0 = 50\ \Omega$ [146]. The vias diameter d, the center–center distance s, and the other preliminary geometrical values are chosen following [98-102]. The slot ensures the radiation of the EM field and its interaction with the fuel samples.

Figure 5.6 shows the equivalent circuit of the single-slot SIW applicator [122,147-148]. The distributed-constants network, modelling the input and output microstrip transmission lines, includes the series impedance $Z = R + j\omega L$ per unit length and the shunt admittance $Y = G + j\omega C$ per unit length. The inductance L_s and the capacity C_s model the transverse slot [147-148].

Figure 5.7 shows the distribution of the modulus of the electric field irradiated by the slot in the xy plane, i.e., at the upper metal layer. The discontinuity between the feeding microstrip line and the SIW tends to confine the electric field near to the slot, as in a slotted resonant-like structure, improving the interaction with the fuel samples.

The first optimization regards the SIW length L_{guide}. Starting from the preliminary value reported in Table 5.III, $L_{guide} = 14\ mm$, larger values have been simulated until $L_{guide} = 20\ mm$, by considering a change step $\Delta L_{guide} = 2\ mm$. The extreme of the range $L_{guide} = 20\ mm$ is arbitrarily fixed to guarantee a high compactness degree. The modulus of the scattering parameters S_{11} and S_{21} as a function of frequency f for different values of the SIW length L_{guide}

has exhibited a bandwidth increase and an increased impedance matching at the fixed extreme value $L_{guide} = 20\,mm$. The optimization of the radiating slot is performed with the aim of further improving the device operation.

Figure 5.8 shows the modulus of the scattering parameters S_{11} (solid curves) and S_{21} (dotted curves) as a function of frequency f for different values of the slot width W_{slot}. As the slot width becomes smaller, a better impedance matching can be observed. However, the extreme $W_{slot} = 0.2\,mm$ has been arbitrarily fixed to allow a sufficient interaction between measurand background and EM field. Many other optimizations have been performed by varying slot length L_{slot}, center–center vias distance s, and vias diameter d, however, the performances fell short.

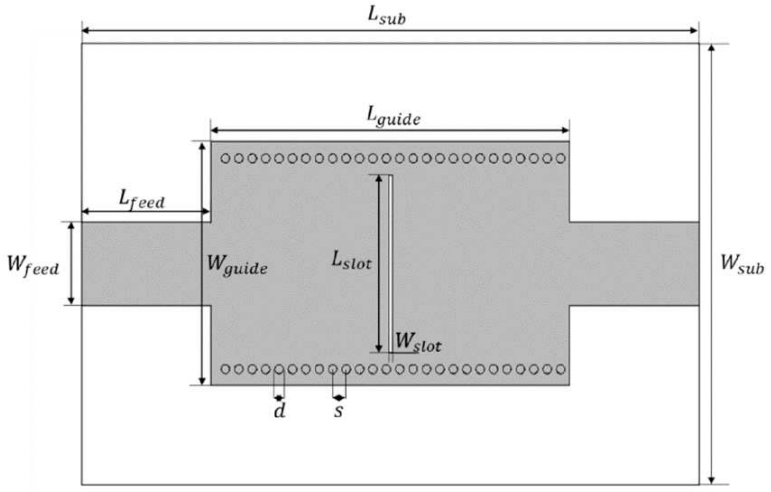

Figure 5.5 Scheme of the designed single-slot SIW applicator in air [10].

TABLE 5.III

MAIN GEOMETRIC PARAMETERS OF THE DESIGNED SINGLE-SLOT SIW APPLICATOR IN AIR

Parameter	*Value* (mm)	*Description*
L_{sub}	35	Substrate length
W_{sub}	25	Substrate width
L_{guide}	14.3	SIW length
W_{guide}	13.8	SIW width
L_{feed}	10.35	Microstrip line length
W_{feed}	4.7	Microstrip line width
L_{slot}	10.05	Slot length
W_{slot}	0.3	Slot width
s	0.75	Centre-centre distance of vias
d	0.5	Vias diameter

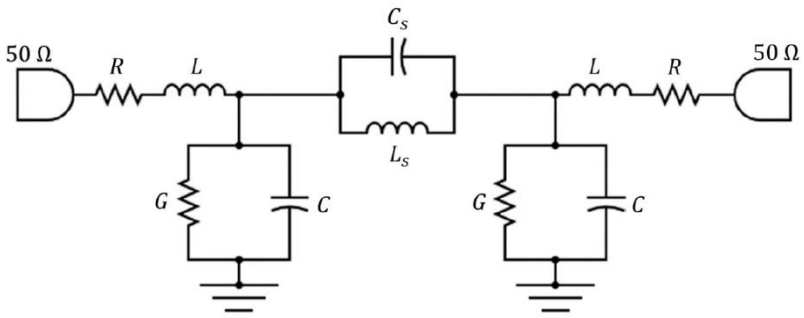

Figure 5.6 Equivalent circuit of the single-slot SIW applicator [10].

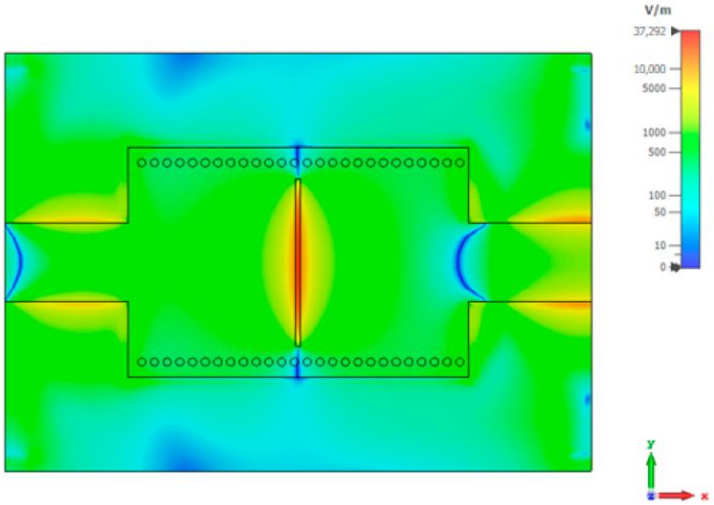

Figure 5.7 Modulus of the electric field irradiated by the slot in the xy −plane, single-slot SIW applicator in air [10].

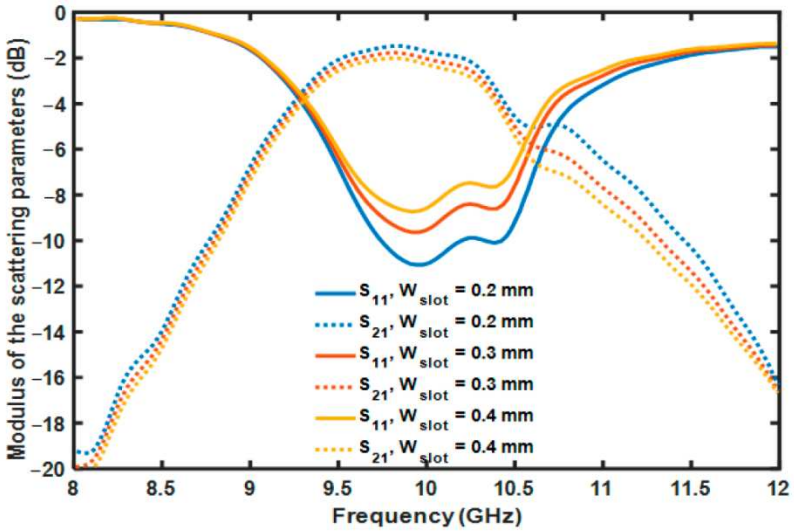

Figure 5.8 Modulus of the scattering parameters S_{11} (solid curves) and S_{21} (dotted curves) as a function of frequency f for different values of the slot width W_{slot} [10].

5.2.3 SIW sensor with air background. Cross slot configuration

The SIW applicator geometry is modified with the aim to improve the sensing performances. Two half geometries, allowing half mode behaviour, of the previous applicator are placed in close position and coupled via a gap, named the horizontal slot. The further, horizontal, slot is designed to enhance the interaction between the EM field and the fuel samples. The new geometry, reporting the main parameters, is shown in Figure 5.9. The preliminary values of the geometric parameters are reported in Table 5.IV. For this SIW applicator, asymmetric input, and output microstrip lines are designed. This is justified by considering that it is similar to the composition of two half-mode structures.

Figure 5.10 shows the equivalent circuit of the cross-slot SIW applicator [122,147-148]. The equivalent circuit is composed by two circuits like the previous one. Each of them refers to one of the two half-mode structures. The proximity coupling is modelled via the mutual inductance of M_{12}, the effect of the cut on the half-mode structure is modelled by a properly high value load impedance Z_L.

The SIW length is again set at $L_{guide} = 20\ mm$. The optimization has regarded the parameters of slot width W_{slot}, slot length L_{slot}, and gap width W_{gap}. For the slot width W_{slot}, the parametric investigation is performed in the range $W_{slot} = 0.2 \div 0.4\ mm$. The modulus of the scattering parameters S_{11} and S_{21} as a function of the frequency f for different values of slot width W_{slot} is simulated. As the slot width W_{slot} decreases, the impedance matching increases. The best value is $W_{slot} = 0.2\ mm$. This value is a trade-off. A narrower slot is not investigated, as previously discussed in Paragraph 5.2.2. Moreover, good impedance matching with $|S11| = -22\ dB$ at the frequency of $f = 9.6\ GHz$ is reached. A further decrease in the length of W_{slot} is not interesting and could cause an interaction reduction with the background.

The gap width W_{gap} is varied in the range of $W_{gap} = 0.2 \div 0.4mm$. Figure 5.11 shows the modulus of the simulated scattering parameters S_{11} (solid curves) and S_{21} (dotted curves) as a function of the frequency f for different values of gap width W_{gap}. Additionally, the gap width modifies the applicator impedance matching. The best value is $W_{gap} = 0.2\ mm$, ensuring the maximum transmission bandwidth and the minimum scattering parameter modulus $|S_{11}|$. The impedance matching with $|S_{11}| = -23\ dB$ at the frequency $f = 9.6\ GHz$ is obtained.

The slot length L_{slot} is varied in the range of $L_{slot} = 4.9 \div 5.3\ mm$ in order to ensure the maximum interaction between the fuel sample and the sensor. The modulus of the scattering parameters S_{11} and S_{21} as a function of the frequency f has been simulated for different values of L_{slot}. As the slot length L_{slot} decreases, the impedance matching increases, and the bandwidth becomes larger. The impedance matching with $|S_{11}| = -19\ dB$ at the frequency of $f = 9.6\ GHz$ is simulated for $L_{slot} = 4.9\ mm$.

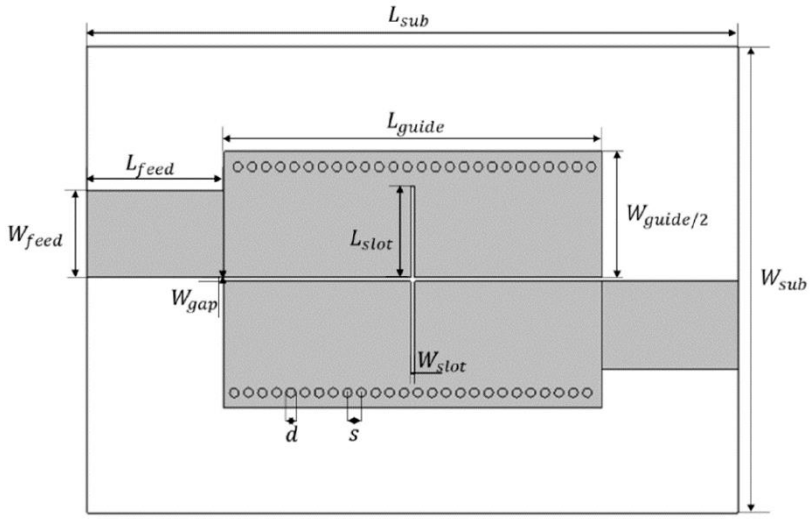

Figure 5.9 Scheme of the designed cross-slot SIW applicator [10].

TABLE 5.IV

MAIN GEOMETRIC PARAMETERS OF THE DESIGNED CROSS-SLOT SIW APPLICATOR.

Parameter	*Value* (mm)	*Description*
L_{sub}	35	Substrate length
W_{sub}	25	Substrate width
L_{guide}	20.3	SIW length
$W_{guide}/2$	6.9	Half SIW width
L_{feed}	7.5	Microstrip line length
W_{feed}	4.7	Microstrip line width
L_{slot}	4	Slot length
W_{slot}	0.3	Slot width
W_{gap}	0.3	Gap width
s	0.75	Centre-centre distance of vias
d	0.5	Vias diameter

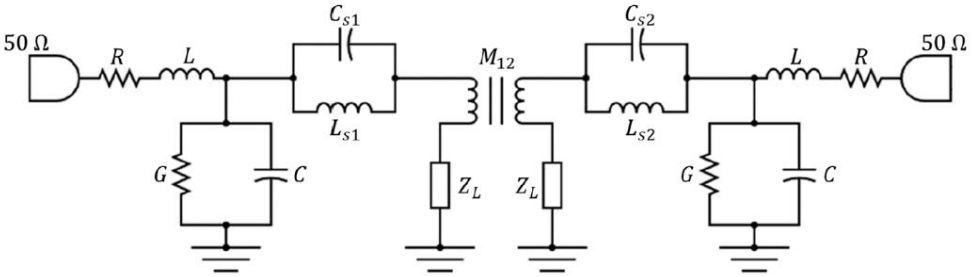

Figure 5.10 Equivalent circuit of the cross-slot SIW applicator [10].

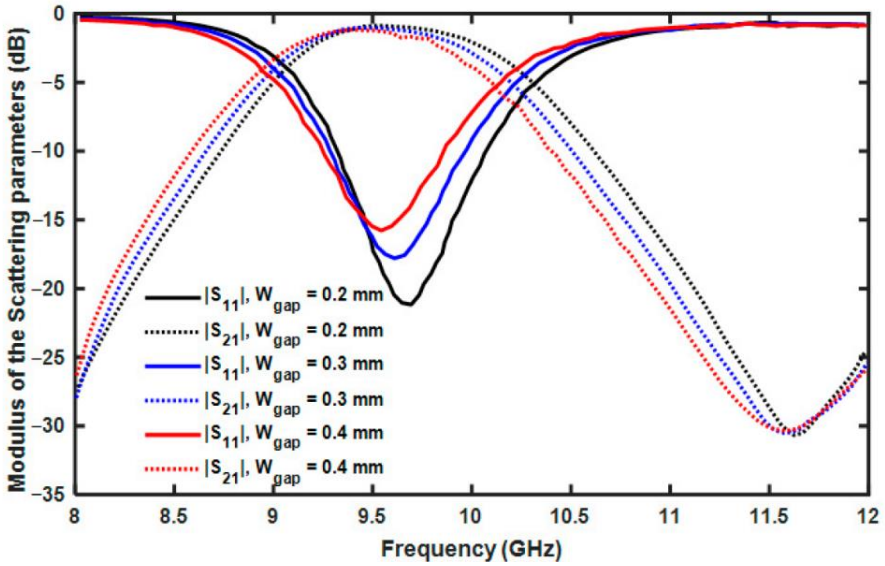

Figure 5.11 Modulus of the scattering parameters S_{11} (solid curves) and S_{21} (dotted curves) as a function of frequency f for different values of the slot width W_{gap} [10].

5.3 Simulation results

After all the optimizations, the optimal geometrical dimensions for the cross-slot SIW device are reported in Table 5.V. These values ensure a good impedance matching and the wide bandwidth in the $f = 9 \div 10\ GHz$ range. The device is also compact and low-profile.

To evaluate the cross-slot SIW applicator performances as a water-in-fuel sensor, the measured dielectric constants of the five samples have been imported into the simulation CST Studio Suite® software. A similar investigation to that reported in Paragraph 2.3 has been performed, showing that the same SIW

structure could be employed with a water-in-diesel background, allowing a promising performance without further refinement. In other words, the dielectric constant of air and the real part ε' of the diesel dielectric constant at the considered frequencies f are sufficiently close.

In fact, Figure 5.12 illustrates the modulus of the scattering parameters S_{11} (solid curves) and S_{21} (dotted curves) as a function of the frequency f for air (black curve) and pure diesel (blue curve) backgrounds. The impedance matching with $S_{11} = -18\,dB$ at the frequency $f = 9.5\,GHz$ for the diesel background is good enough.

The percentage change on the modulus of the scattering parameter S_{21}, obtained by simulating the diesel sample in contact and placed at the distance $d_{air} = 0.1\,mm$ from the top metallic layer, is below $\Delta S_{21} = 9\%$. However, the distance d_{air} can be eliminated in practical application after an easy mechanical optimization.

The percentage change in the modulus of the scattering parameter S_{21} obtained by simulating the diesel sample in contact with the top metallic layer and the radiating slots filled with diesel and filled with air is of the order of $\Delta S_{21} = 1.3\%$. Additionally, this error can be eliminated by a direct contact of the applicator with diesel flux.

Figure 5.13a shows the modulus of the simulated scattering parameter S_{21} as function of the frequency f for the five different water concentrations. Figure 5.13b is a magnified view of the matching frequency $f = 9.5\,GHz$. It shows that, as the water concentration increases, the modulus of the scattering parameter S_{21} decreases. The variation is quite linear. The values of the modulus of the scattering parameter S_{21} for the five water concentrations at frequency $f = 9.2\,GHz$ are listed in Table 5.VI. The simulated sensor sensitivity can be calculated as:

$$\frac{\Delta|S_{21}|}{\Delta\rho} = 1.39\,mdB/ppm\ @\ 9.2\,GHz$$

The coefficient of determination is $R^2 = 0.85$, which is quite good.

TABLE 5.V

OPTIMIZED GEOMETRIC PARAMETERS OF THE CROSS-SLOT SIW APPLICATOR.

Parameter	*Value* (mm)	*Description*
L_{sub}	35	Substrate length
W_{sub}	25	Substrate width
L_{guide}	20	SIW length
$W_{guide}/2$	6.9	Half SIW width
L_{feed}	7.5	Microstrip line length
W_{feed}	4.7	Microstrip line width
L_{slot}	4.9	Slot length
W_{slot}	0.2	Slot width
W_{gap}	0.2	Gap width
s	0.75	Centre-centre distance of vias
d	0.5	Vias diameter

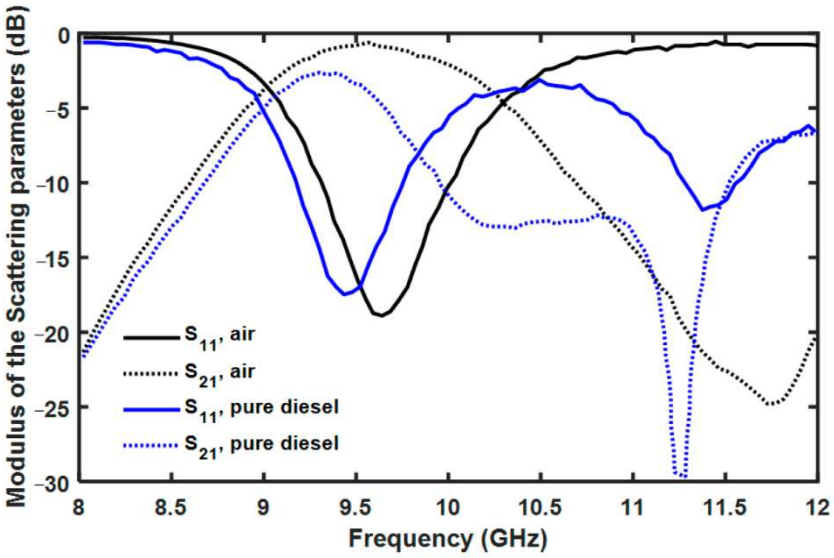

Figure 5.12 Cross-slot SIW applicator. Modulus of the simulated scattering parameters S_{11} (solid curves) and S_{21} (dotted curves) as a function of the frequency f for air (black curves) and pure diesel (blue curves) backgrounds [10].

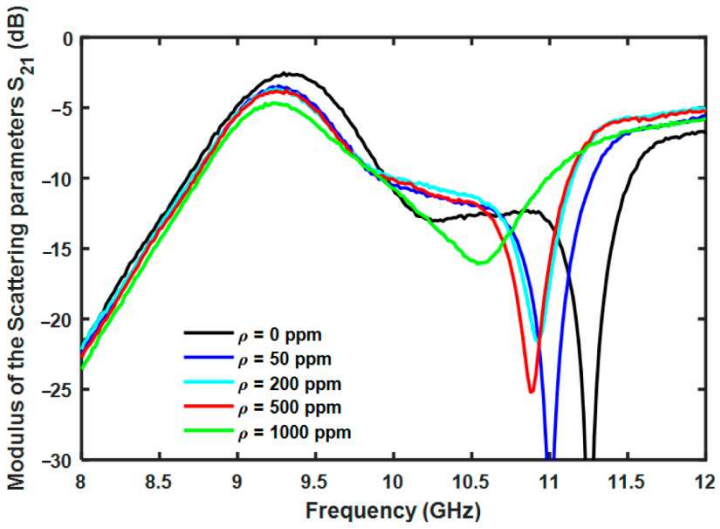

(a)

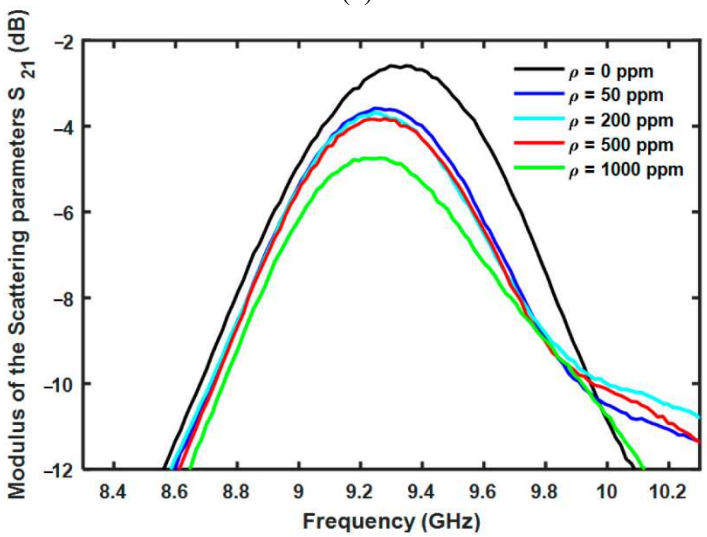

(b)

Figure 5.13 Cross-slot SIW applicator. (a) Modulus of the simulated scattering parameters S_{21} as a function of the frequency f for different water concentrations. (b) Zoom around $f = 8.3 \div 10.3\ GHz$ [10].

TABLE 5.VI

CROSS-SLOT SIW. MODULUS OF THE SIMULATED SCATTERING PARAMETER S_{21} FOR THE FIVE WATER CONCENTRATIONS AT FREQUENCY $f = 9.2\ GHz$.

Water Concentration ρ (ppm)	$\lvert S_{21} \rvert$ @9.2 GHz (dB)
0	−3.033
50	−3.718
200	−3.827
500	−3.930
1000	−4.778

5.4 Measurements

The cross-slot SIW prototype have been fabricated by employing the dielectric substrates Rogers RT/duroid 5880 with $\varepsilon_r = 2.2$ and $tan\delta = 0.0009$ by using a standard PCB process. Figure 5.14 shows the fabricated device.

The applicator has been characterized by using the VNA Keysight FieldFox, considering as the background: i) air, i.e., without the fuel sample to be detected, and ii) the same fuel samples, characterized in Paragraph 5.2.1 and simulated in Paragraph 5.3.

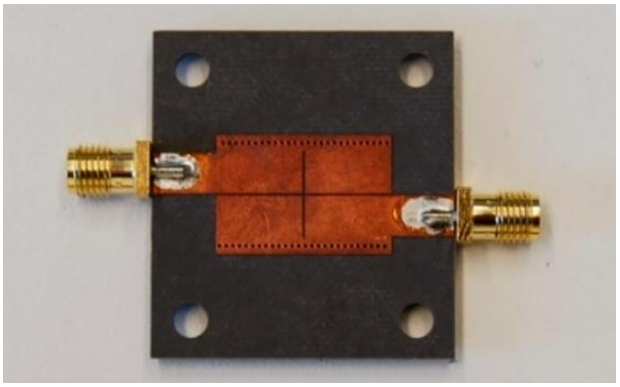

Figure 5.14 Constructed cross-slot SIW applicator [10].

5.4.1 Characterization in air background

The measured modulus of the scattering parameters S_{11} and S_{21} as a function of the frequency f is shown in Figure 5.15 (solid curves) and compared with the simulated parameters (dotted curves). The results are in agreement with the simulations. A right shift of about $\Delta f = 0.5\ GHz$ can be seen for both S_{11} and S_{21} curves. This behavior can be caused by the fabrication tolerance leading to a little mismatch between the geometric dimensions of the fabricated device and the nominal/optimized ones reported in Table 5.V.

5.4.2 Characterization in water-in-diesel background

The complete measurement set-up is shown in Figure 5.16a. It is composed by the VNA Keysight FieldFox, connected to the constructed cross-slot SIW applicator. Figure 5.16b shows the plastic bag with the fuel sample placed on the applicator. Its stability is ensured by an appropriate support. The bag containing the fuel samples is constituted by polyethylene.

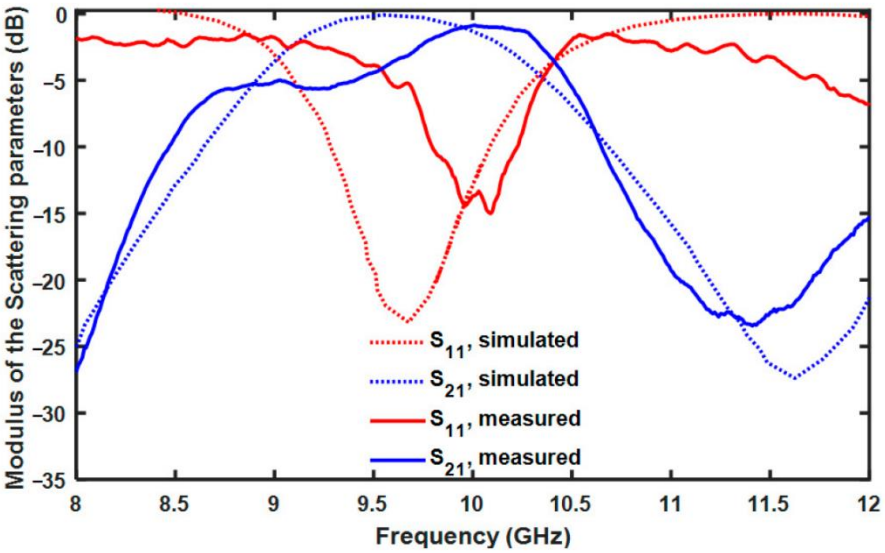

Figure 5.15 Cross-slot SIW applicator with air as the background. Modulus of the scattering parameters S_{11} and S_{21} as a function of the frequency f for measured (solid curves) and simulated (dotted curves) [10].

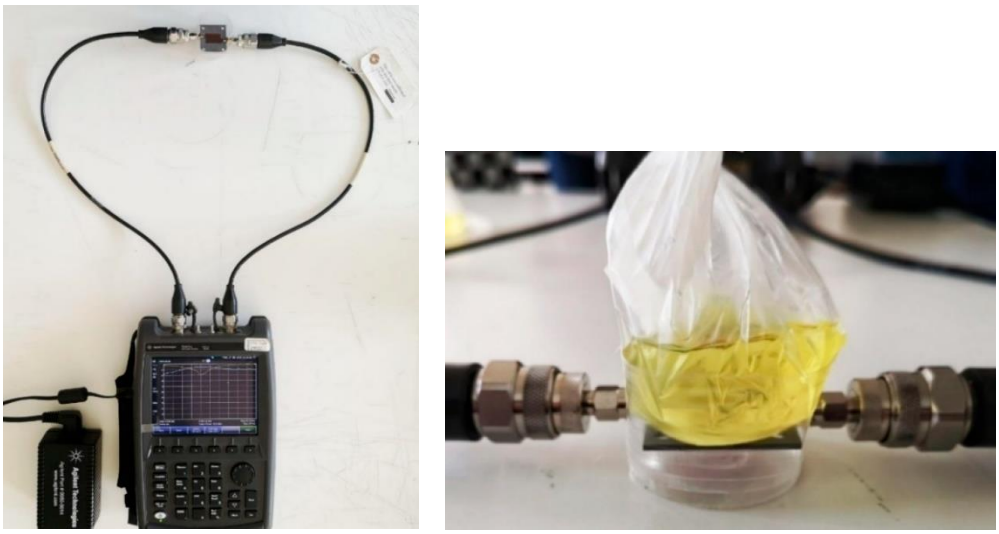

(a) (b)

Figure 5.16 (a) Measurement set-up using the Keysight VNA N9927A FieldFox and the constructed cross-slot SIW applicator as a water-in-fuel sensor; (b) magnified view of one of the measured fuel samples [10].

Figure 5.17 shows measurements proving that it can be considered transparent, allowing complete radiating field transmission, and does not affect the water-in-diesel characterization.

Figure 5.18a shows the measured modulus and Figure 5.18b the measured phase of the scattering parameter S_{11} as a function of the frequency f, for the five

different water concentrations ρ. These curves do not allow us to easily obtain a sensing characteristic since no change proportional with the water concentration is observed.

Figure 5.19a shows the measured modulus and Figure 5.19b the measured phase of the scattering parameter S_{21} as a function of the frequency f for the five different water concentrations ρ. As expected, no S_{21} phase shift can be observed with variations in water concentration. On the contrary, the measured modulus varies quite linearly, as predicted by simulations. It is affected by the radiated power interacting with the sample, which allows the sensor operation. As for the simulated parameters of Figure 5.15, the modulus of the scattering parameter S_{21} decreases as the water concentration increases, showing an inverse proportionality. Table 5.VII reports the values of the measured modulus of the scattering parameter S_{21} for the different concentrations at a frequency of $f = 9.76\ GHz$, where the $|S_{21}|$ is maximized for all the five curves.

Figure 5.20 shows the measured modulus of the scattering parameter S_{21} as a function of the water concentration ρ. The proportionality is quite linear, so it is possible to calculate the sensitivity as

$$\frac{\Delta|S_{21}|}{\Delta\rho} = 1.42\ mdB/ppm\ @\ 9.76\ GHz$$

The coefficient of determination is $R^2 = 0.94$, which is in excellent agreement with the simulation illustrated in Paragraph 4. Considering the VNA N9927A resolution $\Delta S_{21} = 0.01\ dB$, the proposed set-up is able to measure a minimum variation in water concentration of $\Delta\rho \approx 7\ ppm$ [145]. The SIW applicator is intriguing for its compactness and performances even when compared with the literature [87-88,95]. It could be employed with a single frequency source and an MW power meter in order to obtain an online and low-cost system for diesel quality detection.

The response of the microwave sensor is practically immediate due to the instantaneous interaction of the microwave with the sample. It is worth noting that a potential industrial application for on-time / online measurement could be feasible if the water-in-diesel solution flowed in a microwave-transparent tube, in contact with the sensor like the bag used in this work. In this case, the tube walls should be continuously washed and in contact with the flow to be monitored, thus allowing an instantaneous sensor response.

The influence of temperature on the applicator response is not significant for relatively substantial changes. In fact, the thermal expansion causes a negligible

variation in the sensor size and, as a consequence, a negligible variation in the chosen resonant frequency. This slight variation does not affect the applicator performance since it can operate over the wide frequency range of $f = 9 \div 11\ GHz$. Due to the temperature dispersion of the complex dielectric constant of the samples, a calibration could be required for large temperature changes.

The main limitation of the proposed applicator is the low selectivity. Generally, microwave sensors are characterized by a low selectivity, since they are based on the dielectric constant variation of the measured sample. Dielectric constant variation can depend on a number of potential contaminants/concentrations for a given wavelength. However, water contamination is the predominant one occurring in diesel production/supply chain, and the proposed microwave monitoring is interesting in practical application.

Table 5.VIII reports the comparison between the proposed applicator and the literature results. The proposed sensor exhibits the best sensitivity $\Delta|S_{21}|/\Delta\rho$ [87-88,95].

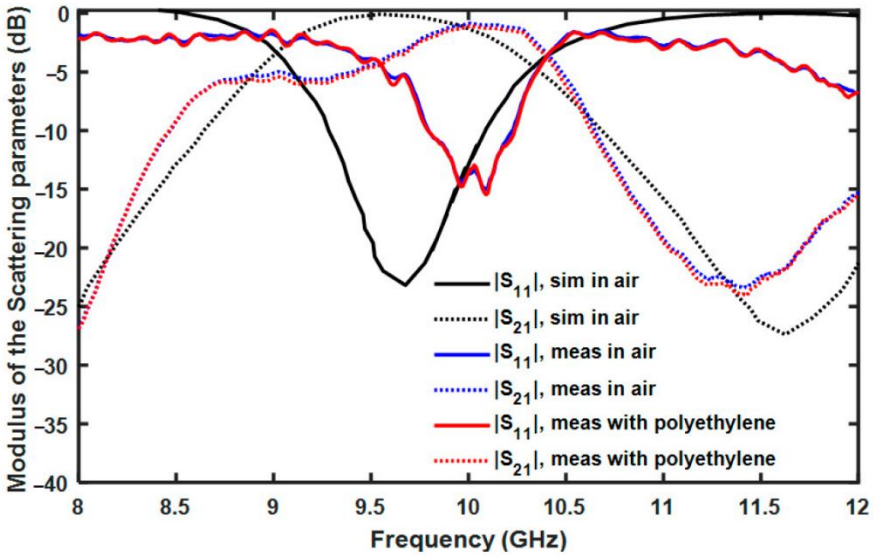

Figure 5.17 Cross-slot SIW applicator. Modulus of the scattering parameters S_{11} (solid curves) and S_{21} (dotted curves) as a function of the frequency f measured in air (blue curves), measured with polyethylene (red curve), and simulated (black curves) [10].

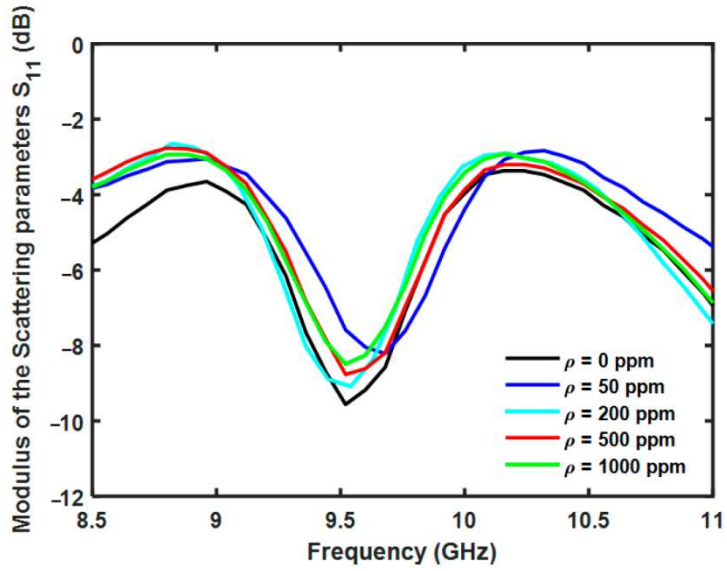

(a)

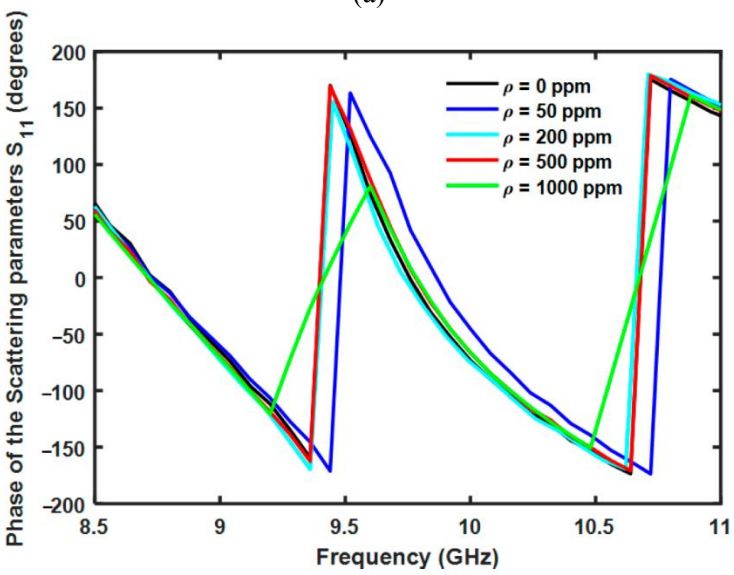

(b)

Figure 5.18 (a) Measured modulus of the scattering parameter S_{11} as a function of the frequency f and (b) measured phase of the scattering parameter S_{11} as a function of the frequency f for the five different water concentrations ρ [10].

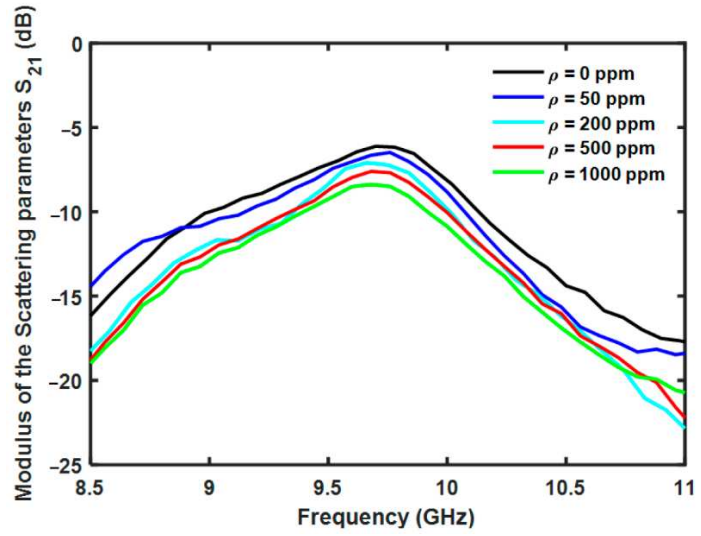

(a)

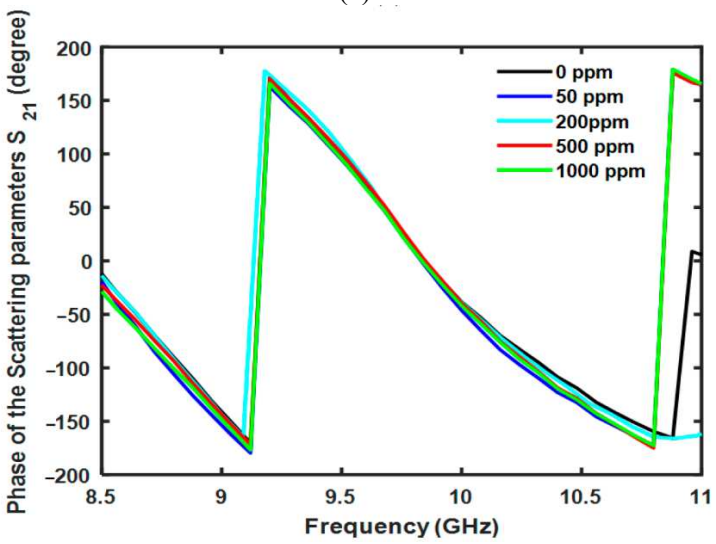

(b)

Figure 5.19 (a) Measured modulus of the scattering parameter S_{21} as a function of the frequency f and (b) measured phase of the scattering parameter S_{21} as a function of the frequency f for the five different water concentrations ρ [10].

TABLE 5.VII

MEASURED MODULUS OF THE SCATTERING PARAMETER S_{21} FOR THE FIVE WATER CONCENTRATIONS AT A FREQUENCY OF $f = 9.76\ GHz$.

Water Concentration ρ (ppm)	$\lvert S_{21}\rvert$ @$9.76\ GHz$ (dB)
0	−6.17
50	−6.48
200	−7.21
500	−7.68
1000	−8.49

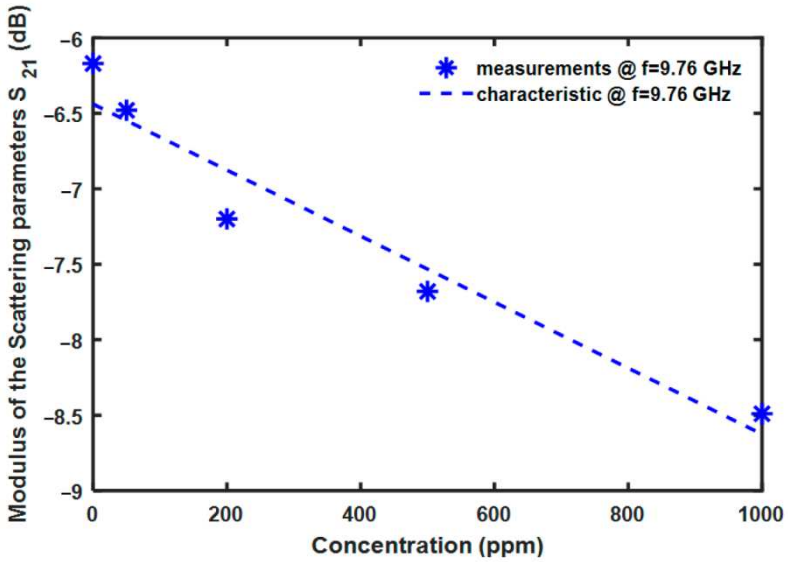

Figure 5.20 Measured modulus of the scattering parameters S_{21} as a function of water concentration ρ at frequency $f = 9.76\ GHz$ [10].

TABLE 5.VIII
MEASURED MODULUS OF THE SCATTERING PARAMETER S_{21} FOR THE FIVE WATER CONCENTRATIONS AT A FREQUENCY OF $f = 9.76\ GHz$.

References	*Sensitivity* $\Delta\|S_{21}\|/\Delta\rho$ (mdB/ppm)
[87]	0.4
[88]	0.6
[95]	0.0872
Cross-slot SIW applicator	1.42

5.5 Concluding remarks

A water-in-diesel sensor based on an SIW microwave applicator has been designed, constructed, and characterized. This characterization has confirmed the simulated performances in terms of bandwidth and impedance matching. Five water contaminated fuel samples have been characterized in terms of dielectric constant frequency dispersion with a SPEAG DAK 3.5 probe. The same samples have been detected with the designed SIW applicator allowing a water-in-diesel monitoring with a sensitivity of $\Delta|S_{21}|/\ \Delta\rho = 1.42\ mdB/ppm$ at a frequency of $f = 9.76\ GHz$ with a coefficient of determination $R^2 = 0.94$. The minimum variation in water concentration with the proposed set-up is $\Delta\rho = 7\ ppm$. The applicator is interesting because it is low-cost and low-profile, and it could be employed with a single frequency source and an MW power meter.

Conclusions

The design, fabrication, and characterization of different microwave resonant structures in the field of the medicine therapy and environmental monitoring have been performed. In particular:

i) An SRR-based metamaterial has been designed to be used as a lens for a SIW cavity backed patch applicator in superficial hyperthermia cancer treatment. A prototype has been fabricated and characterized. The simulated scattering parameter modulus of the antenna loaded with the biological tissue with and without metamaterial lens is $|S_{11}| = -37\ dB$ and $|S_{11}| = -14\ dB$ at the $f = 11\ GHz$ frequency, respectively. The measured minimum of the scattering parameter modulus $|S_{11}| = -42\ dB$ has been measured at the $f = 10.6\ GHz$ frequency. The experimental results are in good agreement the simulations and suggest that SRR lens can find actual application to focus the electromagnetic field of the microwave applicators for the thermal therapy of skin cancer.

ii) An extensive analysis of various design solutions has been performed in order to the fabrication of low-cost microwave needle applicators for interstitial hyperthermia cancer treatment. Two prototypes of 14 gauge and 16 gauge have been fabricated and characterized. The experimental results are in good agreements with simulations. Their employment can be considered as a desirable alternative to surgical resection, reducing side effects to healthy tissues and increasing patient wellness, as mini-invasive approach. In addition, various metamaterial lenses based on Closed Loop Resonator are designed and optimized to improve the performance of the 16G applicator. The numerical results are an interesting preliminary study and show great potential for subsequent developments.

iii) Metalenses have been designed and optimized in the frequency band of $f = 3 \div 15\ GHz$ in order to enhance the radiation performance of an antipodal Vivaldi antenna (AVA). Simulated and measured performances are in good agreement, confirming the improvement of the gain in a wide

frequency range, preserving the operating bandwidth. A maximum gain of about $G_{max} = 12\ dB$ and a maximum gain increase of about $\Delta G_{max} = 2.5\ dB$ have been measured, for the AVA with metalens based on SRR. Moreover, the novel L-shaped metalens improves both bandwidth and the gain, especially at high frequencies. A maximum gain increase of $\Delta G_{max} = 4.8\ dB$ and a maximum HPBW reduction of $\Delta HPBW_{max} = 31.3°$ have been measured at the frequency of $f = 13.8\ GHz$ with respect to the pristine AVA.

iv) A SIW applicator for the detection of water in diesel has been designed, starting from the dielectric characterization of water-diesel blends. A prototype of the applicator has been fabricated and characterized. An experimental sensitivity of $\Delta|S_{21}|/\ \Delta\rho = 1.42\ mdB/ppm$ has been obtained at a frequency of $f = 9.76\ GHz$ with a coefficient of determination $R^2 = 0.94$. The applicator is interesting because it is low-cost and low-profile, and it could be employed with a single frequency source and a microwave power meter.

The obtained results have been in part published in the Proceedings of National and International Conferences or on International Journals, as listed on page viii of the thesis.

References

[1] V. Portosi, A.M. Loconsole, F. Prudenzano, "A Split Ring Resonator-Based Metamaterial for Microwave Impedance Matching with Biological Tissue," *Applied Sciences*, 10, 9: 6740, 2020.

[2] V. Portosi, A.M. Loconsole, M. Valori, V. Marrocco, I. Fassi, F. Bonelli, G. Pascazio, V. Lampignano, A. Fasano, F. Prudenzano, "Low-Cost Mini-Invasive Microwave Needle Applicator for Cancer Thermal Ablation: Feasibility Investigation," *IEEE Sensors Journal*, 21, 13, 14027-14034, 2021.

[3] V. Portosi, A.M. Loconsole, M. Valori, V. Marrocco, F. Bonelli, G. Pascazio, V. Lampignano, A. Fasano, R. Lorusso, F. Prudenzano, "Optimization of low-cost needle microwave applicators for cancer therapy," *IEEE Proceedings XXXIV General Assembly and Scientific Symposium (GASS) of the International Union of Radio Science (URSI)*, Rome, Italy, 28 August – 4 September 2021.

[4] V. Portosi, A.M. Loconsole, M. Valori, V. Marrocco, F. Bonelli, G. Pascazio, V. Lampignano, A. Fasano, F. Prudenzano, "Refinement of a Microwave Needle Applicator for Cancer Therapy via Metamaterials," *IEEE Proceedings of 21st Mediterranean Microwave Symposium (MMS 2022)*, Italy, Pizzo (VV), 2022.

[5] V. Portosi, A. M. Loconsole, M. Valori, R. Lorusso, F. Bonelli, G. Pascazio, V. Lampignano, A. Fasano, R. Lorusso, F. Prudenzano, "Feasibility investigation of low-cost microwave needle applicator for thermal ablation cancer therapy", *IEEE Proceedings of 15th IEEE International Symposium on Medical Measurements and Applications 2020*, 1-3 June 2020, Bari, Italy, pp.1-6.

[6] V. Portosi, A.M. Loconsole, A. Campana, F. Anelli, F. Prudenzano, "A Novel L-Shaped Metalens for Ultra-Wide Band (UWB) Antenna Gain Improvement," *Applied Sciences*, 13, 8, 2023.

[7] A.M. Loconsole, V. Portosi, V.V. Francione, F. Anelli, A. Annunziato, M.C. Falconi, F. Prudenzano, "Optimization of a wideband antipodal Vivaldi antenna with metalenses," *International Journal of Microwave and Wireless Technologies,* 1-8, 2023.

[8] A.M. Loconsole, G. Roberto, M.C. Falconi, D. Laneve, V. Portosi, A. Massaro, N. Savino, F. Prudenzano, "Compact Vivaldi antipodal SIW antenna for GPR applications," *IEEE Proceedings XXXIV General Assembly and Scientific Symposium (GASS) of the International Union of Radio Science (URSI),* Rome, Italy, 28 August – 4 September 2021.

[9] A.M. Loconsole, V. Portosi, V.V. Francione, G. Roberto, F. Anelli and F. Prudenzano, "Wideband antipodal Vivaldi antenna with metalenses for GPR applications," *IEEE Proceedings of 21st Mediterranean Microwave Symposium (MMS 2022)*, Italy, Pizzo (VV), 2022. doi: 10.1109/MMS55062.2022.9825608

[10] A.M. Loconsole, V.V. Francione, V. Portosi, O. Losito, M. Catalano, A. Di Nisio, F. Attivissimo, F. Prudenzano, "Substrate-Integrated Waveguide Microwave Sensor for Water-in-Diesel Fuel Applications," *Applied Sciences*, 11, 21:10454, 2021.

[11] F. Anelli, A. Annunziato, A. Maria Loconsole, V. Portosi, S. Cozic, P. L. P. du Teilleul, S. Venck, S. Poulain, F. Prudenzano, "Low-Loss Fluoride Optical Fiber Coupler for Mid-Infrared Applications" submitted to *IEEE – Optica Journal of Lightwave Technology*, August 2023 (Under Review)

[12] A.M. Loconsole, M.C. Falconi, V. Portosi, F. Prudenzano, "Numerical Design of a Gain-Switched Pulsed Laser at 3.92 μm Wavelength Based on a Ho^{3+}-Doped Fluoroindate Fiber," *IEEE – Optica Journal of Lightwave Technology*, 39, 10, 3276-3283, 2021.

[13] A. Delazar, L. Nahar, S. Hamedeyazdan, S. Sarker, "Microwave-Assisted Extraction in natural products isolation," in *Methods in Molecular Biology*; Sarker, S., Nahar, L. Eds.; Humana Press: Clifton, NJ, USA, 2012; 864, 89-115.

[14] P.C. Veggi, J. Martinez, M.A.A. Meireles, "Fundamentals of Microwave Extraction," in *Microwave-assisted Extraction for Bioactive Compounds*, Food Engineering Series; Chemat, F., Cravotto, G. Eds.; Springer: Boston, MA, USA, 2012; 15-52.

[15] I. Safarik, K. Horska, K. Pospiskova, Z. Maderova, M. Safarikova, "Microwave assisted synthesis of magnetically responsive composite materials," *IEEE Trans. Magn.*, 49, 213-218, 2013.

[16] M.F.K., Ariffin, A. Idris, N.H.A. Ngadiman, "Optimization of one-pot microwave-assisted ferrofluid nanoparticles synthesis using response surface methodology," *IEEE Trans. Magn.*, Volume 54, page 1-6, 2018.

[17] M. Bozzetti, G. Calò, A. D'Orazio, V. Petruzzelli, F. Prudenzano, N. Diaferia, C. Bonaventura, "Mode-stirred chamber for cereal disinfestations," *Mater. Res. Innov.*, 8, 17-22, 2004.

[18] D.B. Oliveira, E.J. Silva, J.J.S. Santos, O.M. Neto, "Design of a microwave applicator for water sterilization using multiobjective optimization and phase control scheme," *IEEE Trans. Magn.*, 47, 1242-1245, 2011.

[19] M. Sethi, S.K. Chakarvarti, "Hyperthermia techniques for cancer treatment: a review," *Int. J. Pharmtech. Res.,* 8, 6, 2015.

[20] M.G. Skinner, M.N. Iizuka, Kolios, M.C. Kolios, M.D. Sherar, "A theoretical comparison of energy sources - microwave, ultrasound and laser - for interstitial thermal therapy," *Phys. Med. Biol.*, 43, 12, 3535-3547, 1999.

[21] M.C. Falconi, D. Laneve, M. Bozzetti, T.T. Fernandez, G. Galzerano, F. Prudenzano, "Design of an efficient pulsed Dy3+: ZBLAN fiber laser operating in gain switching regime," *J. Light. Technol*, 36, 23, 5327-5333, 2018.

[22] E. Ewertowska, R. Quesada, A. Radosevic, A. Andaluz, X. Moll, F. García Arnas, E. Berjano, F. Burdío, M. Trujillo, "A clinically oriented computer model for radiofrequency ablation of hepatic tissue with internally cooled wet electrode," *Int. J. Hyperthermia*, 35, 1, 194-204, 2018.

[23] J.C. Lin, P. Bernardi, S. Pisa, M. Cavagnaro, E. Piuzzi, "Antennas for medical therapy and diagnostics," in *Modern Antenna Handbook*, C.A. Balanis, John Wiley & Sons Inc. Publication, USA, 2008, pp. 1377–1401.

[24] C.J. Simon, D.E. Dupuy, W.W. Mayo-Smith, "Microwave ablation: principles and applications," *Radiographics*, 25, 2005.

[25] P. Bernardi, M. Cavagnaro, J.C. Lin, S. Pisa, E. Piuzzi, "Distribution of SAR and temperature elevation induced in a phantom by a microwave cardiac ablation catheter," *IEEE Trans. Microw. Theory Tech*., 52, 8, 1978–1986, 2004.

[26] H. Fallahi, P. Prakash, "Antenna designs for microwave tissue ablation," *Crit. Rev. Biomed. Eng*., 46, 6, 495-521, 2018.

[27] R. Ortega-Palacios, S. García-Jimeno, M.F.J. Cepeda, A. Vera, L. Leija, "Microwave ablation for breast cancer using a microcoaxial antenna: thermal comparison between swine breast tissue and breast phantom," in *Proceedings 2011 PAHCE*, Rio de Janeiro, Brazil, 2011.

[28] J. Vrba, L. Vojackova, O. Fiser, I. Merunka, "Microwave interstitial applicator array for treatment of pancreatic cancer," in *Proceedings PIERS-Toyama*, Toyama, Japan, 2018.

[29] L. Zhang, N. Wang, Q. Shen, W. Cheng, G.J. Qian, "Therapeutic efficacy of percutaneous radiofrequency ablation versus microwave ablation for hepatocellular carcinoma," *PLoS One*, 8, 10, 2013.

[30] P. Prakash, M.C. Converse, J.G. Webster, D.M. Mahvi, "An optimal sliding choke antenna for hepatic microwave ablation," *IEEE Trans. Biomed. Eng.,* 56, 10, 2470–2476, 2009.

[31] H. Luyen, S.C. Hagness, N. Behdad, "A balun-free helical antenna for minimally invasive microwave ablation," *IEEE Trans. Antennas Propag.*, 63, 3, 959–965, 2015.

[32] C.L. Brace, P.F. Laeseke, D.W. van der Weide, F.T. Lee, "Microwave ablation with a triaxial antenna: results in ex vivo bovine liver," *IEEE Trans. Microw. Theory Tech*., 53, 1, 215-220, 2005.

[33] S. Labonte, A. Blais, S.R. Legault, H.O. Ali, L. Roy, "Monopole antennas for microwave catheter ablation," *IEEE Trans. Microw. Theory Tech*., 44, 10, 1832–1840, 1996.

[34] W. Hurter, F. Reinbold, W.J. Lorenz, "A dipole antenna for interstitial microwave hyperthermia," *IEEE Trans. Microw. Theory Tech*., 39, 6, 1048–1054, 1991.

[35] Z.A. Ibitoye, E.O. Nwoye, M.A. Aweda, A.A. Oremosu, C.C. Annunobi, O.N. Akanmu, "Optimization of dual slot antenna using floating metallic sleeve for microwave ablation," *Med. Eng. Phys.,* 37, 4, 384–391, 2015.

[36] M. Cavagnaro, C. Amabile, P. Bernardi, S. Pisa, N. Tosoratti, "A minimally invasive antenna for microwave ablation therapies: design, performances and experimental assessment," *IEEE. Trans. Biomed. Eng.*, 58, 4, 949-959, 2011.

[37] I. Longo, G. Biffi Gentili, M. Cerretelli, N. Tosoratti, "A coaxial antenna with miniaturized choke for minimally invasive interstitial heating," *IEEE. Trans. Biomed. Eng.*, 50, 1, 82-88, 2003.

[38] H. Luyen, S.C. Hagness, N. Behdad, "Reduced-diameter designs of coax-fed microwave ablation antennas equipped with baluns," *IEEE Antennas Wirel. Propag. Lett.,* 16, 1385–1388, 2016.

[39] P. Gas, B. Szymanik, "Shape optimization of the multi-slot coaxial antenna for local hepatic heating during microwave ablation," in *Proceedings 2018 IIPhDW*, Swinoujście, Poland, 2018.

[40] R.C. Gupta, S.P. Singh, "Analysis of the SAR distributions in three-layered bio-media in direct contact with a water-loaded modified box-horn applicator," *IEEE Trans Microw. Theory Tech.*, 53, 2665-2671, 2005.

[41] O.M. Bucci, L. Crocco, R. Scapaticci, G. Bellizzi, "On the Design of Phased Arrays for Medical Applications," *IEEE Inst. Electr. Electron. Eng.*, 104, 633-648, 2016.

[42] S. Curto, P. McEvoy, X. Bao, M.J. Ammann, "Compact patch antenna for electromagnetic interaction with human tissue at 434 MHz," *IEEE Trans. Antennas Propag*., 57, 2564-2571, 2009.

[43] G. Muntoni, A. Fanti, G. Montisci, M. Muntoni, "A blood perfusion model of a RMS tumor in a local hyperthermia multi-physic scenario: a preliminary study," *IEEE J. Electromagn. RF Microw. Med. Biol.*, 3, 71-78, 2019.

[44] S. Singh, B. Sahu, S.P. Singh, "Conformal microstrip slot antenna with an AMC reflector for hyperthermia," *J. Electromagn. Waves Appl.*, 30, 1603-1619, 2016.

[45] J. Carlier, V. Thomy, J.C. Camart, L. Dubois, J. Pribetich, "Modeling of planar applicators for microwave thermotherapy," *IEEE Trans. Microw. Theory Tech.*, 50, 3036-3042, 2002.

[46] H. Attia, L. Yousefi, O.M. Ramahi, "Analytical model for calculating the radiation field of microstrip antennas with artificial magnetic superstrates: theory and experiment," *IEEE Trans. Antennas Propag.*, 59, 5, 1438-1445, 2001.

[47] Y.H. Liu, X.P. Zhao, "Investigation of anisotropic negative permeability medium cover for patch antenna," *IET Microw. Antennas Propag*., 2, 737-744, 2008.

[48] H. Attia, L. Yousefi, M.M. Bait-Suwailam, M.S. Boybay, O.M. "Ramahi, Enhanced-gain microstrip antenna using engineered magnetic superstrates," *IEEE Antennas Wirel. Propag. Lett.*, 8, 1198-1201, 2009.

[49] N.A. Jaffar, N. Buniyamin, K. Lias, "An overview of available metamaterial-based antenna for non-invasive hyperthermia cancer treatment," *Indones. J. Electr. Eng. Comput. Sci*., 14, 697-705, 2019.

[50] Y. Tao, G. Wang, "Conformal hyperthermia of superficial tumor with left-handed metamaterial lens applicator," *IEEE. Trans. Biomed. Eng*., 59, 3525-350, 2012.

[51] Y. Gong, G. Wang, "Superficial tumor hyperthermia with flat left-handed metamaterial lens," *Prog. Electromagn. Res. PIER*, 98, 389-405, 2009.

[52] D. Vrba, J. Vrba, "Novel applicators for local microwave hyperthermia based on zeroth-order mode resonator metamaterial," *Int. J. Antennas Propag.*, 2014, 1-7, 2014.

[53] D. Vrba, D.B. Rodrigues, J. Vrba, P.R. Stauffer, "Metamaterial antenna arrays for improved uniformity of microwave hyperthermia treatments," *Prog. Electromagn. Res. PIER*, 156, 1-12, 2016.

[54] X. Shi, Y. Cao, Y. Hu, X. Luo, H. Yang, L.H. Ye, "A High-Gain Antipodal Vivaldi Antenna With Director and Metamaterial at 1–28 GHz," *IEEE Antennas Wirel. Propag. Lett.*, *20*, 2432–2436, 2021.

[55] S. Zhu, H. Liu, P. Wen, "A New Method for Achieving Miniaturization and Gain Enhancement of Vivaldi Antenna Array Based on Anisotropic Metasurface,". *IEEE Trans. Antennas Propag.*, *67*, 1952–1956, 2019.

[56] R.C. Deng, X.-M. Yang, B. Ma, T.-Q. Li, H.-Y. Chen, Y. Yang, H. He, Y.-W. Chen, Z. Tang, "Performance enhancement of novel antipodal Vivaldi antenna with irregular spacing distance slots and modified-w-shaped metamaterial loading," *Appl. Phys. A*, *125*, 5, 2018.

[57] X. Li, H. Zhou, Z. Gao, H. Wang, G. Lv, "Metamaterial Slabs Covered UWB Antipodal Vivaldi Antenna," *IEEE Antennas Wirel. Propag. Lett.*, *16*, 2943–2946, 2017.

[58] L. Chen, Z. Lei, R. Yang, J. Fan, X. Shi, "A Broadband Artificial Material for Gain Enhancement of Antipodal Tapered Slot Antenna," *IEEE Trans. Antennas Propag.*, *63*, 395–400, 2015.

[59] L. Sang, S. Wu, G. Liu, J. Wang, W. Huang, "High-Gain UWB Vivaldi Antenna Loaded with Reconfigurable 3-D Phase Adjusting Unit Lens," *IEEE Antennas Wirel. Propag. Lett*., *19*, 322–326, 2020.

[60] M.A. Boujemaa, R. Herzi, F. Choubani, A. Gharsallah, "UWB Antipodal Vivaldi antenna with higher radiation performances using metamaterials," *Appl. Phys. A*, *124*, 714, 2018.

[61] M. Sun, Z.N. Chen, X. Qing, "Gain Enhancement of 60-GHz Antipodal Tapered Slot Antenna Using Zero-Index Metamaterial," *IEEE Trans. Antennas Propag.*, *61*, 1741–1746, 2013.

[62] S. El-Nady, H.M. Zamel, M. Hendy, A.H.A. Zekry, A.M. Attiya, "Gain Enhancement of a Millimeter Wave Antipodal Vivaldi Antenna by Epsilon-Near-Zero Metamaterial," *Prog. Electromagn. Res. C*, *85*, 105–116, 2018.

[63] S. Zhu, H. Liu, P. Wen, L. Du, J. Zhou, "A Miniaturized and High Gain Double-Slot Vivaldi Antenna Using Wideband Index-Near-Zero Metasurface," *IEEE Access*, *6*, 72015–72024, 2018.

[64] E. Erfani, M. Niroo-Jazi, S. Tatu, "A High-Gain Broadband Gradient Refractive Index Metasurface Lens Antenna," *IEEE Trans. Antennas Propag.*, *64*, 1968–1973, 2016.

[65] R. Singha, D. Vakula, "Gain enhancement of the ultra-wideband tapered slot antenna using broadband gradient refractive index metamaterial," *Int. J. RF Microw. Comput. Aided Eng.*, *28*, e21191, 2018.

[66] H. Cheng, Yang, Y. Li, Y. Chen, "A Compact Vivaldi Antenna with Artificial Material Lens and Sidelobe Suppressor for GPR Applications," *IEEE Access, 8*, 64056–64063, 2020.

[67] O. Yesilyurt, G. Turwn-Sayan, "Metasurface Lens for Ultra-Wideband Planar Antenna," *IEEE Trans. Antennas Propag.*, *68*, 719–726, 2020.

[68] P. Fei, Y.-C. Jiao, W. Hu, F.-S. Zhang, "A Miniaturized Antipodal Vivaldi Antenna With Improved Radiation Characteristics," *IEEE Antennas Wirel. Propag. Lett.*, *10*, 127–130, 2011.

[69] W. Wang, Y. Zheng, "Wideband Gain Enhancement of a Dual-Polarized MIMO Vehicular Antenna," *IEEE Trans. Veh. Technol., 70*, 7897–7907, 2021.

[70] A.Z. Hood, T. Karacolak, E. Topsakal, "A Small Antipodal Vivaldi Antenna for Ultrawide-Band Applications," *IEEE Antennas Wirel. Propag. Lett.*, *7*, 656–660, 2008.

[71] Y. Liu, W. Zhou, S. Yang, W. Li, P. Li, S. Yang, "A Novel Miniaturized Vivaldi Antenna Using Tapered Slot Edge With Resonant Cavity Structure for Ultrawideband Applications," *IEEE Antennas Wirel. Propag. Lett., 15*, 1881–1884, 2016.

[72] V. Gjokaj, J. Papapolymerou, J.D. Albrecht, B. Wright, P. Chahal, "A Compact Receive Module in 3-D Printed Vivaldi Antenna," *IEEE Trans. Compon. Packag. Manuf. Technol.*, *10*, 343–346, 2020.

[73] J. Puskely, J. Lacik, Z. Raida, H. Arthaber, "High-Gain Dielectric-Loaded Vivaldi Antenna for K_a-Band Applications," *IEEE Antennas Wirel. Propag. Lett., 15*, 2004–2007, 2016.

[74] M. Abbak, M.N. Akinci, M. Cayoren, I. Akduman, "Experimental Microwave Imaging With a Novel Corrugated Vivaldi Antenna," *IEEE Trans. Antennas Propag.*, *65*, 3302–3307, 2017.

[75] M.T. Islam, M.T. Islam, M. Samsuzzaman, H. Arshad, H. Rmili, "Metamaterial Loaded Nine High Gain Vivaldi Antennas Array for Microwave Breast Imaging Application," *IEEE Access*, *8*, 227678–227689, 2020.

[76] W. Digman, "Effects of Fuel Contamination on Corrosion of Aircraft Fuel Systems," SAE Technical Paper; Warrendale, PA, USA, 1962.

[77] I.M. Atadashi, M.K. Aroua, A.R. Abdul Aziz, N.M.N. Sulaiman, "The effects of water on biodiesel production and refining technologies: A review," *Renew. Sustain. Energy Rev*., 16, 3456–3470, 2012.

[78] L.C. Oliveira, E.G. Pereira, R.C. Oliveira, M.R.A. Morais, A.M.N. Lima, H. Neff, "SPR sensor for tampering detection in biofuels," in *IEEE Proceedings of the International Instrumentation and Measurement Technology Conference (I2MTC 2015)*, Pisa, Italy, 11–14 May 2015.

[79] B. Levitas, J. Matuzas, G. Viswanath, V. Basalingappa, V. Venkoparao, "UWB Based Oil Quality Detection," in *IEEE Proceedings of the International Conference on Ultra-Wideband (ICUWB 2011)*, Bologna, Italy, 14–16 September 2011.

[80] A. Kunte, S. Kulkarni, "Experimental investigation of complex permittivity and determination of ethanol content in gasoline," in *Proceedings of the International Conference of Recent Advances in Microwave Theory and Applications, Microwave 2008*, Jaipur, India, 21–24 November 2008; pp. 171–174.

[81] A. Kunte, A. Gaikwad, "Adulteration Detection in Petroleum Liquids using Stacked Multi Ring Resonator," in *Proceedings of the Third International Conference on Electrical, Electronics, Communication, Computer Technologies and Optimization Techniques (ICEECCOT 2018)*, Msyuru, India, 14–15 December 2018.

[82] A. Foundazi, K.M. Donnell, "Design of a Microstrip Patch Antenna for Microwave Sensing of Petroleum Production Lines," in *Proceedings of the United States National Committee of URSI National Radio Science Meeting (USNC-URSI NRSM 2017)*, Boulder, CO, USA, 4–7 January 2017

[83] C.H. Lee, Y. Jeong, H. Ashraf, "Rectangular Cavity Sensor for Distinguishing between Normal and High-Drivability-Index Gasolines," IEEE Access 2020, 8, 182193–182203.

[84] S. Kulkarni, M.S. Joshi, "Design and Analysis of Shielded Vertically Stacked Ring Resonator as Complex Permittivity Sensor for Petroleum Oils," *IEEE Trans. Microw. Theory Tech*., 63, 2411–2417, 2015.

[85] A.A. Kunte, A.N. Gaikwad, "Dielectric constant measurement of low loss liquids using stacked multi ring resonator," *Sadhana*, 43, 1–12, 2018.

[86] G.A. Eyebe, N. Sama, N. Boubekeur, F. Domigue, "Microwave Sensing Schemes of CPW Resonators Fully Printed on Humidity Sensitive Substrates," *IEEE Microw. Wirel. Compon. Lett.*, 29, 303–305, 2020.

[87] G. Andria, F. Attivissimo, A. Di Nisio, G.M. D'Aucelli, S.M. Camporeale, P. Pappalardi, "Design of a Microwave Sensor for Fuel Quality Monitoring," in *IEEE Proceedings of the 5th International Workshop on Metrology for AeroSpace (MetroAeroSpace 2018)*, Rome, Italy, 20–22 June 2018.

[88] G. Andria, F. Attivissimo, A. Di Nisio, A. Trotta, S.M. Camporeale, P. Pappalardi, "Design of a microwave sensor for measurement of water in fuel contamination," *Measurement*, 136, 74–81, 2019.

[89] M. Farries, N. Hayes, J. Kelley, G. Tippet, G. Webb, B. Tighe, K. Zhou, "Optical methods for detecting contamination in jet fuel," in *IEEE Proceedings of the Avionics, Fiber-Optics and Photonics Technology Conference*, San Antonio, TX, USA, 22–24 September 2009.

[90] W. Zhang, D.J. Webb, M. Carpenter, C. Williams, "Measuring water activity of aviation fuel using a polymer optical fiber Bragg grating," in *Proceedings of the SPIE, 23rd International Conference on Optical Fibre Sensors*, Santander, Spain, 2 June 2014.

[91] W. Zhang, S. Grice, K. Sugden, I. Bennion, "Free water in fuel sensor using fiber long period grating," in *Proceedings of the SPIE, 21st International Conference on Optical Fiber Sensors*, Ottawa, ON, Canada, 17 May 2011.

[92] W. Zhang, D.J. Webb, L. Lao, D. Hammond, M. Carpenter, C. Williams, "Water content detection in aviation fuel by using PMMA based optical fiber grating," *Sens. Actuators B Chem*., 282, 774–779, 2019.

[93] H. Räikkönen, M. Oksanen, "Microwave acoustic sensing of water in hydrocarbon/water solutions," *Sens. Actuator A Phys.*, 45, 99–101, 1994.

[94] V. Skwarek, T. Eggers, "A Low-cost Capacitive Fuel-level and Quality Sensor for Automotive Applications," in *Proceedings of the AMA Conferences 2013 - SENSOR 2013*, Nürnberg, Germany, 14–16 May 2013; pp. 680–685.

[95] Q. Xue, X. Tang, Y. Li, H. Liu, X. Duan, "Contactless and Simultaneous Measurement of Water and Acid contaminations in Oil Using a Flexible Microstrip Sensor," *ACS Sens.*, 5, 171–179, 2020.

[96] H. Liu, X. Tang, H. Lu, W. Xie, Y. Hu, Q. Xue, "An interdigitated impedance microsensor for detection of moisture content in engine oil," *Nanotechnol. Precis. Eng.*, 3, 75–80, 2020.

[97] K. Khalid, I.V. Grozescu, L.K. Tiong, L.T. Sim, R. Mohd, "Water detection in fuel tanks using the microwave reflection technique," *Meas. Sci. Technol*., 14, 1905–1911, 2003.

[98] Y. Cassivi, L. Perregrini, P. Arcioni, M. Bressan, K. Wu, G. Conciauro, "Dispersion characteristics of substrate integrated rectangular waveguide," *IEEE Microw. Wirel. Compon. Lett.*, 12, 333–335, 2002.

[99] F. Xu, K. Wu, "Guided-wave and leakage characteristics of substrate integrated waveguide," *IEEE Trans. Microw. Theory Tech*., 53, 66–73, 2005.

[100] G. Venanzoni, D. Mencarelli, A. Morini, M. Farina, F. Prudenzano, "Review of Substrate Integrated Waveguide Circuits for Beam-Forming Networks Working in X-Band," *Appl. Sci.*, 9, 1003, 2019.

[101] M. Bozzi, A. Georgiadis, K. Wu, "Review of substrate-integrated waveguide circuits and antennas," *IET Microw. Antenna Propag*., 5, 909–920, 2011.

[102] K. Wu, D. Deslandes, Y. Cassivi, "The Substrate Integrated Circuits-A New Concept for High-Frequency Electronics and Optoelectronics," in *Proceedings of the TELSKIS 2003*, Nis, Serbia and Montenegro, 1–3 October 2003.

[103] F. Bigelli, D. Mencarelli, M. Farina, G. Venanzoni, P. Scalmati, C. Renghini, A. Morini, "Design and Fabrication of a Dielectricless Substrate-Integrated Waveguide," *IEEE Trans. Compon. Packag. Manuf. Technol*., 6, 256–261, 2016.

[104] D. Mencarelli, A. Morini, F. Prudenzano, G. Venanzoni, B. Bigelli, O. Losito, M. Farina, "Broadband Single-Layer Slotted Array Antenna in SIW Technology," *IEEE Antennas Wirel. Propag. Lett.*, 15, 263–265, 2016.

[105] C. Liu, F. Tong, "An SIW Resonator Sensor for Liquid Permittivity Measurements at C Band," *IEEE Microw. Wirel. Compon. Lett*., 25, 751–753, 2015.

[106] O. Losito, V. Portosi, G. Venanzoni, F. Bigelli, D. Mencarelli, P. Scalmati, C. Renghini, P. Carta, F. Prudenzano, "Feasibility Investigation of SIW Cavity-Backed Patch Antenna Array for Ku Band Applications," *Appl. Sci.*, 9, 1271, 2019.

[107] C. Qi, D.R. Jackson, Y. Yao, J. Chen, "SIW Microstrip Cavity Resonators with a Sensing Aperture," in *IEEE Proceedings of the Texas Symposium on Wireless and Microwave Circuits and Systems (WMCS 2019)*, Waco, TX, USA, 28–29 March 2019.

[108] G. Venanzoni, D. Mencarelli, A. Morini, M. Farina, G. Angeloni, C. Renghini, P. Carta, P. Potenza, O. Losito, L. Mescia, et al. "Single

Layer Standalone Wideband Substrate Integrated Waveguide Directional Coupler," *Microw. Opt. Technol. Lett*., 56, 1141–1144, 2014.

[109] T. Castellano, O. Losito, L. Mescia, M.A. Chiapperino, G. Venanzoni, D. Mencarelli, G. Angeloni, C. Renghini, P. Carta, F. Prudenzano, "Feasibility Investigation of Low Cost Substrate Integrated Waveguide (SIW) Directional Couplers," *Prog. Electromagn. Res. B*, 59, 31–44, 2014.

[110] M.A. Chiapperino, O. Losito, T. Castellano, G. Venanzoni, L. Mescia, G. Angeloni, C. Renghini, P. Carta, P. Potenza, F. Prudenzano, "Dual-Band Substrate Integrated Waveguide Resonator Based on Sierpinski Carpet," *Prog. Electromagn. Res. C*, 57, 1–12, 2015.

[111] G. Venanzoni, D. Mencarelli, A. Morini, M. Farina, O. Losito, F. Prudenzano, "Compact Double-Layer Substrate Integrated Waveguide Magic Tee for X-Band Applications," *Microw. Opt. Technol. Lett.*, 58, 932–936, 2016.

[112] C. Caloz, T. Itoh., *Electromagnetic Metamaterials: Transmission Line Theory and Microwave Applications*; Wiley & IEEE Press: Hoboken, NJ, USA, 2006.

[113] J.B. Pendry, A.J. Holden, D.J. Robbins, W.J. Stewart, "Magnetism from conductors and enhanced Nonlinear phenomena," *IEEE Trans. Micro Theory* Tech., 47, 2075-2084, 1999.

[114] S. Maslovski, P. Ikonen, I. Kolmakov, S. Tretyakov, "Artificial magnetic material based on the new magnetic particle: Metasolenoid," *Prog. Electromagn. Res. PIER*, 54, 61–81. 2005.

[115] R.E. Collin, *Foundation for Microwave Engineering*, 2nd ed.; John Wiley & Sons, Inc.: Hoboken, NJ, USA, 2001.

[116] C.L. Holloway, E.F. Kuester, J.A. Gordon, J. O'Hara, J. Booth, D.R. Smith, "An Overview of the Theory and Applications of Metasurfaces: The Two-Dimensional Equivalents of Metamaterials," *IEEE Antennas Propag. Mag.*, 54, 10–35, 2012.

[117] D.R. Smith, D.C. Vier, T. Koschny, C.M. Soukoulis, "Electromagnetic parameter retrieval from inhomogeneous metamaterials," *Phys. Rev. E*, *71*, 036617, 2005.

[118] Z. Szabo, G.-H. Park, R. Hedge, E.-P. Li, "A Unique Extraction of Metamaterial Parameters Based on Kramers–Kronig Relationship," *IEEE Trans. Microw. Theory Tech.*, *58*, 2646–2653, 2010.

[119] G. Dolling, M. Wegener, C. M. Soukoulis, and S. Linden, "Negative index metamaterial at 780 nm wavelength," *Opt. Lett.*, 32, 53–55, 2007.

[120] W. Che, K. Deng, D. Wang, Y.L. Chow, "Analytical equivalence between substrate-integrated wave," *IET Microw Antennas Propag*., 2, 35-41, 2008.

[121] G. Venanzoni, D. Mencarelli, A. Morini, M. Farina, O. Losito, F. Prudenzano, "Compact substrate integrated waveguide six-port directional coupler for X-band applications," *Microw. Opt. Technol. Lett.*, 57, 2589-2592, 2015.

[122] C.A. Balanis, *Antenna theory analisys and design*, 4th ed.; John Wiley & Sons, Inc.: Hoboken, NJ, USA, 2016.

[123] Andreuccetti, R. Fossi, C. Petrucci, "An internet resource for the calculation of the dielectric properties of body tissues in the frequency range 10 Hz - 100 GHz," IFAC-CNR, Florence, Italy, 1997. Available online: http://niremf.ifac.cnr.it/tissprop.

[124] MC. Velázquez-Ahumada, MJ. Freire, R. Marqués, "Metamaterial focusing device for microwave hyperthermia," *Microw. Opt. Technol. Lett*., 53, 2868-2872, 2011.

[125] L. Leggio, O. de Varona, E. Dadrasnia, "A comparison between different schemes of microwave cancer hyperthermia treatment by means of left-handed metamaterial lenses," *Prog. Electromagn. Res. PIER*, 150, 73-87, 2015.

[126] K. Lias, N. Buniyamin, M. Zulkarnaen, "Simulation study of an EBG-M applicator towards non-invasive breast hyperthermia cancer procedure," *J. Teknol.*, 78, 75-81, 2016.

[127] Y. Tao, E. Yang, G. Wang, "Left-handed metamaterial lens applicator with build-in cooling feature for superficial tumor hyperthermia," *Appl. Comput. Electromagn. Soc. J.*, 32, 1029-1034, 2017.

[128] G. Andria, F. Attivissimo, A. Di Nisio, A. M. L. Lanzolla, P. Larizza, S. Selicato, "Development and performance evaluation of an electromagnetic tracking system for surgery navigation" *Measurement*, 148, 1-7, 2019.

[129] H.H. Pennes, "Analysis of tissue and arterial blood temperatures in the resting human forearm," *J. Appl. Physiol*., 1, 2, 5-34, 1948.

[130] A.P. O'Rourke, M. Lazebnik, J.M. Bertram, M.C. Converse, S.C. Hagness, J.G. Webster, D.M. Mahvi, "Dielectric properties of human normal, malignant and cirrhotic liver tissue: in vivo and ex vivo measurements from 0.5 to 20 GHz using a precision open-ended coaxial probe," *Phys. Med. Biol.*, 52, 15, 4707-4719, 2007.

[131] SPEAG, DAK Professional Handbook V 1.10, August 2013

[132] W. Scarcia, G. Palma, M.C. Falconi, F. De Leonardis, V.M.N. Passaro, F. Prudenzano, "Electromagnetic modelling of fiber sensors for low-cost and high sensitivity temperature monitoring," *Sensors*, 15,12, 29855-29870, 2015.

[133] M.C. Falconi, G. Palma, F. Starecki, V. Nazabal, J. Troles, J.L. Adam, S. Taccheo, M. Ferrari, F. Prudenzano, "Dysprosium-doped chalcogenide master oscillator power amplifier (MOPA) for mid-ir emission," *J. Light. Technol.*, 35, 2, 265–273, 2016.

[134] M.C. Falconi, G. Palma, F. Starecki, V. Nazabal, J. Troles, S. Taccheo, M. Ferrari, F. Prudenzano, "Design of an efficient pumping scheme for Mid-IR Dy3+:Ga5Ge20Sb10S65 PCF fiber laser," *IEEE Photon. Technol. Lett.*, 28, 18, 1984-1987, 2016.

[135] R.S. Quimby, L.B. Shaw, J.S. Sanghera, I.D. Aggarwal, "Modeling of cascade lasing in Dy: chalcogenide glass fiber laser with efficient output at 4.5 μm," *IEEE Photon. Technol. Lett*., 20, 2, 123–125, 2008

[136] C. Mustacchio, L. Boccia, E. Arnieri, G. Amendola, "A Gain Levelling Technique for On-Chip Antennas Based on Split-Ring Resonators," *IEEE Access*, *9*, 90750–90756, 2021.

[137] L. Chen, Q. Ma, S.S. Luo, F.J. Ye, H.Y. Cui, T.J. Cui, "Touch-Programmable Metasurface for Various Electromagnetic Manipulations and Encryptions," *Small*, *18*, 2203871, 2022.

[138] Q. Ma, W. Gao, Q. Xiao, L. Ding, T. Gao, Y. Zhou, X. Gao, T. Yan, C. Liu, Z. Gu, et al., "Directly wireless communication of human minds via non-invasive brain-computer-metasurface platform," *eLight*, *2*, 11, 2022.

[139] Y. Li, S. Chen, H. Liang, X. Ren, L. Luo, Y. Ling, S. Liu, Y. Su, S.T. Wu, "Ultracompact multifunctional metalens visor for augmented reality displays," *PhotoniX*, *3*, 29, 2022.

[140] A. Laxman Kumar, A. Ranjan, M. Chauhan, V.K. Killamsetty, B. Mukherjee, "Circular SRR Shaped UWB Antenna with WiMAX Band Notch Characteristics," in *Proceedings of the IEEE Radio and Antenna Days of the Indian Ocean (RADIO 2018)*, Wolmar, Mauritius, 15–18 October 2018; pp. 1–2.

[141] W.J. Krzysztofik, T.N. Cao, "Metamaterials in Application to Improve Antenna Parameters," in *Metamaterials and Metasurfaces*; IntechOpen: London, UK, 2019.

[142] M. Moniruzzaman, M.T. Islam, M. Samsuzzaman, M.M. Salaheldeen, N.M. Sahar, S.S. Al-Bawri, S.H.A. Almalki, H. Alsaif, M.S. Islam, "Gap coupled symmetric split ring resonator based near zero index

ENG metamaterial for gain improvement of monopole antenna," *Sci. Rep.*, *12*, 7406, 2022.

[143] R. Natarajan, J. V. George, M. Kanagasabai, A. Kumar Shrivastav, "A Compact Antipodal Vivaldi Antenna for UWB Applications," *IEEE Antennas Wirel. Propag. Lett.,* 14, 1557-1560, 2015.

[144] A. M. De Oliveira, M. B. Perotoni, S. T. Kofuji, J. F. Justo, "A Palm Tree Antipodal Vivaldi Antenna with Exponential Slot Edge for Improved Radiation Pattern," *IEEE Antennas Wirel. Propag. Lett*, 14, 1334-1337, 2015.

[145] Keysight. FieldFox Handheld Analyzers 4/6.5/9/14/18/26.5/32/44/50 GHz Datasheet. Available online: https://www. keysight.com/it/en/assets/7018-03314/data-sheets/5990-9783.pdf.

[146] D.M. Pozar, *Microwave Engineering*, 3rd ed.; Wiley: Hoboken, NJ, USA, 2004.

[147] A. Nella, A. Gandhi, "Lumped Equivalent Models of Narrowband Antennas and Isolation Enhancement in a Three Antennas System," *Radioengineering*, 27, 646–653, 2018.

[148] H. Dashti, M.H. Neshati, "Input Impedance of Rectangular Substrate Integrated Waveguide (SIW) Cavity Backed Slot Antennas," in *Proceedings of the 27th Iranian Conference on Electrical Engineering (ICEE)*, Tehran, Iran, 2–4 May 2017